Università degli Studi di Padova

Centro di Ateneo di Studi e Attività
Spaziali "Giuseppe Colombo" (CISAS)

Corso di Dottorato di Ricerca in:
Scienze Tecnologie e Misure Spaziali

Curricolo: Scienze e Tecnologie per Applicazioni Spaziali e Aeronautiche (STASA)

XXXI Ciclo

EXPERIMENTAL QUANTUM COMMUNICATION WITH GNSS SATELLITES

Coordinatore:
Ch.mo Prof. Giampiero Naletto
Supervisore:
Ch.mo Prof. Giuseppe Vallone

Dottorando:
Luca Calderaro

This thesis is dedicated to
my beloved family and Sara

A miracle, for what else could you call it:
today the sun rose at three-fourteen
and will set at eight-o-one.
A miracle, less surprising than it should be:
even though the hand has fewer than six fingers,
it still has more than four.
A miracle, just take a look around:
the world is everywhere.
An additional miracle, as everything is additional:
the unthinkable
is thinkable.

— Wislawa Szymborska

RINGRAZIAMENTI

Vorrei ringraziare il mio supervisore Prof. Giuseppe Vallone e il Prof. Paolo Villoresi per avermi accolto nel loro gruppo, dandomi l'opportunità di lavorare in questo ambito innovativo della ricerca. La loro continua curiosità e passione per la scienza, la grande esperienza e disponibilità sono state fonti di ispirazione durante questi anni.

La mia gratitudine va inoltre a tutti i miei colleghi "Luxorandi" per tutto l'aiuto che mi hanno dato e senza i quali questi tre anni non sarebbero stati così piacevoli. In particolare, vorrei ringraziare: Matteo Schiavon per avermi introdotto all'arte dell'allineamento del Sagnac; Francesco Vedovato, Costantino Agnesi e Daniele Dequal per le notti passate a MLRO a puntare satelliti fino all'alba; Mirko Pittaluga, Giulio Foletto e Francesco Picciariello per il loro contributo fondamentale in laboratorio; Alberto Santamato, Marco Avesani, Andrea Stanco, Alessia Scriminich, Marco Tomasin e Davide Marangon con i quali ho condiviso viaggi, conferenze e idee.

Un grande ringraziamento va a mia madre, mio padre e mia sorella per il loro instancabile sostegno, ai miei amici di una vita e a Sara.

Un sentito grazie a tutti.

Padova, Settembre 2018.

Luca Calderaro

PREFAZIONE

Il termine Comunicazione Quantistica si riferisce a tutti quei protocolli basati sulla trasmissione fedele di stati quantistici. L'enorme progresso tecnologico nella manipolazione delle singole particelle quantistiche ha portato alla realizzazione di test sperimentali su alcune delle più stravaganti predizioni della Meccanica Quantistica. I cosiddetti esperimenti mentali (gedankenexperiments) che sono stati formulati dai padri della Meccanica Quantistica nel secolo scorso, sono ora diventati realtà. Riportando le parole di Schrödinger: "... non sperimentiamo mai solo un elettrone o atomo o (piccola) molecola". Ciò non corrisponde più alla realtà dei fatti. Possiamo realizzare esperimenti che coinvolgono singoli atomi o molecole, e persino singoli fotoni; diventa quindi possibile dimostrare che le "conseguenze ridicole" a cui alludeva Schrödinger sono, in effetti, vere.

La possibilità di preparare, manipolare e rilevare singoli fotoni ha aperto la strada al campo della comunicatione quantistica. Molte applicazioni interessanti legate alla sicurezza delle comunicazioni iniziano a prendere forma, fra cui la più promettente è la distribuzione di chiave quantistica. Il passaggio cruciale verso l'utilizzo di queste tecnologie quantistiche è l'estensione del canale quantistico in modo tale da poter mettere in comunicazione, in linea di principio, due punti qualsiasi sulla superficie terrestre. A tal fine, vengono perseguite principalmente due strategie: lo sviluppo di ripetitori quantistici per connettere diversi tratti realizzati in fibra ottica, i quali hanno un'estensione limitata a causa delle perdite intrinseche della fibra, e lo sviluppo di canali quantistici intersatellitari e satellite-terra che sfruttano le minori perdite della trasmissione in aria/vuoto.

Questa tesi raccoglie i risultati del mio progetto di dottorato sotto la supervisione del Prof. Giuseppe Vallone e del Prof. Paolo Villoresi, relativi alla scienza della comunicazione quantistica. L'obiettivo principale del progetto è quello di estendere la comunicazione quantistica satellitare fino alle orbite MEO come base per la realizzazione di test fondamentali sulla Meccanica Quantistica. Particolare attenzione è stata dedicata anche alle applicazioni delle misure quantistiche deboli. Affinché questa tesi sia il più esaustiva possibile, il Capitolo 1 introduce brevemente il formalismo della teoria quantistica, che sarà usato in questo lavoro. I capitoli seguenti riportano i risultati del mio dottorato. In particolare, i Capitoli 2 e 3 sono relativi alla comunicazione quantistica spaziale e contengono materiale che è stato pubblicato come:

- Calderaro, Luca and Agnesi, Costatino and Dequal, Daniele and Vedovato, Francesco and Schiavon, Matteo and Santamato, Alberto and Luceri, Vincenza and Bianco, Giuseppe and Vallone, Giuseppe and Vil-

loresi, Paolo. "*Towards Quantum Communication from Global Navigation Satellite System*." In: Quantum Science and Technology (in press). Preprint available on arXiv: 1804.05022v1.

- Vedovato, Francesco and Agnesi, Costantino and Schiavon, Matteo and Dequal, Daniele and Calderaro, Luca and Tomasin, Marco and Marangon, Davide G. and Stanco, Andrea and Luceri, Vincenza and Bianco, Giuseppe and Vallone, Giuseppe and Villoresi, Paolo. "*Extending Wheeler's delayed-choice experiment to space.*" In: Science Advances 3.10, e1701180. ISSN: 2375-2548. DOI: 10.1126/sciadv.1701180.

- Agnesi, Costantino and Vedovato, Francesco and Schiavon, Matteo and Dequal, Daniele and Calderaro, Luca and Tomasin, Marco and Marangon, Davide G. and Stanco, Andrea and Luceri, Vincenza and Bianco, Giuseppe and Vallone, Giuseppe and Villoresi, Paolo. "*Exploring the boundaries of quantum mechanics: Advances in satellite quantum communications.*" In: Philosophical Transactions of the Royal Society of London Series A: Mathematical Physical and Engineering Science, vol. 376, 20170461. ISSN: 1364-503X. DOI: 10.1098/rsta.2017.0461

I Capitoli 4 e 5 trattano gli esperimenti sulle applicazioni delle misure quantistiche deboli, il cui materiale è stato pubblicato come:

- Schiavon, Matteo and Calderaro, Luca and Pittaluga, Mirko and Vallone, Giuseppe and Villoresi, Paolo. "*Three-observer Bell inequality violation on a two-qubit entangled state.*" In: Quantum Science and Technology 2.1, p. 015010. ISSN: 2058-9565. DOI: 10.1088/2058-9565/aa62be.

- Calderaro, Luca and Foletto, Giulio and Dequal, Daniele and Villoresi, Paolo and Vallone, Giuseppe. "*Direct reconstruction of the quantum density matrix by strong measurements.*" In: Physical Review Letters (in press). Preprint available on arXiv: 1803.10703v1.

PREFACE

Quantum Communication (QC) is referred as all those protocols that deal with the faithful transportation of quantum states. The huge technological progress in the manipulation of the single quantum particles has led to the experimental tests of some of the most intriguing features of Quantum Mechanics (QM). The gedankenexperiments that were formulated by the fathers of QM in the last century, have become real. In the words of Schrödinger: "... we never experiment with just one electron or atom or (small) molecule." This is no longer true. We can do experiments involving single atoms or molecules and even single photons, and thus it becomes possible to demonstrate that the "ridiculous consequences" alluded to by Schrödinger are, in fact, quite real.

The possibility of preparing, manipulating and detecting single photons has paved the way for the field of QC. Many interesting applications related to the security of communication start taking shape, of which the most promising is the Quantum Key Distribution (QKD). The crucial step towards the establishment of these quantum technologies is the extension of the communication channel up to the possibility of connecting any two points around the Earth. To this aim, two main strategies are being pursued: the development of quantum repeaters in order to interconnect several fiber-based channels, each of which have limited extension due to the inherent losses of the fiber, and the progress of satellite-to-ground and satellite-to-satellite links that take advantage of the lower losses of the free-space channel.

This thesis collects my research under the supervision of Prof. Giuseppe Vallone and Prof. Paolo Villoresi on a set of topics in the quantum communication science, the main objective being the extension of the satellite-to-ground channel towards MEO and its applications on the fundamental tests of QM. Particular attention have also been dedicated to the applications of weak measurements. In order for this thesis to be as self-contained as possible, Chapter 1 briefly introduces the formalism of the quantum theory, which will be used in this dissertation. The following chapters report the results of my work. In particular, Chapters 2 and 3 are related to the topic of Space Quantum Communication and contain material that have been published as:

- Calderaro, Luca and Agnesi, Costatino and Dequal, Daniele and Vedovato, Francesco and Schiavon, Matteo and Santamato, Alberto and Luceri, Vincenza and Bianco, Giuseppe and Vallone, Giuseppe and Villoresi, Paolo. "*Towards Quantum Communication from Global Navigation Satellite System*." In: Quantum Science and Technology (in press). Preprint available on arXiv: 1804.05022v1.

- Vedovato, Francesco and Agnesi, Costantino and Schiavon, Matteo and Dequal, Daniele and Calderaro, Luca and Tomasin, Marco and Marangon, Davide G. and Stanco, Andrea and Luceri, Vincenza and Bianco, Giuseppe and Vallone, Giuseppe and Villoresi, Paolo. "*Extending Wheeler's delayed-choice experiment to space.*" In: Science Advances 3.10, e1701180. ISSN: 2375-2548. DOI: 10.1126/sciadv.1701180.

- Agnesi, Costantino and Vedovato, Francesco and Schiavon, Matteo and Dequal, Daniele and Calderaro, Luca and Tomasin, Marco and Marangon, Davide G. and Stanco, Andrea and Luceri, Vincenza and Bianco, Giuseppe and Vallone, Giuseppe and Villoresi, Paolo. "*Exploring the boundaries of quantum mechanics: Advances in satellite quantum communications.*" In: Philosophical Transactions of the Royal Society of London Series A: Mathematical Physical and Engineering Science, vol. 376, 20170461. ISSN: 1364-503X. DOI: 10.1098/rsta.2017.0461

Chapters 4 and 5 address the experiments on the application of the weak measurements, whose material have been published as:

- Schiavon, Matteo and Calderaro, Luca and Pittaluga, Mirko and Vallone, Giuseppe and Villoresi, Paolo. "*Three-observer Bell inequality violation on a two-qubit entangled state.*" In: Quantum Science and Technology 2.1, p. 015010. ISSN: 2058-9565. DOI: 10.1088/2058-9565/aa62be.

- Calderaro, Luca and Foletto, Giulio and Dequal, Daniele and Villoresi, Paolo and Vallone, Giuseppe. "*Direct reconstruction of the quantum density matrix by strong measurements.*" In: Physical Review Letters (in press). Preprint available on arXiv: 1803.10703v1.

CONTENTS

LIST OF FIGURES

LIST OF TABLES

ACRONYMS

BS Beam Splitter

CCR Corner Cube Retroreflector

CEST Central European Summer Time

CHSH Clauser, Horne, Shimony, and Holt

EOM Electro-Optic Modulator

FFDP Far Field Diffraction Pattern

FPGA Field Programmable Gate Array

GLONASS GLObal NAvigation Satellite System

GNSS Global Navigation Satellite System

GPS Global Positioning System

HWP Half Wave Plate

ILRS International Laser Ranging Service

LCR Liquid Crystal Retarder

LEO Low Earth Orbit

MEO Medium Earth Orbit

MLRO Matera Laser Ranging Observatory

MPD Micro Photon Devices

NASA National Aeronautics and Space Administration

PBD Polarized Beam Displacer

PBS Polarized Beam Splitter

PMT Photon Multiplier Tube

PPKTP Periodically Poled Potassium Titanyl Phosphate

PPRA Pulse Peaker Regeneratice Amplifier

QC Quantum Communication

QI Quantum Information

QKD Quantum Key Distribution

QM Quantum Mechanics

QRNG Quantum Random Number Generator

QST Quantum State Tomography

QWP Quarter Wave Plate

RTT Round Trip Time

SHG Second Harmonic Generator

sHWP switchable Half Wave Plate

SLR Satellite Laser Ranging

SNR Signal to Noise Ratio

SPAD Single Photon Avalanche Photodiode

SPDC Spontaneous Parametric Down Conversion

TDC Time to Digital Converter

TIR Total Internal Reflection

Anybody who is not shocked by
quantum theory has not understood it.

— Niels Bohr

1

INTRODUCTION TO QUANTUM INFORMATION

Quantum Information (QI) is a branch of science born from the Quantum Mechanics theory and the Information theory. QI studies the quantification, processing, and communication of information encoded in quantum systems. Richard Feynman may be regarded as the father of QI. In a lecture titled *Simulating Physics with Computers* (Feynman, 1982) he put the question: can a classical, universal computer simulate any physical system? And in particular, what about quantum systems? Feynman noted that a computer based on quantum systems could have had a great advantage in terms of simulation efficiency with respect to the classical counterpart. The simulation of a many-particle quantum system may be in principle performed by a universal classical computer, but it becomes computationally intractable with just a 100 of particles in the system. The problem lies in the fact that the classical resources (number of bits) required grows exponentially with the number of particles. On the contrary, a quantum computer would need a number of quantum bits that depends linearly on the number of the particles to be simulated.

From the initial idea of exploiting quantum systems for simulation needs, many other applications have been found ranging from computation, to sensors and communication. The development of this field is leading to the so called *second quantum revolution*, in which the possibility of controlling single quantum particles allows for the realization of new groundbreaking technologies as secure communication networks, sensitive sensors for biomedical imaging and fundamentally new paradigms of computation.

In this Chapter, I will provide a brief overview of QI, introducing some results of the theory that will be used in this thesis.

1.1 POSTULATES OF QUANTUM MECHANICS

The predictions of Quantum mechanics can be derived from a series of postulates. The most widely used approach is the one formulated by Dirac and von Neumann, which I list below (Nielsen and Chuang, 2010; Renes, 2015):

- **States:**
  The set of states of an isolated physical system is in one-to-one correspondence to the projective space of a Hilbert space $\mathscr{H}$. In particular, any physical state can be represented by a normalized vector $|\phi\rangle \in \mathscr{H}$ which is unique up to a phase factor.

- **Dynamics:**
  For any possible evolution of an isolated physical system with state space $\mathscr{H}$ and for any fixed time interval $[t_0, t_1]$, there exists a unitary U describing the mapping of states $|\phi\rangle \in \mathscr{H}$ at time t_0 to the state $|\phi'\rangle = U|\phi\rangle$ at time t_1. The unitary U is unique up to a phase factor and is determined from the Hamiltonian, H, of the system by the Schrödinger equation

$$i\hbar \frac{\mathrm{d}}{\mathrm{d}t} |\phi\rangle = H|\phi\rangle , \tag{1.1}$$

  being $\hbar$ the reduced Planck constant.

- **Observables:**
  Any physical property of a system that can be measured is an observable and all observables are represented by self-adjoint linear operators acting on the state space $\mathscr{H}$. Each eigenvalue x of an observable O corresponds to a possible value of the observable. Since O is self-adjoint, it takes the form $O = \sum_x x\Pi_x$, where Π_x is the projector onto the subspace with eigenvalue x.

- **Measurements:**
  The measurement of an observable O yields an eigenvalue x. If the system is in a state $|\phi\rangle \in \mathscr{H}$, then the probability of observing outcome x is given by the *Born rule*:

$$P_X(x) = \mathrm{Tr}\left(\Pi_x |\phi\rangle \langle\phi|\right). \tag{1.2}$$

  The state $|\phi'_x\rangle$ of the system after the measurement, conditioned on the outcome x, is given by

$$|\phi'_x\rangle = \sqrt{\frac{1}{P_X(x)}}\Pi_x |\phi\rangle . \tag{1.3}$$

- **Composition:**
  For two physical systems with state spaces $\mathscr{H}_A$ and $\mathscr{H}_B$, the state space of the product system is isomorphic to $\mathscr{H}_A \otimes \mathscr{H}_B$. Furthermore, if the individual systems are in states $|\phi\rangle_A \in \mathscr{H}_A$ and $|\phi\rangle_B \in \mathscr{H}_B$, then the joint state is

$$|\Phi\rangle = |\phi\rangle_A \otimes |\phi\rangle_B . \tag{1.4}$$

1.2 QUBIT

The simplest quantum state represents physical systems which can be found into two alternative configurations and, in the analogy with the classical bit, is dubbed qubit. For instance, the state of a coin can be represented by the upper face being head or cross. It is customary to label the possible discrete configurations of a system by integer numbers, in our example 0 and 1. In the quantum framework, each state corresponds to a vector in a linear complex space, of dimension 2 for the qubit: $|0\rangle, |1\rangle \in \mathbb{C}^2$. Since the configurations $|0\rangle$ and $|1\rangle$ are mutually exclusive, they correspond to orthogonal states: $\langle 0|1\rangle = 0$. Hence, the states $|0\rangle$ and $|1\rangle$ are a orthonormal basis of the state space, also called computational basis. Contrary to the classical counterpart, a qubit $|\phi\rangle$ can be in any linear combination of the states $|0\rangle$ and $|1\rangle$, then in general

$$|\phi\rangle = \alpha |0\rangle + \beta |1\rangle , \tag{1.5}$$

being α and β any complex number such that $|\alpha|^2 + |\beta|^2 = 1$. Some examples of physical systems described by a qubit are listed in Tab. 1.1.

Physical system	Computational basis	
Spin-½	$\|m = 1/2\rangle$	$\|m = -1/2\rangle$
Photon polarization	$\|\text{Horizontal}\rangle$	$\|\text{Vertical}\rangle$
"Two-level" atom	$\|\text{groundstate}\rangle$	$\|\text{excitedstate}\rangle$

Table 1.1: Example of qubit systems.

A useful representation of the qubit space is the Bloch sphere. Any qubit $|\psi\rangle$ can be parametrized by a point of coordinates (θ, ϕ) in a sphere:

$$|\psi\rangle = \cos(\theta) |0\rangle + e^{i\phi} \sin(\theta) |1\rangle . \tag{1.6}$$

This identify a Bloch vector from the center to the surface of the sphere $\hat{n} = \hat{x} \sin\theta \cos\phi + \hat{y} \sin\theta \sin\phi + \hat{z} \cos\theta$. It is easy to see that $|\hat{n}\rangle$ and $|-\hat{n}\rangle$ are orthogonal state, hence the states along the six cardinal directions ($|\pm\hat{x}\rangle$, $|\pm\hat{y}\rangle$ and $|\pm\hat{z}\rangle$) form three orthogonal bases. These states are the eigenbases of the Pauli operators:

$$\begin{aligned}
\sigma_z &= |0\rangle \langle 0| - |1\rangle \langle 1| = \begin{pmatrix} 1 & 0 \\ 0 & -1 \end{pmatrix}, \\
\sigma_x &= |0\rangle \langle 1| + |1\rangle \langle 0| = \begin{pmatrix} 0 & 1 \\ 1 & 0 \end{pmatrix}, \\
\sigma_y &= -i |0\rangle \langle 1| + i |1\rangle \langle 0| = \begin{pmatrix} 0 & -i \\ i & 0 \end{pmatrix},
\end{aligned} \tag{1.7}$$

1.3 BIPARTITE STATES AND ENTANGLEMENT

As stated in the last postulate, we can consider multiple systems, for instance the polarization of two photons. It is in this setting that the weirdness of quantum mechanics shows up. Remarkably, the most general state of a two photons' polarization system, $|\psi\rangle_{AB} \in \mathscr{H}_A \otimes \mathscr{H}_B$, is not described by the single states of the two photons, say $|\phi\rangle_A \in \mathscr{H}_A$ and $|\phi'\rangle_B \in \mathscr{H}_B$. Indeed, in general we have

$$|\psi\rangle_{AB} \neq |\phi\rangle_A \otimes |\phi'\rangle_B . \tag{1.8}$$

This is in contrast with classical mechanics, in which, for instance, the position of a system composed by two particles is completely described by the position of the two single particles. The correct description for a composite system is found by following the postulates. Consider a orthonormal basis for each system $\mathscr{H}_A$ and $\mathscr{H}_A$ of dimension d_A and d_B, respectively: $\{|b_j\rangle_A \, | j = 1, \ldots, d_A\}$ and $\{|b_k\rangle_B \, | k = 1, \ldots, d_B\}$. Then a basis for the composite system is $\{|b_j\rangle_A \otimes |b_k\rangle_B\}$. Therefore, the global state is a linear combination of the basis:

$$|\psi\rangle_{AB} = \sum_{j=1}^{d_A} \sum_{k=1}^{d_B} \psi_{j,k} \, |b_j\rangle_A \otimes |b_k\rangle_B , \tag{1.9}$$

being $\psi_{j,k} \in \mathbb{C}$ such that $\sum_{j=1}^{d_A} \sum_{j=1}^{d_B} |\psi_{j,k}|^2 = 1$. I state now the *Schmidt decomposition* without proving it[1]. Given any bipartite state $|\psi\rangle_{AB} \in \mathscr{H}_A \otimes \mathscr{H}_B$, there exist orthonormal bases $\{|\xi_j\rangle_A\}$ and $\{|\eta_k\rangle_B\}$ for $\mathscr{H}_A$ and $\mathscr{H}_B$ respectively, such that

$$|\psi\rangle_{AB} = \sum_{j=1}^{d_{\min}} \lambda_j \, |\xi_j\rangle_A \otimes |\eta_j\rangle_B , \tag{1.10}$$

where $d_{\min} = \min(d_A, d_B)$, $\lambda_j \geq 0$ and $\sum_{j=1}^{2} \lambda^2 = 1$. Applied to the case of two photons' polarization state, we have that in general

$$|\psi\rangle_{AB} = \lambda_1 \, |\xi_1\rangle_A \otimes |\eta_1\rangle_B + \lambda_2 \, |\xi_2\rangle_A \otimes |\eta_2\rangle_B \tag{1.11}$$

that makes evident the correctness of the Eq. 1.8. A states that can be written as

$$|\psi'\rangle_{AB} = |\xi_1\rangle_A \otimes |\eta_1\rangle_B \tag{1.12}$$

belongs to the class of the so called *separable* states. All the other states that are not separable are called *entangled*. In particular, if $\lambda_j = 1/\sqrt{d_{\min}}$, the state is called *maximally entangled*.

1 for the interested reader the proof can be found in the books cited at the beginning of the Chapter, and in many others.

For the purposes of this thesis, I introduce the maximally entangled states for the polarization of two photons. The Bell states are the canonical maximally entangled state of two qubits:

$$\begin{aligned}
|\Phi\rangle_{AB} &= \frac{1}{\sqrt{2}}(|00\rangle_{AB} + |11\rangle_{AB}),\\
|\Phi_x\rangle_{AB} &= \frac{1}{\sqrt{2}}(|01\rangle_{AB} + |10\rangle_{AB}),\\
|\Phi_y\rangle_{AB} &= \frac{1}{\sqrt{2}}(|01\rangle_{AB} - |10\rangle_{AB}),\\
|\Phi_z\rangle_{AB} &= \frac{1}{\sqrt{2}}(|00\rangle_{AB} - |11\rangle_{AB}).
\end{aligned} \tag{1.13}$$

The ensemble of $|\Phi\rangle_{AB}$, $|\Phi_x\rangle_{AB}$, $|\Phi_y\rangle_{AB}$ and $|\Phi_z\rangle_{AB}$ forms a basis for the composite space $\mathscr{H}_A \otimes \mathscr{H}_B$ and is called the Bell basis. The state $|\Phi_y\rangle_{AB}$ is also referred to as the singlet state due to the nomenclature in atomic physics, corresponding to the state of two electrons with total spin equal to zero. In this thesis, I will often use the notation of horizontal $|H\rangle \equiv |0\rangle$ and vertical $|V\rangle \equiv |1\rangle$ polarization in place of the computational basis.

1.3.1 *No cloning*

A simple result that has major implications for quantum communication is the no-cloning theorem. It asserts that there is no physical process that can copy any quantum state into another. Suppose we have a cloning machine, whose action is represented by some unitary U, and that we have two photons A and B, with states $|\phi\rangle_A$ and $|0\rangle_B$, respectively. Hence, the global system is described by the state $|\phi\rangle_A |0\rangle_B$. The action of the cloning machine should be such that

$$U|\phi\rangle_A |0\rangle_B = |\phi\rangle_A |\phi\rangle_B = |\psi\rangle_{AB}, \tag{1.14}$$

where at the end of the process the B photon has the same state of the A photon. In particular, assume that the computational basis is copied from A to B:

$$U|0\rangle_A |0\rangle_B = |0\rangle_A |0\rangle_B \quad \text{and} \quad U|1\rangle_A |0\rangle_B = |1\rangle_A |1\rangle_B. \tag{1.15}$$

Then, for some state $|\phi\rangle_A = \alpha|0\rangle_A + \beta|1\rangle_A$, the linearity of the operator U implies

$$U|\phi\rangle_A |0\rangle_B = \alpha|0\rangle_A |0\rangle_B + \beta|1\rangle_A |1\rangle_B = |\psi'\rangle_{AB}. \tag{1.16}$$

The resulting state $|\psi'\rangle_{AB}$ is actually an entangled state, in contrast with the separable state $|\psi\rangle_{AB}$ that we wanted to obtain. For instance, if we take the

initial state such that $\alpha = \beta = 1/\sqrt{2}$ we end up with $|\psi'\rangle_{AB} = |\Phi\rangle_{AB}$. We conclude that

$$U |\phi\rangle_A |0\rangle_B \neq |\phi\rangle_A |\phi\rangle_B , \tag{1.17}$$

for arbitrary states ϕ.

The no-cloning theorem gives a hint about the possibility of devising communication protocols in which two parties can secretly communicate by exchanging quantum states. Assume that the two parties encode the message, to be exchanged, in a quantum state $|\phi\rangle_A$. The eavesdropper, that wants to know what the message is, cannot copy the quantum state, and if he blocks it or tries to measure it, the two parties will detect his presence and abort the communication before the information leakage.

1.4 DENSITY OPERATOR FORMALISM

The framework introduced in the previous section has been formulated using the language of state vectors. An alternative approach, that captures a wider set of scenarios usually encountered in quantum mechanics, is known as *density operator* or *density matrix*. It is mathematically equivalent to the state vector formulation, but it has the great feature of including classical information in the quantum description. In particular, it allows the possibility of dealing with systems whose states is not known, which is typically the case of systems interacting in an environment.

Assume that a quantum system is in one of a number of states $|\phi_i\rangle$ with probability p_i and $i = 1, \ldots, N$. Then, we can write the density operator of the system as

$$\rho = \sum_{i=1}^{N} p_i |\phi_i\rangle \langle\phi_i| , \tag{1.18}$$

with $\sum_{i=1}^{N} p_i = 1$. Mathematically, ρ is a linear operator (that can be represented as a matrix[2]) and represents our a priori[3] knowledge of the system state. In particular, if some $p_i = 1$ then the density operator is a *pure state*, in the sense that system's state is known with certainty, otherwise it is a *mixed state*. This resembles the classical idea of a random process. Assume that we want to describe the state of a coin after a toss. We would say that after the toss the face is either cross or head with 50% probability each. If we encode the two mutually exclusive states "head" and "cross" in the computational basis of a qubit, $|0\rangle$ and $|1\rangle$ respectively, we would equivalently say that the state of the qubit is either $|0\rangle$ or $|1\rangle$ with probabilities $p_0 = 0.5$ and $p_1 = 0.5$ respectively:

$$\rho = \frac{1}{2}(|0\rangle \langle 0| + |1\rangle \langle 1|). \tag{1.19}$$

2 from which the name density matrix.

3 Before a subsequent measurement on the system.

More generally, consider a classical random variable Z that takes discrete values z with probability $P(z)$. Also consider an orthonormal basis $\{|b_z\rangle\}$ on a Hilbert space of dimension equal to the number of possible values of Z. Then, the density operator

$$\rho_Z = \sum_Z P(z) \, |b_z\rangle \, \langle b_z| \, , \tag{1.20}$$

contains the information of the classical random Z. It is clear that a classical state can be embedded in the quantum mechanical framework by encoding it into orthonormal vector states.

From the definition given in Eq. 1.18, it is possible to prove that an operator ρ is a density operator associated to some ensemble $\{p_i, |\phi_i\rangle\}$ if and only if it satisfy the following conditions

- **Trace condition** ρ has trace equal to one: $\mathrm{Tr}(\rho) = 1$.
- **Positive condition** ρ is a positive semidefinite operator: $\langle\psi|\rho|\psi\rangle \geq 0$ for any $|\psi\rangle$.

Naively, any convex combination of density operators is again a density operator.

The postulates of quantum mechanics can be restated in the density operator framework.

- **States:**
  Any isolated physical system is associated to a Hilbert space $\mathscr{H}$. In particular, any physical state can be represented by a density operator, which is a positive operator with trace one, acting on the Hilbert space $\mathscr{H}$. If the quantum system is in a ensemble of states $\{p_i, \rho_i\}$, then the density operator is

  $$\rho = \sum_{i=1}^{N} p_i \rho_i \tag{1.21}$$

- **Dynamics:**
  For any possible evolution of an isolated physical system with state space $\mathscr{H}$ and for any fixed time interval $[t_0, t_1]$, there exists a unitary U describing the mapping of the density operator ρ at time t_0 to the state $\rho' = U\rho U^\dagger$ at time t_1. The unitary U is unique up to a phase factor and is determined from the Hamiltonian, H, of the system by the Schrödinger equation

  $$i\hbar \frac{\mathrm{d}}{\mathrm{dt}} \rho = [H, \rho], \tag{1.22}$$

  being $\hbar$ the reduced Planck constant.

- **Observables:**
  Any physical property of a system that can be measured is an observable and all observables are represented by self-adjoint linear operators acting on the state space $\mathscr{H}$. Each eigenvalue x of an observable O corresponds to a possible value of the observable. Since O is self-adjoint, it takes the form $O = \sum_x x\Pi_x$, where Π_x is the projector onto the subspace with eigenvalue x.

- **Measurements:**
  The measurement of an observable O yields an eigenvalue x. If the system is in a state ρ, then the probability of observing outcome x is given by the *Born rule*:

  $$P_X(x) = \mathrm{Tr}\left(\Pi_x \rho\right). \tag{1.23}$$

  The state ρ' of the system after the measurement, conditioned on the outcome x, is given by

  $$\rho' = \frac{\Pi_x \rho \Pi_x}{P_X(x)}. \tag{1.24}$$

- **Composition:**
  For two physical systems with state spaces $\mathscr{H}_A$ and $\mathscr{H}_B$, the state space of the product system is isomorphic to $\mathscr{H}_A \otimes \mathscr{H}_B$. Furthermore, if the individual systems are in states ρ_A and ρ_B, then the joint state is

  $$\rho = \rho_A \otimes \rho_B. \tag{1.25}$$

1.4.1 *Reduced density operator*

The formalism of the density operator has the great advantage of providing tools for describing subsystems. Assume to have a composite system in a Hilbert space $\mathscr{H}_A \otimes \mathscr{H}_B$, with state ρ_{AB}. The state solely describing the system $\mathscr{H}_A$ is given by the reduced density operator for the system A

$$\rho_A = \mathrm{Tr}_B(\rho_{AB}), \tag{1.26}$$

where Tr_B is the *partial trace* over the system B. As an example, consider the case of a separable state $\rho_{AB} = \rho \otimes \sigma$, with ρ the state of system A and σ the state of system B. From the definition of partial trace, we have

$$\rho_A = \mathrm{Tr}_B(\rho \otimes \sigma) = \rho. \tag{1.27}$$

A less trivial example is the Bell state $|\Phi\rangle$, whose density operator is

$$\rho_{AB} = |\Phi\rangle\langle\Phi| = \frac{|00\rangle\langle 00| + |11\rangle\langle 11| + |11\rangle\langle 00| + |00\rangle\langle 11|}{2}. \tag{1.28}$$

The subsystem ρ_A is then

$$\begin{aligned}\rho_A &= \mathrm{Tr}_B(\rho_{AB}) \\ &= \frac{|0\rangle\langle 0|\langle 0|0\rangle + |1\rangle\langle 1|\langle 1|1\rangle + |1\rangle\langle 0|\langle 0|1\rangle + |0\rangle\langle 1|\langle 1|0\rangle}{2} \\ &= \frac{1}{2}(|0\rangle\langle 0| + |1\rangle\langle 1|),\end{aligned} \tag{1.29}$$

which is the completely mixed state. Hence, if the global system is in a completely known pure state, the subsystem may be in a random mixed state. This strange property is another hallmark of quantum entanglement.

1.4.2 *Purification of mixed states*

In the previous section we have seen that a composite system in a pure state may describe its subsystems in a mixed state. Remarkably, we can do the reverse action, stating that any density matrix is a reduced density operator of a pure state in a larger Hilbert space. This mapping is called purification: given a density operator ρ_A on Hilbert space $\mathscr{H}_A$, a purification $|\Psi\rangle_{AB}$ is a pure state on Hilbert space $\mathscr{H}_A \otimes \mathscr{H}_B$ for some $\mathscr{H}_B$, such that

$$\rho_A = \mathrm{Tr}_B(|\Psi\rangle_{AB}\langle\Psi|_{AB}). \tag{1.30}$$

To prove that we can find a purification for any state ρ_A, assume that such density operator is associated to the ensemble $\{p_i, |i\rangle_A\}$, with $|i\rangle_A$ being an orthonormal basis on $\mathscr{H}_A$ (this is always possible due to the Schmidt decomposition):

$$\rho_A = \sum_i p_i |i\rangle\langle i|_A . \tag{1.31}$$

We introduce a space system $\mathscr{H}_B$ with same dimension as $\mathscr{H}_A$, and choose an orthonormal basis $\{|\phi_i\rangle_B\}$ and define the purification as

$$|\Psi\rangle_{AB} = \sum_i \sqrt{p_i}\,|i\rangle_A \otimes |\phi_i\rangle_B . \tag{1.32}$$

The reduced density operator is

$$\begin{aligned}\mathrm{Tr}_B(|\Psi\rangle_{AB}\langle\Psi|_{AB}) &= \sum_{ij}\sqrt{p_i p_j}\,|i\rangle\langle j|_A\langle\phi_j|\phi_i\rangle_B \\ &= \sum_{ij}\sqrt{p_i p_j}\,|i\rangle\langle j|_A\,\delta_{ij} \\ &= \sum_i p_i |i\rangle\langle i|_A \\ &= \rho_A\end{aligned} \tag{1.33}$$

1.5 QUANTUM CIRCUITS

A useful way to represent the dynamics of a quantum system is through a circuital scheme. This is the standard representation used in quantum computation, in which the evolution follows an algorithm and hence the quantum state changes step by step. In this scenario, the time is discrete and the whole evolution is divided in several blocks, called *gates*, each one representing a unitary acting on a subsystem. Contrary to the typical approach in which the unitary is calculated from the specific physical system, the mathematical description of the algorithm is independent from its actual physical implementation. Therefore, the gates are chosen from a finite set of simple unitaries acting on single or couples of qubits.

In this section, I will introduce the basic building blocks of the circuit model, describing some of the most commonly used gates.

1.5.1 *Quantum Wires*

A wire represents a Hilbert space and connects a series of gates, i.e. unitaries, acting on that space (Fig. 1.1). For each wire we can assign a density operator through the reduction of the global state. As an alternative pictorial interpretation, we may think of the wire as a carrier of quantum states from a point to another, typically from left to right. It is standard to denote a single qubit with a quantum wire.

Figure 1.1: Qubit quantum wire.

1.5.2 *Quantum Gates*

Quantum gates are unitaries, schematically represented by boxes. We may assign a particular gate for each unitary. However, it has been shown (Lloyd, 1994) that there exists a finite set of quantum gates with which any unitary can be arbitrarily approximated. This was a remarkable result toward the realization of the quantum computer, since it allows experimentalists to focus on a small number of gates to be made concrete. Therefore, we introduce a set of gates acting on a single and on two qubits.

1.5.2.1 *Single-qubit gates*

Single-qubit gates are represented by 2×2 unitary matrices in the computational basis. The circuit representation of single-qubit gates is shown in Fig. 1.2, with a letter identifying the type of gate.

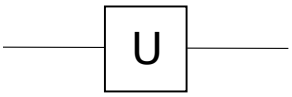

Figure 1.2: Single-qubit gate implementing the unitary U.

An useful gate is the *Hadamard gate*, described by the matrix

$$H = \frac{1}{\sqrt{2}} \begin{pmatrix} 1 & 1 \\ 1 & -1 \end{pmatrix}. \tag{1.34}$$

This gate transforms the computational basis $\{|0\rangle, |1\rangle\}$ into the diagonal one $\{|+\rangle, |-\rangle\}$ and vice-versa.

The *rotation gate* rotates the vector on the Bloch sphere about one cardinal axis of an angle θ

$$\begin{aligned} R_x(\theta) &= \begin{pmatrix} \cos\frac{\theta}{2} & -i\sin\frac{\theta}{2} \\ -i\sin\frac{\theta}{2} & \cos\frac{\theta}{2} \end{pmatrix} \\ R_y(\theta) &= \begin{pmatrix} \cos\frac{\theta}{2} & -\sin\frac{\theta}{2} \\ \sin\frac{\theta}{2} & \cos\frac{\theta}{2} \end{pmatrix} \\ R_z(\theta) &= \begin{pmatrix} e^{-i\frac{\theta}{2}} & 0 \\ 0 & e^{i\frac{\theta}{2}} \end{pmatrix} \end{aligned} \tag{1.35}$$

From the rotation about the z axis we can construct the *phase gate*

$$S = \begin{pmatrix} 1 & 0 \\ 0 & i \end{pmatrix}. \tag{1.36}$$

1.5.2.2 *Two-qubit gates*

The most important class of two-qubit gates is the one of controlled operations, that are represented as in Fig. 1.3

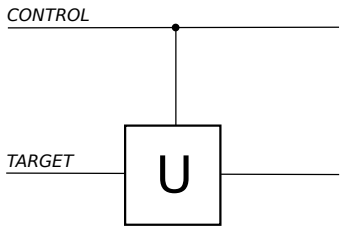

Figure 1.3: Controlled-U operation. The unitary is applied to the target only if the control qubit is in $|1\rangle$.

They have two wires as input and output called *control* and *target*. The former decides which unitaries to apply on the latter, being the identity if the

control state is $|0\rangle$ or U otherwise. An important controlled gate is the *CNOT gate* (controlled not), with matrix

$$CNOT = \begin{pmatrix} 1 & 0 & 0 & 0 \\ 0 & 1 & 0 & 0 \\ 0 & 0 & 0 & 1 \\ 0 & 0 & 1 & 0 \end{pmatrix}, \tag{1.37}$$

that flips the state of the target qubit whenever the control state is in $|1\rangle$. The set formed by single-qubit gates and the CNOT gate is universal for quantum computation.

Another controlled gate that will be later used in this thesis is the *controlled phase shift gate*. In this gate the unitary applyed on the target is the rotation around the z axis of the Bloch sphere, which is described by the matrix

$$CP(\epsilon) = \begin{pmatrix} 1 & 0 & 0 & 0 \\ 0 & 1 & 0 & 0 \\ 0 & 0 & e^{i\epsilon} & 0 \\ 0 & 0 & 0 & e^{-i\epsilon} \end{pmatrix}. \tag{1.38}$$

1.5.3 *Measurements*

Measurements are typically the final element of a quantum circuit. It is conventional not to use any special symbols to denote more general measurements than the projection on to the computational basis, since they can always be represented by unitary transforms with ancilla qubits followed by projective measurements. The standard symbol is shown in Fig. 1.4. Being destructive measurements, the output is not a quantum state but rather a classical bit sometimes represented in the circuit as a double line. In general, quantum measurements are performed as an intermediate step in a quantum circuit and the classical outputs are used to conditionally control subsequent quantum gates. However, they can always be moved to the end of the circuit replacing the classical controlled operations by conditional quantum operations.

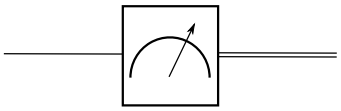

Figure 1.4: Projective measurement on the computational basis. The input is a quantum wire whereas the output is a classical bit denoted as a double wire.

1.6 QUANTUM STATE TOMOGRAPHY

Quantum State Tomography (QST) is the standard tool used for the reconstruction of the density matrix of a quantum state. Consider a quantum system in a d-dimensional Hilbert space, described by the state ρ. Then, the reconstruction of the matrix ρ requires the determination of $d^2 - 1$ independent real parameters. Indeed, a $d \times d$ matrix in the complex vector space can be represented by a linear combination of a orthogonal basis $\{\hat{\sigma}_k | k = 1, \ldots, d^2\}$ that satisfies the relation $\mathrm{Tr}(\hat{\sigma}_k, \hat{\sigma}_j) = \alpha \delta_{k,j}$, with α a constant. For example, the 2×2 matrices can be written as a linear combination of Pauli matrices plus the identity $\{\mathbb{I}, \sigma_x, \sigma_y, \sigma_z\}$. However, in general we have

$$\rho = \sum_{k=1}^{d^2} \frac{1}{\alpha} \hat{\sigma}_k \mathrm{Tr}(\hat{\sigma}_k \rho). \tag{1.39}$$

In an experiment, we can device some set of observables $\{\Pi_j | j = 1, \ldots, d^2\}$ to apply on the quantum system. Then, the postulates of QM state that, if we repeat N times the measurement of Π_j on the state, the mean value will be n_j with

$$n_j = N \mathrm{Tr}(\Pi_j \rho). \tag{1.40}$$

Substituting Eq. 1.39 into Eq. 1.40, we obtain

$$n_j = \frac{N}{\alpha} \sum_{k=1}^{d^2} \mathrm{Tr}(\hat{\sigma}_k \rho) \mathrm{Tr}(\Pi_j \hat{\sigma}_k). \tag{1.41}$$

By defining the $d^2 \times d^2$ matrix B such that $B_{j,k} = \mathrm{Tr}(\Pi_j \hat{\sigma}_k)$ and by inverting it, one gets

$$\mathrm{Tr}(\hat{\sigma}_k \rho) = \frac{\alpha}{N} \sum_{j=1}^{d^2} (B^{-1})_{k,j} n_j, \tag{1.42}$$

which is the k-th parameter of the linear combination, associated to the element of the basis $\hat{\sigma}_k$. In order for the matrix B to be invertible, the experimenter has to choose a set of Π_j linearly independent. Such a set is called a *tomographically complete* set of projectors. In the event that the parameter N is not known from the experiment, the normalization of the matrix ρ gives its value.

As an example, consider the reconstruction of the density matrix of a qubit. A tomographically complete set of measurements is the following

$$\Pi_0 = \frac{1}{2}(|0\rangle\langle 0| + |1\rangle\langle 1|), \quad \Pi_1 = |+\rangle\langle +|, \quad \Pi_2 = |i\rangle\langle i|, \quad \Pi_3 = |0\rangle\langle 0|, \tag{1.43}$$

being $|+\rangle = \frac{1}{\sqrt{2}}(|0\rangle + |1\rangle)$ and $|i\rangle = \frac{1}{\sqrt{2}}(|0\rangle + i\,|1\rangle)$. As a basis for the 2×2 matrices we choose the pauli matrices plus the identity, with $\alpha = 2$. Therefore, we have

$$B = \begin{pmatrix} 1 & 0 & 0 & 0 \\ 1 & 1 & 0 & 0 \\ 1 & 0 & 1 & 0 \\ 1 & 0 & 0 & 1 \end{pmatrix}, \quad \text{and} \quad B^{-1} = \begin{pmatrix} 1 & 0 & 0 & 0 \\ -1 & 1 & 0 & 0 \\ -1 & 0 & 1 & 0 \\ -1 & 0 & 0 & 1 \end{pmatrix}. \tag{1.44}$$

Note that the measurement of Π_0 provides the value of N ($n_0 = N$), whereas the other parameters are

$$\mathrm{Tr}(\hat{\sigma}_k \rho) = \frac{n_k - n_0}{n_0}. \tag{1.45}$$

In general, the reconstructed matrix via Eqs. 1.39 and 1.40 does not satisfy the normalization and non-negativity conditions, since experimental errors may introduce fluctuations and/or biases to the results. In that case, the procedure ends with an unphysical state. A post-processing of the data is usually adopted to find the physical matrix ρ^{opt} that best reproduces the experimental data n_j. The approach consists of defining $\rho(t) = T^\dagger(t)T(t)$ to satisfy non-negativity, with $T(t)$ a triangular matrix containing all d^2 real parameters:

$$T(t) = \begin{pmatrix} t_1 & 0 \\ t_3 + it_4 & t_2 \end{pmatrix}, \tag{1.46}$$

in the qubit case. Indeed, for any $|\psi\rangle$:

$$\langle\psi|\, T^\dagger T\, |\psi\rangle = \langle\psi'|\psi'\rangle \geq 0. \tag{1.47}$$

Then the optimization problem reduces to finding the minimum of the "likelihood" function, for some t^{opt}

$$L(t) = \sum_{j=1}^{d^2} \frac{(N\mathrm{Tr}(\Pi_j \rho(t)) - n_j)^2}{2N\mathrm{Tr}(\Pi_j \rho(t))}. \tag{1.48}$$

The result is a physical state $\rho^{\mathrm{opt}} = \rho(t^{\mathrm{opt}})$.

1.7 WEAK MEASUREMENTS

The measurement postulate involves two remarkable elements. First, it gives the probability for a certain outcome to be revealed. Second, after the measurement, the state of the system is changed to the eigenvector associated to the outcome result. The latter is a highly debated property of the quantum measurement. The typical interpretation states that an observer trying

to get some information about the quantum system will always perturb its state. In particular, it is not a matter of how the experiment is designed, but it is inherent to the interaction between the system and the measurement device. As introduced by Neumann, 1932, the process of measurement can be modeled by an interaction between the system to be measured (the *object*) and an *ancilla* (also called *pointer*), that represents the quantum state of the measuring device. After the interaction, the ancilla is projected onto a state. Clearly, due to the interaction the state of the measuring device will change, becoming entangled with the object. This implies that a projection of the ancilla state will change also the system, in agreement with the postulate. However, as proposed by Aharonov, Albert, and Vaidman, 1988 the interaction can be "weakened" so that the object and ancilla states slightly change from the initial condition. This *weak measurement* had unexpected results, that reveals to be very useful in several measurement applications. In particular, in Chapter 5 I will discuss the application on the reconstruction of the quantum states. In this section, I will describe the basic idea of the weak measurement adapted to the work of this thesis, introducing the concept of the *weak value*.

For the purpose of this thesis, I consider the system and ancilla's Hilbert space to be 2-dimensional each, but the same results hold for arbitrary dimension. Suppose that the initial joint state of the object and ancilla systems is in the pure state, for simplicity,

$$|\psi\rangle = |\phi_S\rangle \otimes |0_A\rangle \,. \tag{1.49}$$

The state is separable since the two systems had no prior interaction. Note that the choice of the initial state of the ancilla is not restricted to a state of the computational basis. We may choose another arbitrary qubit since the observer has complete control on its preparation. To measure an observable S on the object system, the interaction can be modeled by the Hamiltonian

$$H_{\text{int}}(t) = \theta S \otimes \sigma_y, \tag{1.50}$$

being θ a real coefficient determining the strength of interaction. Hence, the evolution is given by the unitary

$$U = e^{-i\theta S \otimes \sigma_y}. \tag{1.51}$$

This operator implements a rotation of the ancilla vector around the y axis of the Bloch sphere by an angle that is the result of the measurement of S in the object system, multiplied by two times θ. Basically, we can interpret the ancilla as the needle of the meter that rotates according to the observable we want to measure on the system. Assuming that the eigenvalues of S are $\{0, 1\}$ and $\theta = \pi/2$, after the interaction the ancilla would be either rotated of π or not, which are two orthogonal vectors in the Bloch sphere. Hence, one can devise a measurement on the ancilla that distinguishes in which of the two

states the ancilla is. This last step perturbs the ancilla's state as well as the one of the system, because the interaction made them entangled. Therefore this model is theoretically equivalent to a measurement of S on the system state, as described by the postulates. Nonetheless, it introduces a scenario that resembles a real experiment in which the system is usually probed by a meter.

Now, assume to choose $\theta \to 0$. The interaction becomes weak and it can be truncated to the first order in θ

$$U \simeq \mathbb{I} - i\theta S \otimes \sigma_y. \tag{1.52}$$

The ancilla state will not end into two distinguishable states, hence its measurement cannot discern between the two possible outcomes of S. However, suppose to add a *post-selection* of the system state by projecting it into a state $|\Phi_S\rangle$. The ancilla state will be

$$|\eta_A^{'}\rangle \simeq |\eta_A\rangle - i\theta \langle S^W\rangle_\phi^\Phi \sigma_y |\eta_A\rangle , \tag{1.53}$$

with $\langle S\rangle^W$ the *weak value* of the observable S defined as:

$$\langle S^W\rangle_\phi^\Phi = \frac{\langle \Phi_S|S|\phi_S\rangle}{\langle \Phi_S|\phi_S\rangle}. \tag{1.54}$$

Remarkably, it is possible show that the weak value is related to the measurements of σ_x and σ_y on the ancilla state:

$$\begin{aligned} \mathrm{Re}(\langle S^W\rangle_\phi^\Phi) &\simeq \frac{1}{2\theta} \langle \sigma_x\rangle_{\eta_A'} \\ \mathrm{Im}(\langle S^W\rangle_\phi^\Phi) &\simeq \frac{1}{2\theta} \langle \sigma_y\rangle_{\eta_A'} . \end{aligned} \tag{1.55}$$

2

SINGLE PHOTONS FROM GLOBAL NAVIGATION SATELLITE SYSTEMS

Ideally, the realization of a QC protocol requires the exchange of single quanta of energy (e.g. photons). In practice, the use of truly single-photon sources in high lossy channels, such as the satellite–to–ground link, is beyond of the current state of the art (Idani et al., 2013). In practical implementations, weak coherent sources (e.g. lasers attenuated at the single photon regime) can be used instead. For instance, QKD can be securely realized using attenuated lasers, provided that the so called decoy protocol is used (Hwang, 2003; Wang, 2005). Nonetheless, when it is necessary to use the source in space-like environments, the standard laboratory design is not sufficient for its reliable use in orbit. The process of spatialization is costly and time consuming, due to the several hardness tests that the model has to pass. Of course this is compulsory for the realization of a complete communication system (Cao et al., 2018; Fink et al., 2017; Villar, Lohrmann, and Ling, 2017), but for the study of the satellite–to–ground quantum channel this may be overkilling.

An effective way to circumvent the use of active sources is through the use of passive CCR on board of artificial satellites. From the ground station, an intense pulsed coherent light is directed to the orbiting CCR array. Due to the small effective area of the CCR array and the divergence of the up-going beam, the reflected light, returning to the ground station, is highly attenuated. This technique does not allow a direct measurement of the number of photons reflected by the CCR array, which should be inferred from the knowledge of the channel losses and the received and/or transmitted photons at the ground. The modeling of the channel losses is complicated since it depends on weather conditions, which may vary in time, and on the information about the CCR array design, which may be non-exhaustive for all satellites. However, there are several satellites, launched for scientific purposes, that have been thoroughly characterized for the use in Satellite Laser Ranging (SLR).

In this Chapter, I will introduce to the properties of CCR and to the modeling of the satellite–to–ground channel losses. Finally, I will report on our work about the realization of single photon exchange from two GLObal NAvigation Satellite System (GLONASS) satellites, orbiting at an altitude of 19,100 km, and the Matera Laser Ranging Observatory (MLRO).

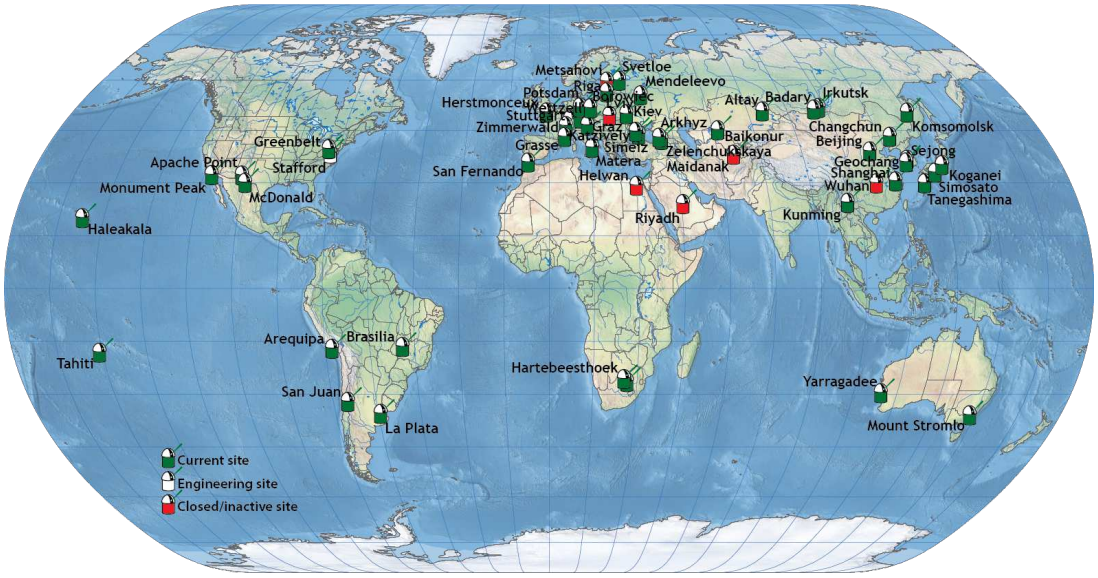

Figure 2.1: Map of the SLR stations updated to November 2017. The map clearly shows the non-uniform coverage of SLR stations, that are mostly situated in the North hemisphere, especially in Europe and Asia. From the ILRS website (*ILRS Home Page*).

2.1 CORNER CUBE RETROREFLECTORS ON ARTIFICIAL SATELLITES

In 1964, NASA initiated the SLR to near-Earth satellites. SLR is a distance measurement technique that employs short laser pulses directed towards a satellite and reflected back to the observatory by CCR mounted on the satellite itself. This technique provides very high precision, up to the level of few millimeters for a single measurement (Bianco et al., 2001b). The scientific products derived using SLR include: precise geocentric positions and motions of ground stations, satellite orbits, components of Earth's gravity field and their temporal variations, Earth orientation parameters (which is important for the elaboration of the International Terrestrial Reference Frame).

Nowadays, there exist more than 40 active SLR stations, coordinated by the International Laser Ranging Service (ILRS), that is in charge of collecting, managing and distributing the data of each SLR station. The stations are distributed all over the Earth, with higher concentration in Europe and in the far East, as shown in Fig. 2.1. The satellites used in laser ranging are placed both in Low Earth Orbit (LEO) and in middle Earth orbit Medium Earth Orbit (MEO), with various orbit inclinations and eccentricities. The orbit of the satellites are predicted on a daily basis from the data collected by the different SLR stations. Predictions are then redistributed to SLR station, where they are used as input to the satellite tracking system.

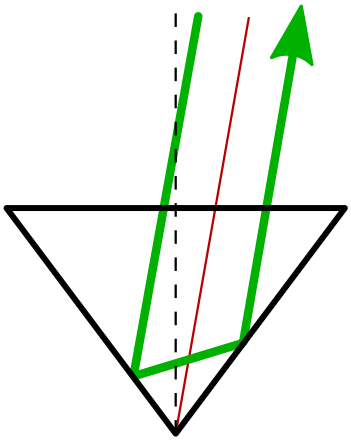

Figure 2.2: The green ray has one of the velocity component parallel to a CCR face, hence two reflections suffice to retroreflect it. The incident and returning rays are parallel and symmetrically displaced with respect to the (red) ray passing by the CCR vertex.

2.1.1 *Basic retroreflectors properties*

Retroreflectors are made of three mutually orthogonal reflecting faces. When the light ray is reflected by a surface, its velocity component normal to the surface is reversed; after three reflections, all its components are reversed and the ray returns back with the same direction. If the velocity vector is parallel to one or two surfaces, then two or one reflections, respectively, suffice to retroreflect the ray. The returning and incident rays will be parallel to each other but spatially displaced, symmetrically with respect to the ray that hit the CCR vertex (see Fig. 2.2).

The measurement of the time that takes for a laser pulse to travel forth and back from the ground station to a CCR (called Round Trip Time (RTT)) gives the range of the vertex. The optical path traveled by all rays is equal to the ray which is reflected at the vertex. As a result, the returning pulse is not spread in time by the single CCR, without altering the precision on the single-shot measurement. However, a systematic error may be introduced if the type of CCR (hollowed or made of dielectric) is not considered. Indeed, dielectric CCRs present an interface that refracts the ray depending on the incident angle and the refractive index. If L is the height of the CCR, from the vertex to the base, θ is the incident angle on the base and n is the refractive index of the dielectric, the correction of the range with respect to hollowed CCR is

$$\Delta R = L\left(\sqrt{n^2 - \sin^2\theta} - \cos\theta\right). \tag{2.1}$$

We can define an input and output aperture of the CCR. The former is actually the shape of the CCR face. We know that any ray with zero incidence

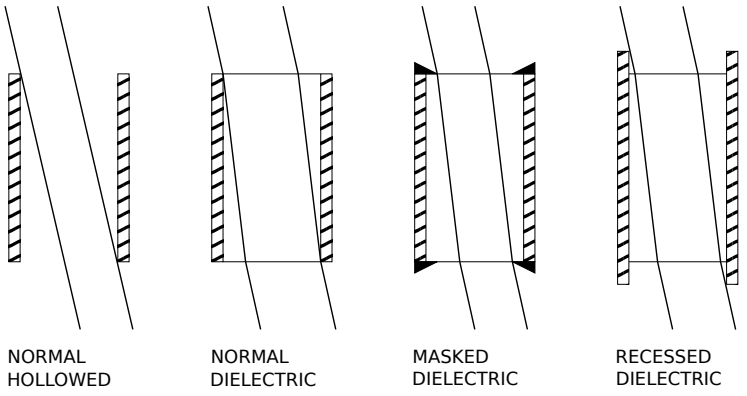

Figure 2.3: Tube analogy for the input and output aperture for several type of CCRs. From left to right: normal hollowed, normal dielectric, masked dielectric, recessed dielectric. Outermost rays are depicted with constant incident angle. Note how the aperture of the dielectric CCR is larger than the hollowed one.

angle and incident in point A will be retroreflected in point B, which is at the same distance from the vertex and on the other side. This imply that the output aperture has the same shape of the input and is rotated by 180 degrees around the vertex. The overlap between the two figures defines the active reflecting area, which is the collection of points in which an incident ray can be reflected back. If the incidence angle θ is not zero then the input and output apertures are reduced by a factor $\cos\theta$ and, since the vertex is not at the center of the input aperture, the output is rotated and shifted by a factor $2L\tan\theta'$, where θ' is the internal incidence angle and it is related to θ by the Snell's law.

A useful and simple approach to visualize the active reflective area is the so called tube analogy (see Fig. 2.3). In this representation, the rays passing through a tube, with length $2L$ and the same section as the CCR face, defines the active area. For solid CCR, the tube should be filled with dielectric. Clearly, the active area is larger for solid CCR than the hollow one at non-zero incident angle, since the rays are bent inside the tube.

The decay of the active area with respect to the incident angle is a feature of the CCR that can be varied using a variety of techniques. Depending on the application the decay can be made more or less narrow. We can define a cutoff angle beyond which the active area is zero. In the tube analogy this depends on the width-to-length ratio of the tube; the larger it is, the smaller is the cutoff angle. To change this ratio either the cube corner is made narrower or a mask is applied over the input aperture. Another technique is to recess the reflector in a cavity of the same shape as the face. For hollow reflector this has the same effect of masking and narrowing the cube corner. Different is the case for a recessed solid CCR, since the displacement is given by the sum of two terms: the container shadows the face with an incident

angle and the refraction happens at the dielectric boundary. For precise SLR measurements, it is preferable to have a narrow active area. This is the case of the LAGEOS, a spherical geodynamic satellite whose surface is covered by 426 CCRs. When illuminated, only a small portion of its cube corners reflect back the light pulse, minimizing the temporal spread of the reflected pulse due to the different RTT of each CCR. The MLRO holds the record precision on the single-shot measurement of the SLR (down to few millimeters), that was reached using LAGEOS (Bianco et al., 2001a,b).

A perfect reflection parallel to the incident beam is not always desirable. The tracking of an orbiting satellite is subjected to a velocity aberration on the returning pulses, which may not return on the ground station. To avoid this scenario, the angle between pairs of reflecting faces is offset of a small amount so that after three reflections the beam is split into two, four or six beams, depending on the number of offset angles, thus enlarging the spot on the ground. Each spot corresponds to a particular order of reflection. If δ is the small offset angle then the beam spreads of an angle $\gamma = \frac{4}{3}\sqrt{6}n\delta$ (Rityn, 1967).

2.1.2 *CCR array*

The majority of satellites are equipped with more than one CCR arranged in an array. Depending on the geometry and purpose of the satellite the shape of the array varies. For geodynamic satellites the array is usually spherical to minimize the temporal spread of the back reflected pulse and maximize the precision of the ranging measurement. As mentioned above, LAGEOS, but also Starlette, Stella, Ajisai, are spherical satellites. Flat rectangular or circular arrays are mostly mounted on high altitude satellites to maximize the active area of the array. For instance, the Global Navigation Satellite System (GNSS) constellation such as GLONASS, Galileo and some Global Positioning System (GPS) satellites are equipped with flat arrays.

In this case, the reflected signal is given by the sum of the amplitudes of the beams reflected by each CCR. Since the laser beam is coherent, the reflections interfere with each other. If all the reflected beams had the same phase, there would be a constructive interference and the total reflected energy would be proportional to the square of the array area. In practice, the small imperfections in the CCR positioning randomize the relative phases. In a first approximation, we may consider the resultant amplitude for a large number of reflected beams N, then the probability distribution for having an amplitude ψ is (Strutt and Rayleigh, 1878)

$$P(\psi)d\psi = \frac{2}{N}e^{-\psi^2/N}\psi d\psi. \tag{2.2}$$

The energy probability distribution is then obtained substituting to the above equation $E = \psi^2$ and $dE = 2\psi d\psi$. The result is an exponential distribution with mean $\overline{E} = N$

$$P(E)dE = \frac{1}{N} e^{-E/N} dE. \tag{2.3}$$

This approximation is exact if these ideal conditions are met:

- the number of reflectors is infinite.
- the amplitude of the reflections is equal between each reflector.
- the coherence length of the incident pulse is infinite.

In practice the approximation still holds if the number of CCRs within the coherence length of the incident pulse is greater than about 10 (Arnold, 1979). Under this condition, we can assume that the intensity of the returning pulse $I_r(t)$ is spread in time with the following equation

$$I_r(t) = \sum_k I_i(t - 2d_k), \tag{2.4}$$

where $I_i(t)$ is the intensity of the incident beam and d_k is the apparent distance of the CCR along the direction of the incident beam.

Temporal spread of back-reflected pulses from Glonass-134

Glonass-134 is part of the Glonass-K1 generation, which is equipped with a holed planar CCR array. The reflectors are distributed over three circles with 37 reflector per each, plus four triplet in the inner part (see Fig. 2.4), for a total amount of 123 CCRs. The most external and internal circles have a radii of 298.1 mm and 230 mm, respectively. During its circular orbit, the satellite corrects its attitude to point its antenna, placed on the hole of the array, towards the Earth center of mass. Considering the fact that the satellite distance from the center of mass of the Earth is constant and knowing the latitute and longitude position of the station, we can calculate the incidence angle of the beam over the array with respect to the measured slant distance of Glonass-134 form the ground station. We now show that for this CCR configuration there are always more than 10 reflectors within the coherence length of the pulse. The maximum angle of incidence on the array is obtained when the satellite elevation angle is zero degrees to the station. Then, the maximum incidence angle is $\arcsin(R_{\text{Earth}}/(R_{\text{Earth}} + D_{\text{Sat}})) \sim 15$ degrees. Assuming for simplicity that, along the line of sight, the number of CCRs are uniformly distributed, we calculate a density of $123/(60\sin(15))\text{CCR/cm} \sim 12.3\text{CCR/cm}$. The temporal coherence of the MLRO pulses is 100 ps FWHM which corresponds to 3 cm of coherence length. Hence, there are 37 CCRs within the coherence length of the pulse, which justify the use of Eq. 2.4.

Given the configuration of the CCRs, we show in Fig. 2.5 the temporal spread of the back-reflected pulse for three different angles of incidence: 0 degrees (blue line), 5 degrees (red line), 10 degrees (yellow line). At normal incidence, the pulse is not changed since the relative distance along the line of sight of the reflectors is much less than the coherence length of the pulse. At higher angles we note the presence of a central depression, due to the hollow on the array, and hence the formation of two peaks, corresponding to the reflection of the closer and further CCRs. As the incidence angle augments the relative distance along the line of sight between the closer and further CCRs increases and hence the two peaks widen the gap.

This effect is deleterious for the measurement of the satellite range, since it introduces a systematic error. The resulting ranging measurement becomes underestimated if the pulse at the detection is not at the single-photon regime. Indeed, the detector will be triggered at the rising edge of the first peak with high probability.

2.2 CHANNEL LOSSES AND MEAN NUMBER OF PHOTONS AT THE SATELLITE

In a satellite-to-ground link, losses are mainly given by the limited receiving area of the telescope with respect to the dimension of the back reflected spot at ground level. Weather conditions may prevent the transmission of optical wavelengths for the presence of low thick cumulus clouds. However, considering the cases in which a link can be established, the atmosphere contributes mainly in the last 10 km next to the ground station. For our purposes, the channel losses are needed for the estimation of the mean number of photons μ leaving the reflectors array. By knowing the detection rate at the receiver R_{det}, the overall channel transmittance t_{all} and the pulse repetition rate $\nu = 100$ MHz we have

$$\mu_{\text{sat}} = R_{\text{det}}/(t_{\text{all}}\nu). \tag{2.5}$$

We model the overall transmittance as given by three terms, $t_{\text{all}} = t_{\text{diff}}t_{\text{atm}}t_{\text{rec}}$, with t_{diff}, t_{atm} and t_{rec} being respectively the transmittance due to diffraction losses, atmospheric losses and receiver apparatus losses. In this section, I will introduce to the models for the estimation of the atmospheric and diffraction transmittance. The receiver transmittance will be discussed in the next section.

2.2.1 *Atmospheric losses*

In the near-ultraviolet to visible (300 to 700 nm), atmospheric attenuation is dominated by aerosol (Mie) scattering, a minor role is played by molecular and ozone absorption (see Fig. 2.6). In the near-infrared beyond 700 nm the

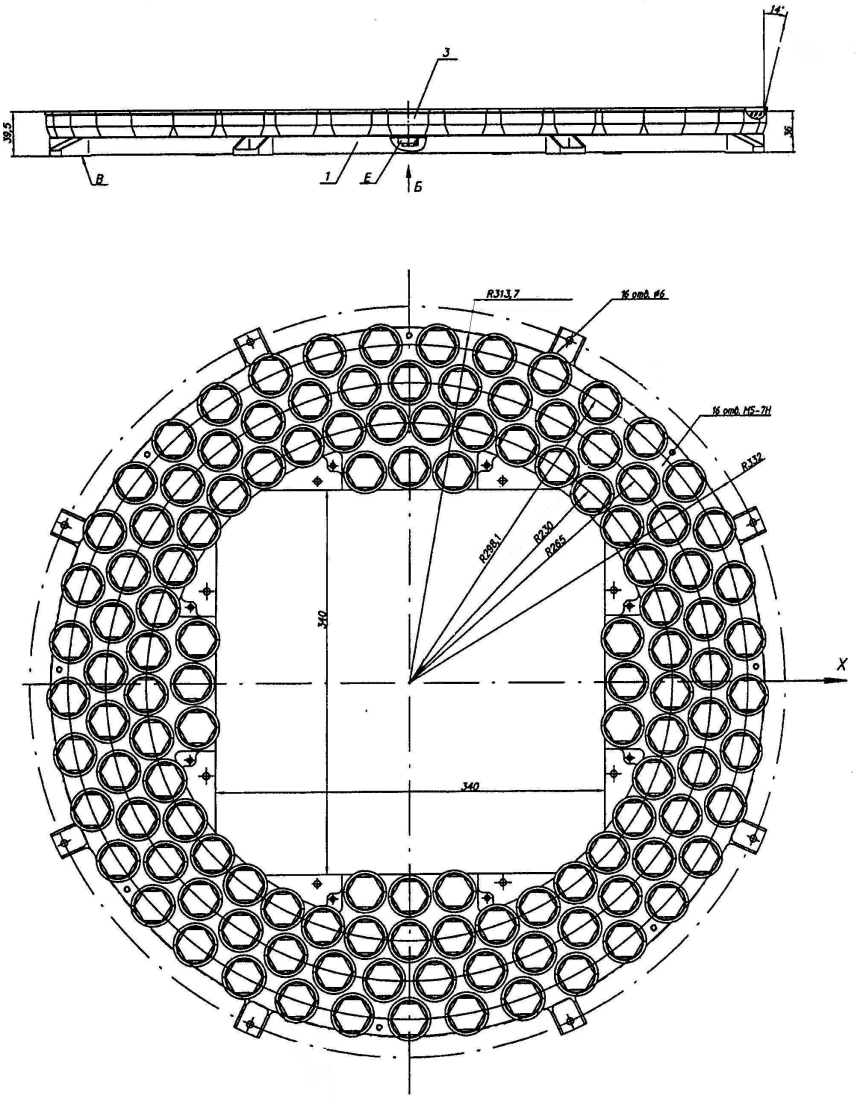

Figure 2.4: CCR array of a Glonass K1. The CCRs are distributed over three circles with 37 reflector per each, plus four triplet in the inner part. Image taken from the official ILRS website (*Glonass K1 corner cube retroreflector array*)

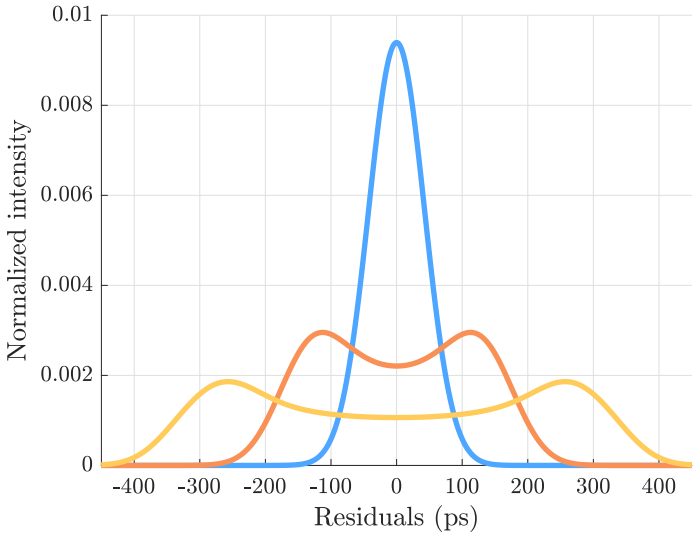

Figure 2.5: Simulated temporal pulse shape after the retroreflection from the CCR array of Glonass-134. Colors represent different incident angle: 0 degrees (blue line), 5 degrees (red line), 10 degrees (yellow line).

atmosphere absorption is modulated by strong absorption features of various molecular constituents of the atmosphere, notably water vapor, oxygen, and carbon dioxide. Atmospheric seeing conditions vary widely from day to day and from site to site. However, the attenuation coefficient decreases approximately exponentially with height according to

$$\sigma_{\text{atm}}(\lambda, V, h) = \sigma_{\text{atm}}(\lambda, V, 0) \exp\left(-\frac{h}{h_{\text{scale}}}\right), \tag{2.6}$$

where $\sigma_{\text{atm}}(\lambda, V, h)$ is the attenuation coefficient at wavelength λ and altitude h for sea level visibility of V, while $\sigma_{\text{atm}}(\lambda, V, 0)$ is the value at sea level, and $h_{\text{scale}} = 1.2$ km is a scale height. The one-way atmospheric transmission over a slant range to a satellite from a site at an altitude h_{t} above sea level is then given approximately by

$$t_{\text{a}}(\lambda, V, h_{\text{t}}) = \exp\left[-\sigma_{\text{atm}}(\lambda, V, 0) h_{\text{scale}} \sec\theta_{\text{zen}} \exp\left(-\frac{h_{\text{t}}}{h_{\text{scale}}}\right)\right], \tag{2.7}$$

where θ_{zen} is the zenith angle of the satellite in the reference frame of the station.

Even if the sky appears relatively clear, sub-visible cirrus clouds are overhead about 50% of the time at most locations. A global study of cirrus cloud thickness yields a mean of 1.3 km when the cirrus are presents (Degnan, 1993). The dependence on the wavelength, for optical thickness less than 0.5 (attenuation coefficient times cloud thickness), is negligible from near ultraviolet to infrared light. Experimentally, the cirrus transmittance is given by the equation

$$t_{\text{c}} = \exp\left(-0.14\left(t \sec\theta_{\text{zen}}\right)\right), \tag{2.8}$$

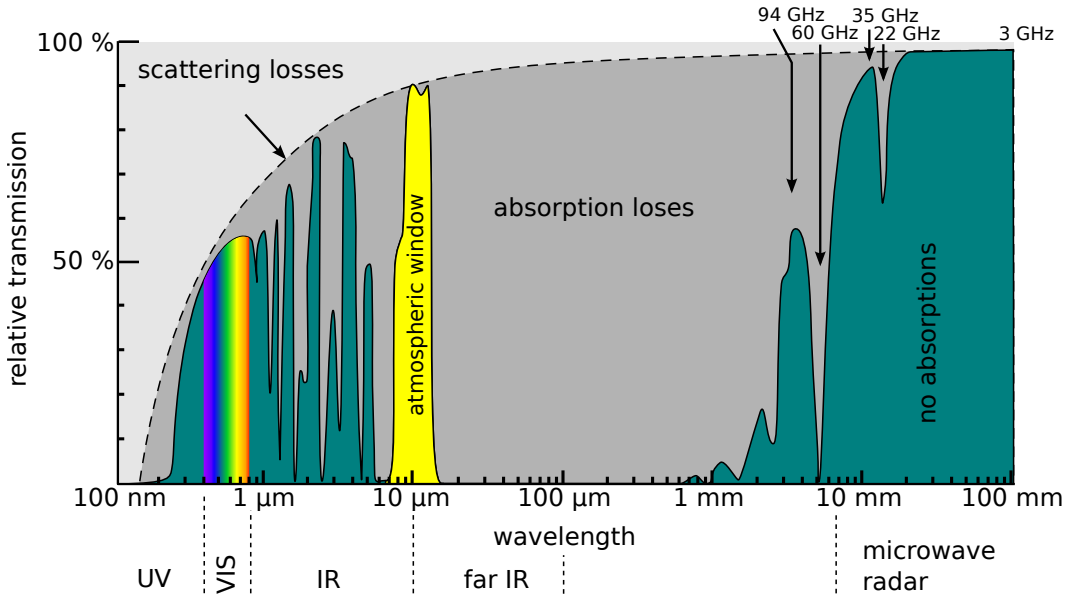

Figure 2.6: Relative atmospheric transmission as a function of the wavelength.

where t is the cirrus cloud thickness. Finally the atmospheric transmittance is give by $t_{\text{atm}} = t_{\text{a}} t_{\text{c}}$.

2.2.2 *Geometrical attenuation*

The large distance between the satellite and the receiving ground station (500-20000 km) contributes to enlarge the spot size of the retroreflected beam, due to diffraction of the optical wave. The analysis of the Far Field Diffraction Pattern (FFDP) is necessary to estimate the divergence angle of the beam and the intensity pattern. The development of a precise theoretical model is challenging since the FFDP depends on the shape of the CCR and on the polarization of the reflected beam, which vary from sector to sector if the surfaces are not coated. The best option is to consider the use of experimental measurement done in laboratory before the satellite launch. Unfortunately, these data are not always available for all satellites. In the following, I will present two methods for estimating the diffraction losses. The former approximates the FFDP as a top-hat distribution, the latter goes through the calculation of the FFDP given the model for the output polarization from the reflector.

Top-hat approximation

The parameter that characterize the efficiency with which a CCR back-reflects the light is the cross-section σ_{cc}. The cross-section gives the area of a perfectly reflecting sphere that, if replaced by the actual CCR, would reflect the beam with equal solid angle and intensity. Such a sphere would reflect the same amount of energy if its illuminated area is equal to the active area of the CCR

A_{cc}. Then, by imposing the back-reflected beam to have a solid angle Ω, we find the total area to be $4\pi/\Omega$ times A_{cc}. Considering the reflectivity ρ of the cube corner we have

$$\sigma_{cc} = \rho A_{cc} \left(\frac{4\pi}{\Omega} \right). \tag{2.9}$$

In this context $\frac{4\pi}{\Omega}$ is also known as the on-axis retroreflector gain.

For a flat array of N CCRs, in the hypothesis that Eq. 2.4 is valid, the cross-section becomes

$$\sigma_{arr} = N\sigma_{cc}. \tag{2.10}$$

If we assume that the back-reflected beam has a top-hat intensity distribution over the angular displacement from the propagation direction, the portion of light that enters the telescope at a slant distance R from the satellite is

$$t_{diff} = \frac{A_{Tel}}{R^2\Omega}. \tag{2.11}$$

If the σ_{arr} is provided, along with the dimensions of the array and the CCRs, the above equations allow us to estimate the transmittance of the channel t_{diff} due to diffraction losses (Dequal et al., 2016).

The drawback of this model is the assumption of a top-hat pattern of the FFDP. In practice the situation is much more complicated and the resulting FFDP is nothing but constant over the solid angle of reflection. In the following section, I will present an estimation of t_{diff} based on a model of the FFDP for Total Internal Reflection (TIR) CCR (Murphy and Goodrow, 2013), which is the type of reflectors mounted on the GLONASS satellites we are considering.

Model of the FFDP for Glonass-134 and 131

As a first approximation, the reflected beam can be modeled by a gaussian beam from a circular aperture whose area is A_{cc}. Then the FFDP is the familiar Airy function given by

$$\frac{\sigma(x)}{\sigma_{cc}} = \left(\frac{2J_1(x)}{x} \right)^2, \tag{2.12}$$

where $J_1(x)$ is the Bessel function of the first kind of order one and

$$x = kR_{cc} \sin\theta, \tag{2.13}$$

being $k = 2\pi/\lambda$ the wavenumber, R_{cc} the radius of the aperture and θ the incidence angle of the beam. The Airy pattern consists of a central lobe surrounded by several weaker rings. Under this assumption, we can define the effective solid angle of the FFDP considering the angle from the beam center to the first null, which is given by equation

$$\theta_{null} = 1.22\frac{\lambda}{2R_{cc}}. \tag{2.14}$$

Hence, the solid angle is approximately $\Omega = \lambda^2 / A_{cc}$ containing the 84% of the energy. Substituting this equation into Eq. 2.9 we find

$$\sigma_{cc} = \rho \left(\frac{A_{cc}}{\lambda} \right)^2 . \tag{2.15}$$

Thus σ_{cc} scales quadratically with the active area. Considering an array with N CCRs, in the hypothesis that Eq. 2.4 is valid, we expect the solid angle not to be changed since the back-reflected beams do not interfere with each other. Hence, we have

$$\sigma_{arr} = N\rho \left(\frac{A_{cc}}{\lambda} \right)^2 . \tag{2.16}$$

Interestingly, in terms of diffraction losses, Eqs. 2.15 and 2.16 tell us that it is better to have a single CCR with N times A_{cc} instead of an array with N small active area CCRs.

It is interesting to note that at an arbitrary incidence angle the active area reduces by a factor (Degnan, 1993)

$$\eta(\theta) = \frac{2}{\pi} \left(\arcsin \xi - \sqrt{2} \xi \tan \theta_{ref} \right) , \tag{2.17}$$

where θ_{ref} is the internal refracted angle that obey to Snell's law

$$n \sin \theta_{ref} = \sin \theta, \tag{2.18}$$

and ξ is a quantity given by

$$\xi = \sqrt{1 - 2 \tan^2 \theta_{ref}}. \tag{2.19}$$

The resulting fall off of the optical cross-section is

$$\sigma_{eff}(\theta) = \eta^2(\theta) \sigma_{cc}. \tag{2.20}$$

Fig. 2.7 shows the fall off of the optical cross-section for a hollow ($n = 1$) and quartz ($n = 1.455$) corner cube. The cut-off angles are respectively 30 and 40 degrees.

To go a step further in the estimation of the FFDP, one should also consider that the polarization of the beam varies dependently on the order of the reflections. In general, the aperture of a CCR can be divided in 6 sectors in which the beam is reflected by the three faces in a different order. From each sector the beam may exit with a different polarization and, furthermore, it may have a relative phase between the other. In this case, the intensity pattern is given by the following equation as a function of the angular displacement from the propagation direction

$$I(\chi, \eta) = \sum_{j=0}^{1} \left| \int_{A_{cc}} du dv S_j(u, v) \exp\left(i\phi(u, v)\right) \exp\left(ik\left(\chi u + \eta v\right)\right) \right|^2 , \tag{2.21}$$

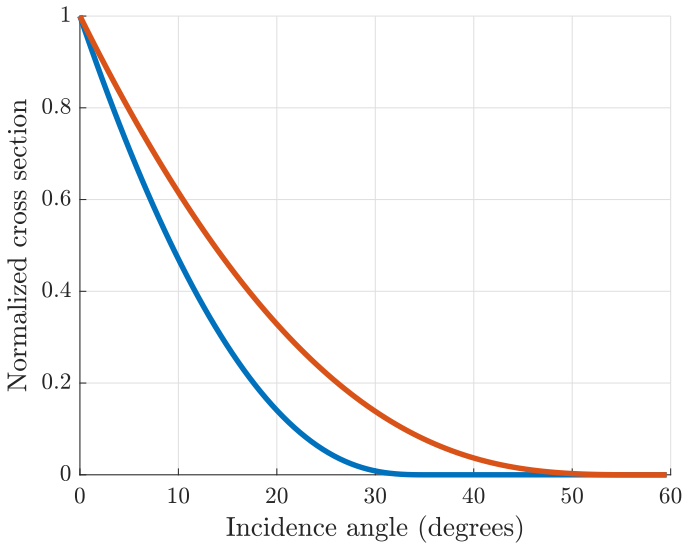

Figure 2.7: Optical cross-section as a function of the incident angle, for hollow (blu line) and dielectric (orange line) CCRs.

where χ and η represent angular coordinates in the far field. The aperture amplitude of the j-th polarization S_j and phase ϕ are functions of the coordinates u and v in the aperture plane, with $k = 2\pi/\lambda$. We can calculate the central irradiance of the Airy disk using Eq. 2.21 with $S = 1/(\sqrt{2}A_{cc})$ and $\phi = 0$, resulting in $I(0,0) = \pi^2 R^2$. On the contrary, if we consider a solid uncoated TIR CCR we obtain $I(0,0) \sim 0.264\pi^2 R^2$ (Murphy and Goodrow, 2013). Hence, its central irradiance is 26.4% that of the Airy disk. Considering also the reflection losses (5%) we have a relative central irradiance of 24.6%. The irradiance pattern is also different: it has a central lobe, similar to the Airy disk, surrounded by other six weaker lobes placed on the vertices of an hexagon. The lobes are displaced from the center of the FFDP by $\theta \simeq 1.4\lambda/D_{cc}$, with D_{cc} the diameter of the reflector aperture. The intensity profile is shown in Fig. 2.8: the dashed and dotted lines represent two orthogonal cuts of the diffraction pattern. For comparison the solid line shows the Airy disk profile.

Since the central intensity peak of a circular aperture of area A depends on the power P_0 incident on it via $I(0,0) = P_0 A/(\lambda^2 R^2)$, the ratio between the power collected by the telescope and P_0 is

$$t_{diff} = 0.246 \frac{A_{cc} A_{Tel}}{R^2 \lambda^2}. \tag{2.22}$$

Moreover, we have to account for the velocity aberration due to the relative motion between the receiving station and the satellite. This aberration gives an offset of the FFDP with respect to the line of sight. As a result the telescope will not collect the peak intensity of the pattern. For satellites at an altitude of about 20.000 km the magnitude of the offset angle is about 26 μrad and it is almost constant during the orbit (Degnan, 1993). The CCRs mounted on GLONASS have a diameter D_{cc} of 26 mm, hence the lateral lobes are displaced

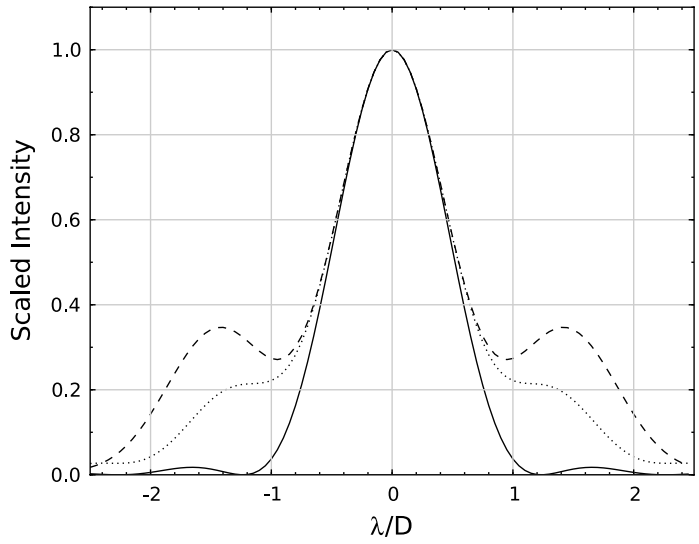

Figure 2.8: Intensity profile of the FFDP. Orthogonal cuts (dashed and dotted) through the normal-incidence far-field diffraction pattern for the TIR CCR under linear input polarization, showing the similarity of the central peak to the scaled Airy function (solid). The cuts correspond to the upper-left panel. From (Murphy and Goodrow, 2013).

of about 29 μrad from the central peak, which is almost equivalent to the velocity aberration. For this reason, we may assume the telescope to be collecting the lateral lobes of the FFDP with 30% the irradiance of the central peak. The correct estimation becomes

$$t_{\text{diff}} = 0.074 \frac{A_{\text{cc}} A_{\text{Tel}}}{R^2 \lambda^2}. \tag{2.23}$$

2.3 EXPERIMENT DESCRIPTION

2.3.1 *Setup*

The MLRO is equipped with a Nasmyth-Cassegrain telescope of 1.5 m diameter (see Fig. 2.9). The first large mirror (M1) has a parabolic metal coated surface with reflectivity of about 95%, at wavelength 532 nm. The second mirror (M2) has a convex hyperbolic surface and is coated in order to have a 99.5% reflectivity, at wavelength 532 nm. The light is then redirected by other five flat coated mirrors, also with 99.5% reflectivity at wavelength 532 nm, to the optical tables in the laboratory below. Mirrors from M4 to M7 will be referred to as the coudé path.

The light path for quantum experiments is in parallel to the setup for SLR activity. It uses the same laser source, a Nd:YAG mode-locking master oscillator that generates train of pulses at 100MHz repetition rate (wavelenght

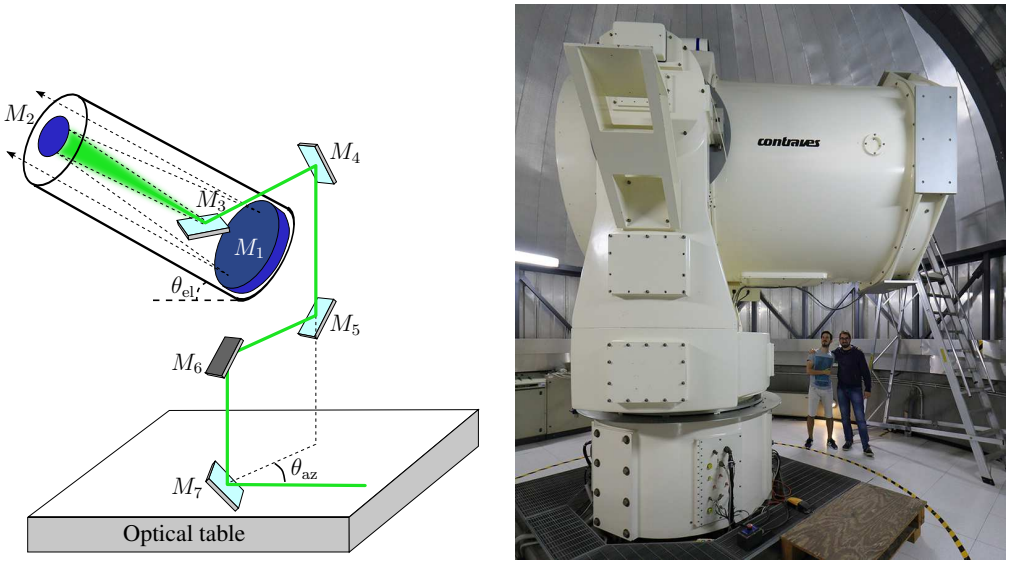

Figure 2.9: Schematic of the telescope and coudé path mirrors **(left)**. Picture of the 1.5 m Nasmyth-Cassegrain telescope **(right)**.

1064 nm), and at the end merges together with the SLR line just before entering the coudé path. Fig. 2.10 shows a schematic of the optical table dedicated for the generation of the quantum line and SLR pulses. A Faraday isolator is placed after the laser source to avoid unwanted retro-reflected beam entering the cavity of the laser. The beam then passes a Brewster plate trasmitting only the p polarization (in this case the horizontal polarization). Then a Pulse Peaker Regeneratice Amplifier (PPRA) is placed to select a pulse out of 10^7. The PPRA is an optical cavity where a Quarter Wave Plate (QWP), two QWP Pockels cells, two Brewster plates and a flash lamp pumped Nd:YAG crystal. This set the pulse frequency of the SLR line at 10 Hz. Only vertical polarized light can enter into the PPRA, hence a Half Wave Plate (HWP) is placed before it to rotate from horizontal to vertical polarization. In this mode only the SLR line is active. The quantum line starts at the transmission of the Brewster plate, hence when both lines are needed the HWP is rotated to split the beam. The transmitted beam is then focused on a Second Harmonic Generator (SHG) crystal to produce a train of pulses at wavelenght 532 nm with 120 mW mean optical power and a 100 MHz repetition rate. Instead, the reflected beam, that exit the PPRA, passes two single pass amplifiers and then generates the second harmonic inside a phase-matched non linear crystal, becoming the SLR pulse at wavelength 532 nm, with 1 W mean optical power and a 10Hz repetition rate. This generation mechanism allows the two photon streams to be locked together and well synchronized with the atomic clock of MLRO.

The two beams pass to the receiving optical table (see Fig. 2.11). The SLR pulse goes through a divergence system, that controls the divergence angle after the telescope, and two beam splitters, one coupling the returning beam to the receiver apparatus and one merging the quantum and SLR paths. The

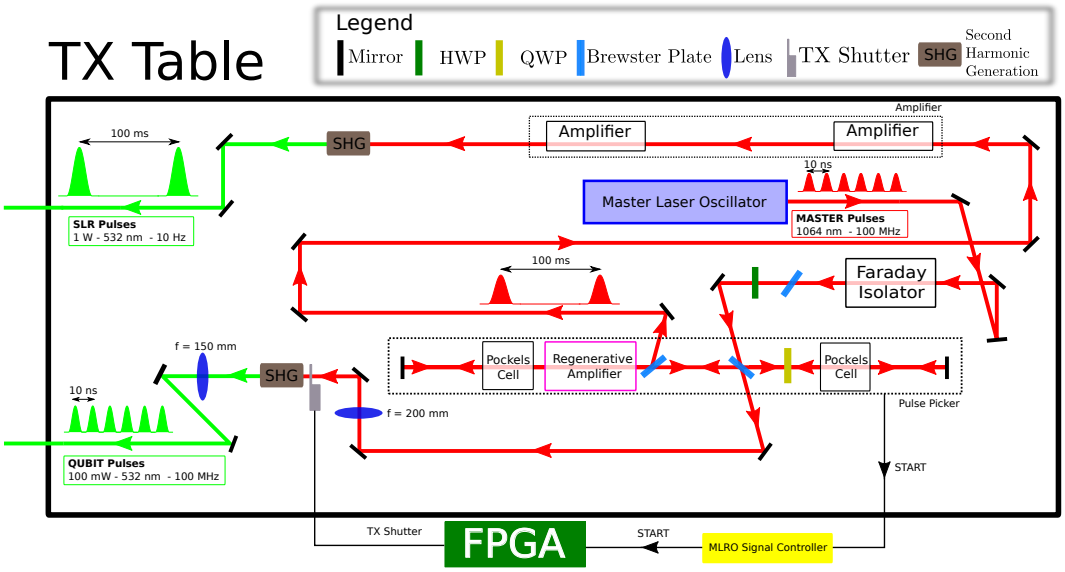

Figure 2.10: Transmission table

receiving set up of the SLR pulse is composed by a micro channel plate for the detection of the pulses and a camera for alignment purposes. On the quantum line, a lens with 500 mm of focal length is placed to collect the beam which is diverging and has a beam width of about 1 inch. A beamsplitter couples the returning photons to the detecting apparatus. Finally a diverging control module is placed.

In this experiment we interchanged two different receiving apparatuses on the quantum line. For Glonass-134 we used a Single Photon Avalanche Photodiode (SPAD) from Micro Photon Devices (MPD) coupled to the returning beam, while for Glonass-131 we used two detectors in parallel to compare their performances: the MPD detector and a Photon Multiplier Tube (PMT) from Hamamatsu Photonics. In the latter case, we coupled the two detectors at the output ports of a 50:50 beam splitter. The MPD detector has a small active area of about 200 μm of diameter but high quantum efficiency at 532 nm (almost 50%), whereas the PMT has a large active area of 22 mm and 10% quantum efficiency. In both cases we added a 3 nm bandpass filter centered at 532 nm to lower the background. The best detector is a compromise between the active area diameter and the quantum efficiency. Indeed, small active area requires a good optical coupling of the returning beam into the detector. In our case, this is not trivial since the beam returning after the coudé path has a diameter of 50 mm. A beam reducer of about 30X factor must be introduced; however, this does not guarantee that all the light collected by the telescope will impinge on the active area, since high reduction factors introduces large shifts on the focal plane for a small movement of the telescope. On the contrary, a large active area is not much subjected to the pointing error of the telescope. In our setup the pointing error is subjected to weather conditions. In particular, the presence of the wind introduces small but rapid oscillations

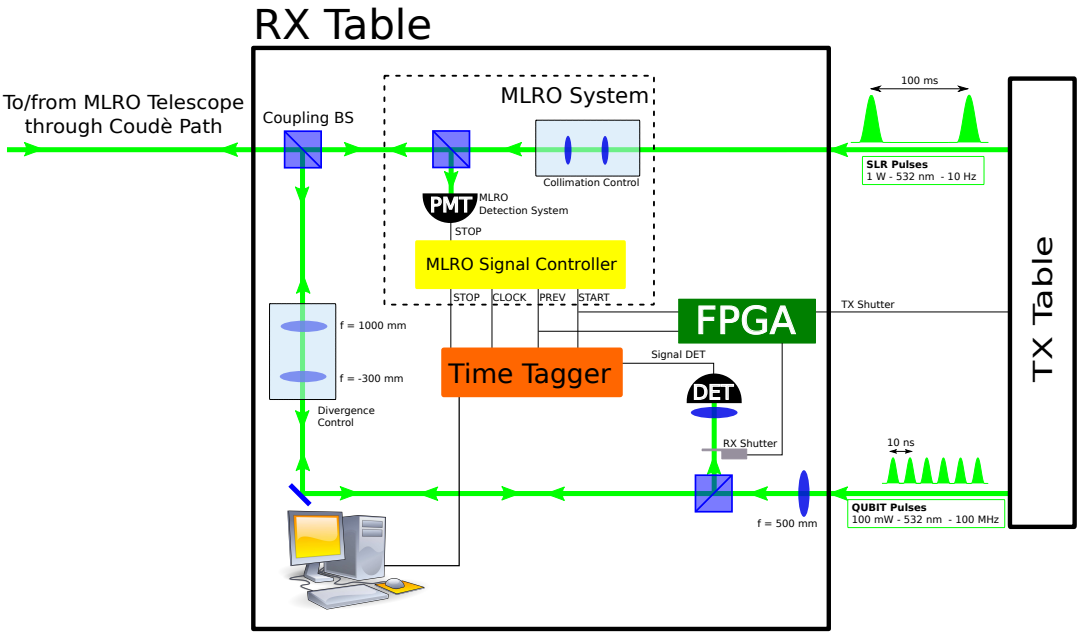

Figure 2.11: Receiving table

of the telescope. At MLRO small adjustments of the pointing are provided by a manned control during the passage of the satellites, which is clearly not sufficiently reactive and has a too low correction frequency.

Neglecting pointing errors, we can estimate the transmittance of the receiver apparatus, t_{rec}, considering the reflectance of the mirrors, the presence of beam splitters and the detector quantum efficiency. Both receiving apparatuses have a common path that goes from M1 to M7 and two 50:50 beam splitters: one next to the coudé path and the other separating the transmission line from the receiving part. The transmittance of this part is measured to be of 13%. Hence, for the measurements with Glonass-134 we have $t_{\text{rec}} = 6.6\%$, whereas with Glonass-131 we have $t_{\text{rec}} = 3.3\%$ and $t_{\text{rec}} = 0.66\%$ for MPD and PMT, respectively.

2.3.2 *Alignment of the setup*

During the experiment both the quantum and SLR lines are active. While the quantum line is used to send and collect the single photons reflected from the satellites, the SLR pulses provide precise estimation of the slant distance of the satellite and hence the expected time of arrival of the reflected single photons. The SLR line is regularly aligned by the MLRO operators using a pinhole, just before the coudé path, and the camera looking at the retroreflection of corner cube inside the mirror M2. Using these two references we align the up-going beam of the quantum line on the SLR line over the entire coudé path and telescope. The quantum line enters the coudé path by a reflection on a beam splitter; by adjusting its tip and tilt angles, we regulate the direction with

which the beam enters the coudé path. Moreover, the beam should pass at the center of the coudé path; to this aim, a mirror placed before the beam splitter provides the translation by changing the incident point on the beam splitter. The procedure goes as follows: the pinhole is inserted along with a CCR before the coudé path, that reflects the beam of the quantum line on the camera. The furthest mirror is tilted to center the spot on the center of the camera. Since it is the furthest, a small tilt produces a large translation on the camera. Then, the beam splitter is adjusted to center the spot of 50 mm diameter on the pinhole. The procedure is repeated until the spots on the camera and on the pinhole are both centered. A further check of the alignment is done by removing the pinhole and the CCR located before the coudé and placing the CCR on M2. The reflection on this CCR should impinge at the center of the camera.

The receiving apparatus is aligned to the down-going beam by mean of a star. This procedure is subjected to the pointing accuracy of the telescope. Small adjustments of the telescope are provided by the operator in order to center the spot of the star on the camera. Once the telescope is well pointed, the receiving detector is translated to maximize the detection rate. If the spot on the focal plane is smaller than the active area, the maximum count rate should be constant for a small translation of the detector, while it should decrease linearly with further translation.

2.3.3 *Synchronization between quantum and SLR lines: optical and electric signals*

Being generated by the same laser, the quantum and SLR train of pulses are naturally locked together. However, the two receiving setups must detect different returning pulses and be repaired by back-reflections of both up-going pulses. To accomplish this task a receiving shutter for each detector and a transmission shutter on the quantum line are temporized through a Field Programmable Gate Array (FPGA). The duty cycle is shown in Fig. 2.12. Since the round-trip-time of a pulse to GNSS is around 130 ms, the time period is set to 200 ms. In the first half of the time period, the transmission shutter is open to send the pulses towards the satellite: at the beginning there is the fire of the first SLR pulse, followed by 100 ms of pulses from the quantum line. Meanwhile, the receiving shutters are closed to protect the detectors. In the second half, the transmission shutter is closed but a second SLR pulse is fired anyway, hence the receiving shutters are closed for the first 5 ms and then opened till 10 ms before the end.

The electronic signals from the detectors are time tagged via a Time to Digital Converter (TDC) with 1 ps of resolution (QuTAG from QuTools), which is synchronized with the MLRO atomic clock. For convention we refer to as Stop signal, a detection from the SLR receiving apparatus. Moreover, other signals are time tagged for further data analysis: the Start signal, which is generated by a photodiode on the transmitting port of the first mirror after

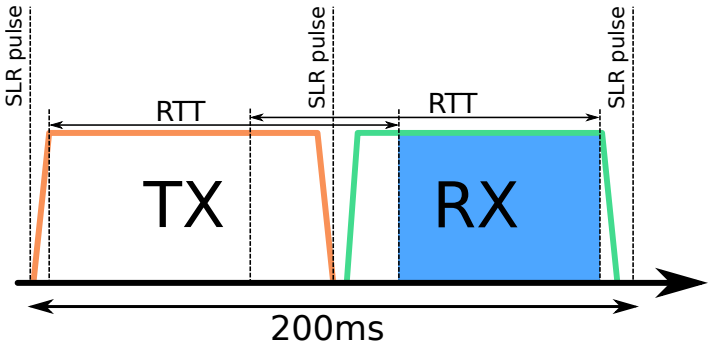

Figure 2.12: Duty cycle of the transmission and receiving shutters.

the amplification stage of the SLR pulse, the signal of the transmission and the receiver shutter. All the shutters are synchronized with the Start signal via the FPGA. The time difference between the Stop and Start signals gives the measurement of the actual round-trip-time of the SLR pulse.

2.3.4 *Data analysis and results*

In this section, I report the results obtained on two passages of the GLONASS satellites 134 and 131 (Space Vehicle Number: 802 and 747, respectively).

As we have seen in the description of the duty cycle, every 200 ms the receiving detector is open for less than 100 ms. In Fig. 2.13 we show a stacked histogram of the time difference between a detection from MPD and the previous even Start signals. The red bars highlight the time in which the receiving shutter is closed. In this phase the count rate is the lowest since the optical path is blocked. Note that the count rate remains constant, meaning that the shutter is blocking all the back-reflected light from the up-going beams that are present in the first 100 ms, when the transmission shutter is open. Hence, these detections are due to the intrinsic dark count rate of the detector plus the background light in the laboratory. In the remaining time, the receiving shutter is open. We expect the SLR pulse to return back, and subsequently the 100 MHz pulses, after a round-trip-time from the previous even Start, which is about 130 ms. Hence, in the first part of the open phase, which lasts about 30 ms, we do not expect the detection of the reflected pulses. This phase is highlighted in green in Fig. 2.13 and is characterized by an exponential decay of the count rate due to the fluorescence of the last beam splitter. This happens because of its atoms that have been excited by the passage of the previous up-going SLR pulse, occurring at time 100 ms. Finally, the blue bars highlight the time in which we expect the return of the pulses, while the receiving shutter is open. For further analysis we do not consider detection out of this region. Moreover, we discard a time window of 6 μs around the re-

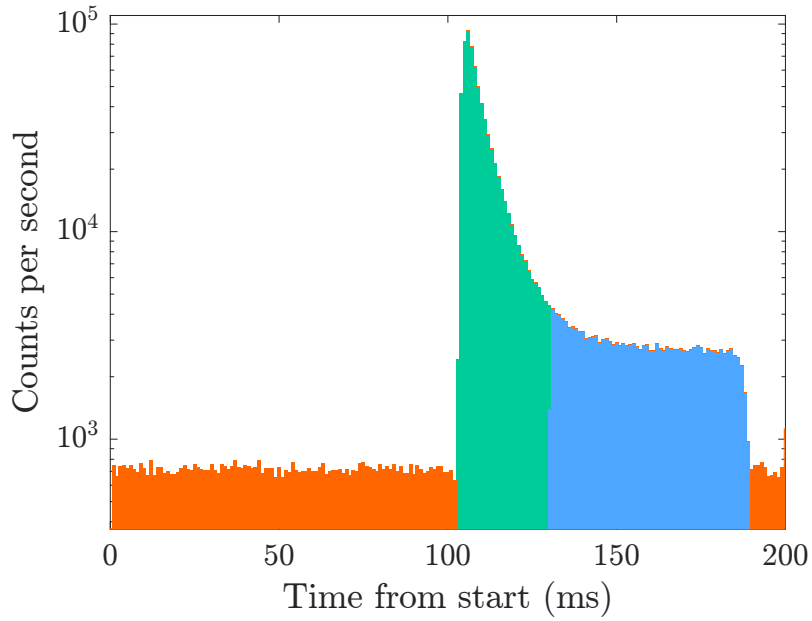

Figure 2.13: Glonass-134 histogram 200 ms

turning time of the SLR pulse, which triggers also the receiver of the quantum line.

To prove the detection of the reflected single photons among all the background noise, we calculate the histogram of the time difference between the measured and expected time of arrival of a photon reflected from the satellite. The photons from the background will show a flat distribution over the 10 ns time window, which is the period between two consecutive pulses of the quantum line. If the photons from the satellite are detected, the distribution will show a peak over the expected time of arrival. The Stop and Start signals provide the measurement of the slant satellite distance over time. As a model for this measurement we use the ephemeris of the satellite, which gives the predicted instantaneous position of the satellite taking into account the variation of the Earth gravitational field, plus a polynomial taking into account small deviations form the prediction. A linear regression is done to find the parameters of the best polynomial that matches the measurements. From this model we precisely determine the instantaneous round-trip-time, $\mathrm{RTT}(t)$. Since the single photons from the satellite are locked to the SLR pulses, the function $t_{\mathrm{ref}} = \mathrm{RTT}(t_i) + t_i$, with t_i the i-th multiple of 10 ns from the first Start signal, gives the expected time of arrival of the single photons. Then, for each single photon detection we calculate the time difference with the closer t_{ref}.

In a single passage of Glonass-134 we had two distinct acquisitions corresponding to the maximum and minimum slant distance of the satellite from the ground station. These two measurements are temporally separated by

about one hour. In particular, the first acquisition lasted about 2 minutes, with mean slant distance of about 20,200 km, whereas the second one lasted about 5 minutes, with mean slant distance of 19,500 km.

In Figs. 2.15 and 2.14 we show the detection rate of the 100 MHz pulses (that from now on I will refer to as the signal detection rate) from Glonass-134 of the first and second acquisitions, respectively. The signal detection rate was estimated in the following way. We divided the whole acquisition in time intervals $\mathcal{I}_k$ of duration $\tau = 5$ s. For each interval we made the histogram (see Figs. 2.16 and 2.17) of the time difference between the tagged detection t_{meas} and the expected time of arrival of the photon t_{ref}. Then, we chose a time window $w = 600$ ps and $w = 400$ ps, for the first and second acquisition respectively, centered around t_{ref}, much larger than the detector jitter (≈ 40 ps) since the retroreflected pulses are temporally spread by the CCR array, and estimated the number of photon detection N_{det} as the difference of the total and background counts within the window. The background was uniformly distributed within the 10 ns period (see Figs. 2.16 and 2.17), therefore we estimated its rate counting the detection over a time window which is at least 1 ns away from t_{ref}. Finally, the signal detection rate was obtained via $R_{\text{det}} = N_{\text{det}}/(\tau\delta)$ where $\delta = 0.3$ is the duty cycle of the communication protocol. Then, we discarded the time windows $\mathcal{I}_k$ with $R_{\text{det}} < 30$ Hz, to filter out acquisition with low SNR. Such selected time windows gave the integrated histogram shown in Figs. 2.16 and 2.17.

At the end of such analysis, we obtained a detection frequency $\overline{R}_{\text{det}} \approx 59$ Hz, a SNR of 0.41 and a mean number of photons at the satellite $\overline{\mu}_{\text{sat}} \approx 16.1$, for the first acquisition of Glonass-134. In this case we used a signal time window w of 600 ps due to the larger temporal spread. For the second acquisition of Glonass-134, we obtained a mean detection frequency $\overline{R}_{\text{det}} \approx 58$ Hz, a SNR of 0.53 and mean number of photons at the satellite $\overline{\mu}_{\text{sat}} \approx 14.5$.

In the passage of Glonass-131, we used a slightly different receiver setup. Instead of using a single receiving detector, we placed an MPD detector and a PMT detector (detection efficiency, 10%; active diameter, 22 mm; H7360-02, Hamamatsu Photonics), coupled both to the down-going link with an additional 50:50 beam splitter. In this way we could compare the performances of the two detectors. Using the same analysis described above, we obtained the signal detection rate presented in Fig. 2.18. We noticed a good correlation between the signal detection rate of the two detectors, although the PMT shows a much lower rate, since its quantum efficiency is five times lower than the one of MPD. We then discarded the time windows with low signal detection rate, obtaining two comparable values for $\overline{\mu}_{\text{sat}}$ for the two detectors. The results are summarized in Tab. 2.1. We noted that the MPD has about five times the signal rate of the PMT, as expected for the higher quantum efficiency. Also the SNR of the MPD is two times the SNR of the PMT, since the jitter on the time of arrival of the photons is lower.

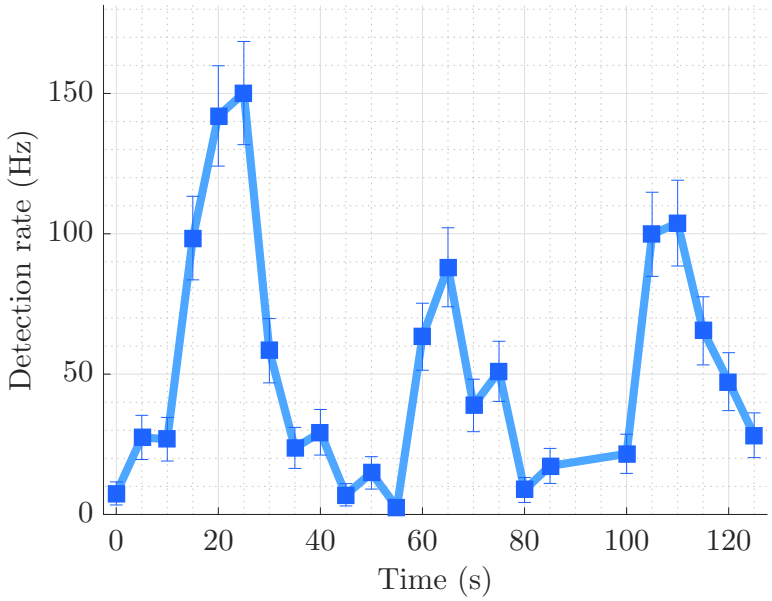

Figure 2.14: Detection rate from Glonass-134 at 20,200 km slant distance. Each point is calculated integrating over an acquisition time window $\mathcal{I}_k$ of $\tau = 5$ s.

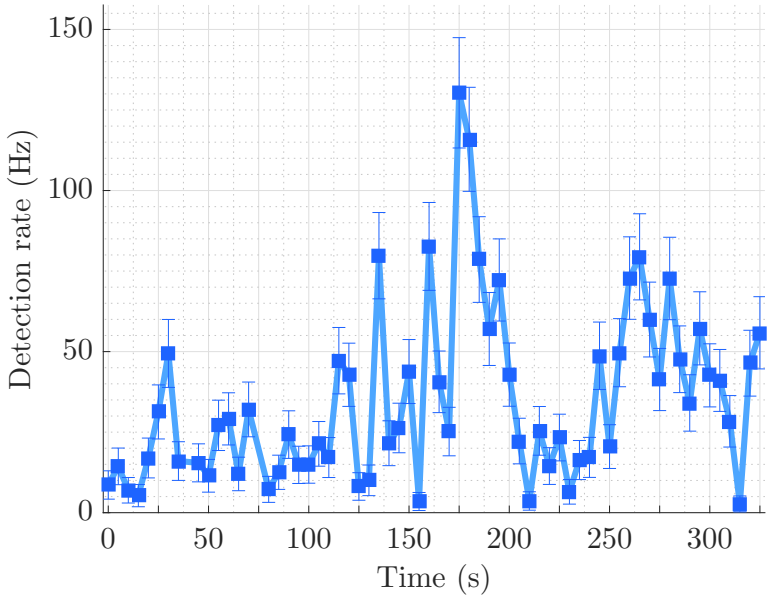

Figure 2.15: Detection rate from Glonass-134 at 19,500 km slant distance. Each point is calculated integrating over an acquisition time window $\mathcal{I}_k$ of $\tau = 5$ s.

By reducing the bin width in Figs. 2.16 and 2.17 we highlight the shape of the peaks confirming that we are able to resolve the temporal distribution of the returning pulse. As mentioned in the subsection 2.1.2, this is the "signature" of Glonass-134 which is given by the particular design of the CCRs array. In these two acquisitions, the corresponding incidence angles are 5 degrees and 9 degrees, respectively. In Fig. 2.19, we compare the actual data (bars) with the simulated temporal shape (solid line), using Eq. 2.4 and adding the

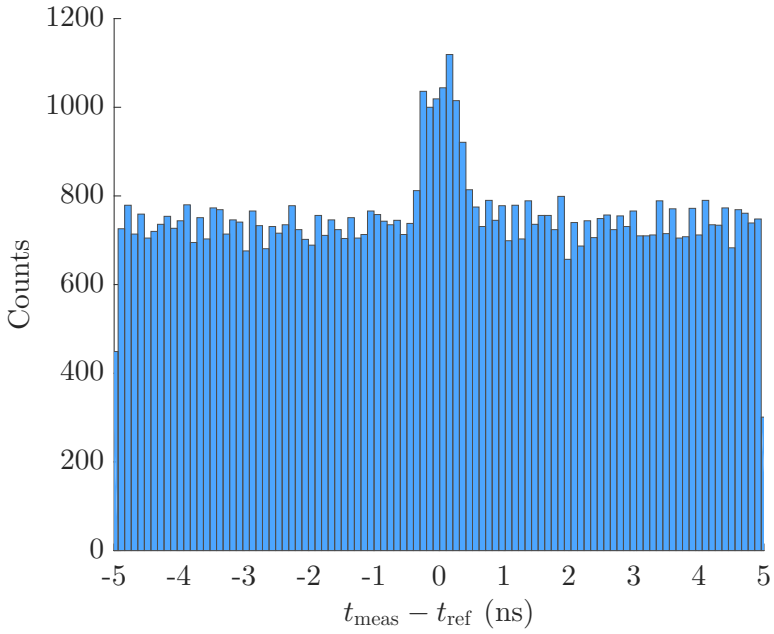

Figure 2.16: Histogram of residuals between the measured and the expected time of arrival of the photons, from Glonass-134 at a slant distance of 20,200 km. Here, we consider acquisition time windows $\mathcal{I}_k$ with detection rate $R_s >$ 30 Hz.

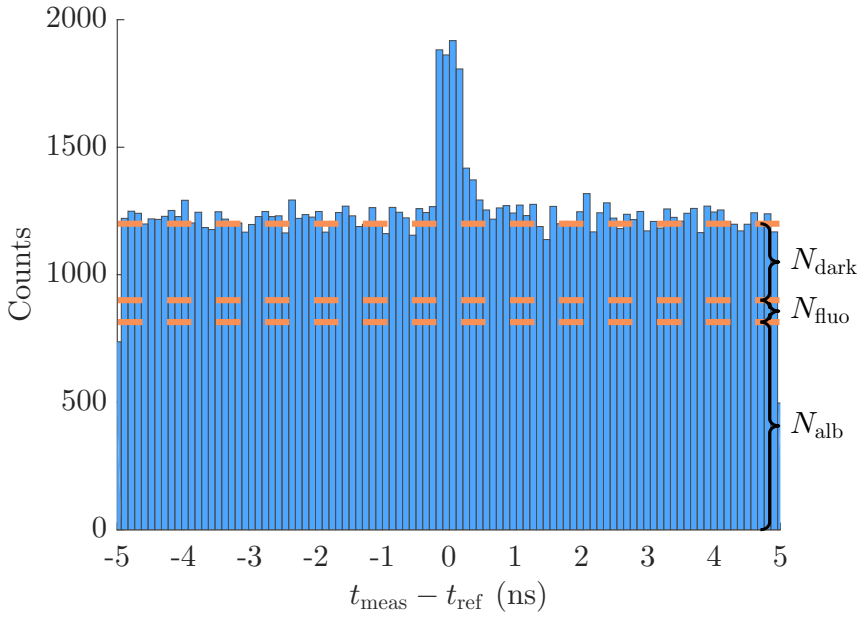

Figure 2.17: Histogram of residuals between the measured and the expected time of arrival of the photons, from Glonass-134 at a slant distance of 19,500 km. Here, we consider acquisition time windows $\mathcal{I}_k$ with detection rate $R_s >$ 30 Hz. Each bin is 100 ps wide. Dashed lines show how the background is distributed among the field of view and satellite albedo (N_{alb}), fluorescence (N_{fluo}) and dark count rate of the detector (N_{dark}).

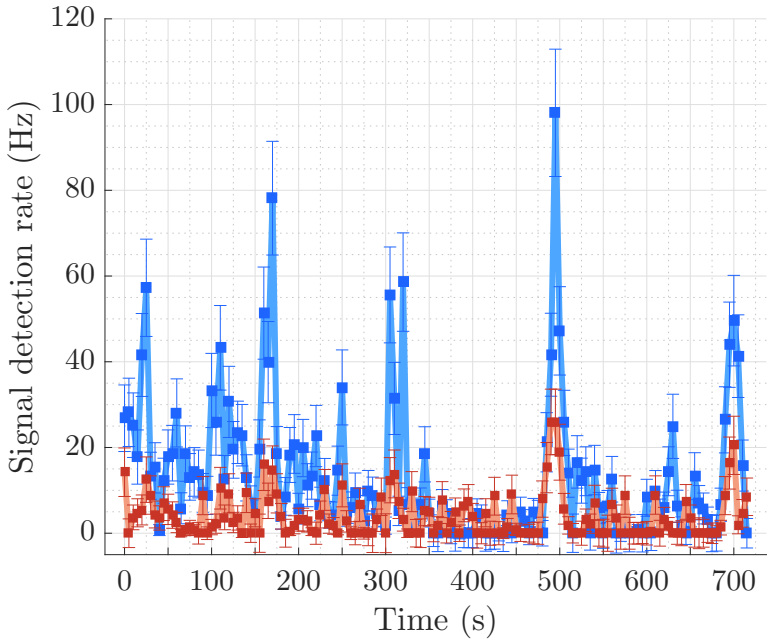

Figure 2.18: Signal detection rate for Glonass-131. The blue solid line refers to the MPD detector, while the red one refers to the PMT.

estimated background. From the model, the calculated peak-to-peak distance is 250 ps and 430 ps, respectively, in agreement with the experimental estimation.

As shown in the work by Otsubo *et al.* (Otsubo, Appleby, and Gibbs, 2001), GLONASS flat CCRs array exhibits particular temporal distribution determining higher error in the laser ranging measurement, in which the mean number of photons at the receiver is usually much greater than one. The authors (Otsubo, Appleby, and Gibbs, 2001) observed the "signature" of the GLONASS satellites by integrating one year of data acquisition. On the con-

Satellite	Glonass-134		Glonass-131	
Slant distance (km)	19,500	20,200	20,250	
Detector	MPD	MPD	MPD	PMT
$\overline{R}_{\mathrm{det}}$ (Hz)	58	59	27	6
SNR	0.53	0.41	0.43	0.21
$\overline{\mu}_{\mathrm{sat}}$	15	16	15	16
l_{down} (dB)	62.1	62.5	62.6	62.6
l_{rec} (dB)	11.8	11.8	14.8	21.8

Table 2.1: Summary of the results. Mean signal detection rate $\overline{R}_{\mathrm{det}}$, mean photon number at the satellite $\overline{\mu}_{\mathrm{sat}}$, mean down-link losses l_{down}, receiver losses l_{rec}. Here we defined $l_{\mathrm{down}} = -10\log_{10}(t_{\mathrm{diff}}t_{\mathrm{atm}})$ and $l_{\mathrm{rec}} = -10\log_{10}(t_{\mathrm{rec}})$.

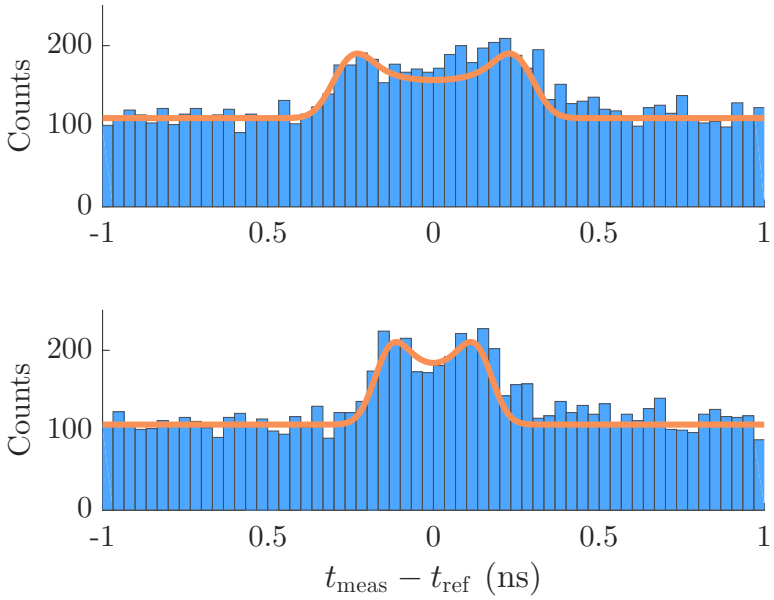

Figure 2.19: Histogram of residuals between measured and expected time of arrival of the photons for Glonass-134 at 20,200 km (top) and 19,500 km (bottom). The incident angle of the beam on the array is about 9 degrees and 5 degrees, respectively. Here we integrate on time windows I_k with high detection rate to highlight the temporal spread of the back reflected impulse. Based on our model, the temporal peak to peak distance is about 430 ps and 250 ps for incident angles of 9 degrees and 5 degrees, respectively (continuous lines)

trary, our result shows that, using single photons detectors and high repetition source, the temporal distribution of the pulse can be measured, even with low mean number of photon at the satellite and short data integration time. A more accurate measurement could be done using a mean number of photons of about one at the receiver. We note that this measurement could even be used to determine the orientation of the array and hence the attitude of the satellite, which is of critical importance for the processing of GNSS data (Kirchner, G., Grunwaldt, L., Neubert, R., Koidl, F., Barschke, M., Yoon, Z., Fiedler, H., Hollenstein, 2013; Montenbruck et al., 2015; Pearlman, Degnan, and Bosworth, 2002).

2.3.5 *Towards quantum communication from GNSS*

Based on these results, we can estimate the performance of a transmitter and receiver needed for the realization of quantum communication protocol from GNSS satellites. For practical QC we target a SNR of the order of 100 and a detection rate larger than 10 kHz.

At the receiver, the background affecting the SNR can be significantly reduced with respect to the present experiment in a dedicated QC application. In our work, the background was estimated by using the detections distribu-

tion on the 200 ms period, shown in Fig. 2.13 for the passage of Glonass-134 at 19,500 km. The blue bars corresponds to the counts in which we expect the transmitted photons to arrive at the detector. A large part of these counts are due to noise. The intrinsic dark count rate of the detector amounts to $N_{\text{dark}} \approx 700$ Hz. They are estimated in the first 100 ms of the period, when the receiving shutter is closed. This noise could be almost halved, reaching the intrinsic dark count rate of the detector, by optimizing the optical isolation of the detector from room light. Another source of noise is the fluorescence that occurs when the upgoing SLR pulse passes through the optical elements in common with our optical path. The intensity of the fluorescence light reduces exponentially in time with half-life that depends on the material. A remaining tail is included in the blue region and amounts to $N_{\text{fluo}} \approx 195$ Hz. This noise can be eliminated, since this pulse is useless for the protocol and can just be avoided. The remaining, and predominant, detections are due to satellite albedo and background of the field of view. This noise is uniformly distributed in time in the blue region and amounts at $N_{\text{alb}} \approx 1.9$ kHz. By using a bandpass filter of 0.3 nm instead of 3 nm, these background detections would be reduced by an order of magnitude. Moreover, a dedicated receiver would avoid signal losses due to beam splitters. Indeed the satellite tracking may be done using a different wavelength. With respect to our setup, this would enhance the signal by a factor of 4, although correspondingly augmenting N_{alb}. Adopting these solutions at the receiver we expect a SNR and a detection rate raised of a factor 10 and 4, respectively.

Regarding the transmitter, we consider an active source on the satellite with a mean photon number per pulse close to 1. Compared to the current result, this involves a signal reduction of about a factor 15. However, the downlink coupling efficiency can be greatly enhanced by using an appropriate telescope. We consider a down-going beam with 10 μrad of angular aperture, shrinking the beam spot on ground and using a point ahead to compensate for velocity aberration as recently demonstrated in (Liao et al., 2017). This would reduce the diffraction losses of 20 dB with respect to the channel losses estimated above. The temporal spread due to the reflector array would not be present, allowing for a narrower temporal filter w that could be chosen considering only the jitter of the detector ($\approx$40 ps). Moreover, with 40 ps jitter, the repetition rate could be increased to more than 1 GHz, thus enhancing the detection rate. With these expedients, the expected SNR and detection rate are of the order of 100 and 10 kHz, respectively.

2.4 DISCUSSION

This work demonstrates the first exchange of few photons per pulse ($\mu_{\text{sat}} \simeq 10$) along a channel length of 20,000 km, from Glonass-134 and Glonass-131 to MLRO, reaching a SNR about 0.5 and a detection rate around 60 Hz. We evaluated the requirements needed for a transmitter mounted on a GNSS satellite

and a ground receiver for the realization of QC between the two terminal. Our findings demonstrate that QC from GNSS satellite is feasible with current state-of-the-art technology.

Extending QC to GNSS is of primary importance for secure communications at the global scale but it is also a resource for fundamental tests of physics in space (Agnesi et al., 2018). Indeed, QC from satellite opens the possibility of testing the foundations of quantum mechanics in the space scenario, as envisaged in theoretical studies (Rideout et al., 2012) and mission proposals (Jennewein et al., 2014; Joshi et al., 2018; Scheidl, Wille, and Ursin, 2013; Ursin et al., 2008), and already realized in actual implementations (Ren et al., 2017; Vedovato et al., 2017; Yin et al., 2017) at the LEO distance. A channel length of over 20,000 km could enable the design of new experiments that test the validity of quantum mechanics at higher orbits and permit the use of satellites following highly elliptical orbits. Such orbital characteristics might be of key importance to observe gravity-induced effects on quantum interference, (Brodutch et al., 2015; Bruschi et al., 2014; Zych et al., 2012), that could shed light on the interplay between general relativity and quantum mechanics, thus validating physical theories and placing bounds on phenomenological models. Concluding, our results pave the way for new applications of quantum technologies and fundamental experiments of physics exploiting QC from high-orbit satellites, which may be implemented on next-generation GNSS constellation.

We are not to tell nature what she's gotta be.
She's always got better imagination than we have.

— Richard Feynman

3

WHEELER DELAYED CHOICE EXPERIMENT EXTENDED ON A SPACE CHANNEL

Gedankenexperiments have consistently played a major role in the development of quantum theory. A paradigmatic example is Wheeler's delayed-choice experiment, a wave-particle duality test that cannot be fully understood using only classical concepts. In this Chapter, I describe our implementation of Wheeler's idea along a satellite-to-ground channel. I will introduce the problem of the wave-particle duality with a brief summary of the history of the theory of light. Then, I will explain the main idea of Wheeler's delayed choice and its experimental implementations. The last sections are dedicated to the design and results of our experiment.

3.1 BRIEF HISTORICAL OVERVIEW OF THE THEORIES OF LIGHT

Many theories of light have been developed over the centuries. These can be categorized into two main groups: the theories based on the wave nature of light, and the theories based on its particle-like behavior. The leading theory on the particle nature of light was put forward by Isaac Newton (Newton, 1730). He stated that light was made of corpuscles emitted by a source in all directions and traveling along a straight line. His argument against the wave theory was based on the fact that light travels along straight lines while waves are known to bend around obstacles. His theory was well suited for explaining the reflection of light, but was wrongly predicting the refraction inside a denser medium, due to the hypothetical greater gravitational pull inside the material, which should accelerate the particles.

His reputation helped the particle theory of light to prevail during the 18th century, being preferred to the wave interpretation introduced by Robert Hooke in 1665 (Hooke, 1665) and mathematically formalized by Christiaan Huygens in 1690 (Huygens, 1690). Huygens proposed that light was emitted in all directions as a series of waves propagating in a medium called the Luminiferous ether. The wave-like behavior successfully predicted the

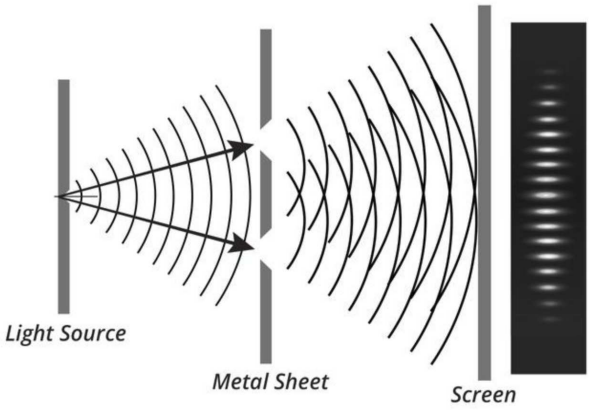

Figure 3.1: Young double-slit experiment.

diffraction, polarization and interference properties of light. In his interpretation, the propagation of the wavefront was explained as the sum of spherical waves being emitted at every point along the wavefront (Huygens-Fresnel principle).

In 1803 a landmark experiment was performed by Thomas Young (see Fig. 3.1). In his work, he let the sunlight pass through a small hole in a paper. The resulting thin light beam was then split in half alongside a paper card and let it propagate toward a distant screen. As predicted by the wave theory, the expected interference fringes showed up on the screen. Indeed, based on the Huygens-Fresnel principle, the experiment can be interpreted in the following way: two spherical waves generate from the two small slits going towards the screen; since the waves generate from the same wavefront of the thin light beam, their phase is equal. On the screen the waves overlap and the intensity pattern that emerges is given by the resulting wavefront; there are points on the screen in which the two waves have the same (opposite) phase, hence constructively (destructively) interfering. In presence of a constructive interference there will be a bright spot on the screen while it will be dark in case of destructive interference. This experiment played a major role in the general acceptance of the wave theory of light.

The success of the wave-based theory continued, being then unified with the electromagnetic theory. The first evidence that light was related to electromagnetism came in 1845, when Michael Faraday discovered that the plane of polarization of linearly polarized light is rotated when the light rays travel along a magnetic field with the same direction in the presence of a transparent dielectric. This effect suggested that light might be some form of disturbance propagating along magnetic field lines. Faraday's work inspired James Clerk Maxwell to study electromagnetic radiation and light. Maxwell unified the theories of electricity and magnetism with his famous equations. Surprisingly, his theory predicted the existence of self-propagating electromagnetic waves traveling through space at a constant speed, in agreement to the previ-

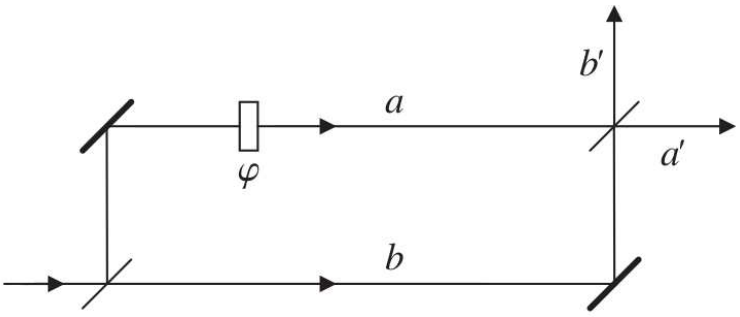

Figure 3.2: Mach-Zehnder interferometer.

ously measured speed of light. From this, Maxwell concluded that light was a form of electromagnetic radiation.

The particle nature of light revived at the beginning of the 20-th century when, looking for a solution to the ultraviolet catastrophe, Planck proposed the discretization of the spectral energy of the black body radiation. The discrete packets were then interpreted by Bose and Einstein as being real particles, then called photons, leading to the explanation of the photoelectric effect (Einstein, 1905). In this framework, a photon is an energy quantum which moves without splitting and can only be absorbed or produced as a whole. These massless corpuscles of light carry a specific amount of energy $E = h\nu$ with h being Planck's constant and ν the light's frequency. Hence an apparent paradox was emerging about the nature of light: interference, diffraction requires the light to be a wave, whereas the photoelectric effect requires it to be an indivisible particle.

With the advent of quantum mechanics it has been accepted that particle and wave behaviors are complimentary (Bohr, 1928) in the sense that they can be revealed only in different experimental contexts and not simultaneously. In a Young-type double slit experiment a single quantum of energy is in a superposition of states, being both at the right and at the left slit. Hence, when detectors are placed just after the slits, the photon is found only at one of the slits, since it can be absorbed as a whole by one of the detectors. At which slit the photon is found is completely random. Moving the detectors far away from the slits, we lose the information from which slit the photon has passed through and hence the photon preserves its superposition state of passing by both slits. In this case, an interference pattern is measured since the photon propagated through both slits, as it was a wave. In 1924, de Broglie postulated that also all massive particles behave as waves. The wavelength associated with a particle with momentum p is given by $\lambda = h/p$. This wave-particle duality was confirmed experimentally through diffraction of an electron beam at a nickel crystal (Davisson, 1928).

To be more precise, consider the setup shown in Fig. 3.2, equivalent to a double-slit experiment. Single photons enter one at a time a Mach-Zehnder interferometer via a semitransparent mirror, working as a 50-50 Beam Splitter

(BS). The two possible paths of the photon are labeled by a and b being the reflected and transmitted arms, respectively. The relative phase difference between the arms is represented by ϕ. The quantum state of the photon is a superposition of the two path states $|a\rangle$ and $|b\rangle$:

$$|\psi\rangle = \frac{1}{\sqrt{2}}\left(|b\rangle + e^{i(\phi+\pi/2)}\,|a\rangle\right), \tag{3.1}$$

being the additional phase $\pi/2$ due to the reflection. By placing two detectors just after the BS, it is possible to measure in which path the photon is traveling. The detectors will fire one at a time, finding the photon only in one of the two arms, in agreement with its particle characteristic. The state ψ determines the probability of finding the photon in one or the other path. By using the Born's rule, it is found $P_a = P_b = 1/2$. If the two paths are recombined on a second BS with outgoing paths a' and b', the quantum state will be

$$|\psi\rangle = \cos\frac{\phi}{2}\,|a'\rangle - \sin\frac{\phi}{2}\,|b'\rangle\,. \tag{3.2}$$

The probabilities of finding the photon in arm a' or b' are given by $P_{a'} = \cos^2\frac{\phi}{2}$ and $P_{b'} = \sin^2\frac{\phi}{2}$. The ϕ-dependent interference fringes indicate that the system traveled through the interferometer by both arms, reflecting its wave character. Based on the experimental setup one or the other property of light (being particle or wave) emerges.

In summary, the observed phenomena led to two alternative classical interpretations of light: being either a wave or a particle. Clearly, these are irreconcilable point of view since a "classical" particle cannot split in two after passing a plate as a "classical" wave may do. Currently, we do not have an intuitive and comprehensive "classical" interpretation of the whole light phenomena and we may never find it since the phenomena that we, as human being, are used to deal with have nothing to do with what happens at the discrete (quantum) level of the nature.

3.2 ORIGINAL FORMULATION OF WHEELER'S DELAYED-CHOICE WAVE-PARTICLE DUALITY GEDANKENEXPERIMENT

In a series of works around 1980, Wheeler proposed a gedankenexperiment to highlight the inherently nonclassical principle behind wave-particle complementarity (Wheeler, 1983). The fundamental question he was trying to answer was: does the photon decide before entering the interferometer whether to behave like a wave or a particle? Even if this may be too naïve to be true, it is something that one cannot exclude a priori.

The setup is illustrated in Fig. 3.3. The **top** panel shows the initial phase of the experiment where a single photon enters a Mach-Zehnder interferometer via a half-silvered ($\frac{1}{2}S$) mirror in which it can travel through two arms: 2a and 2b. This time, the observer chooses whether to put a second $\frac{1}{2}S$ mirror

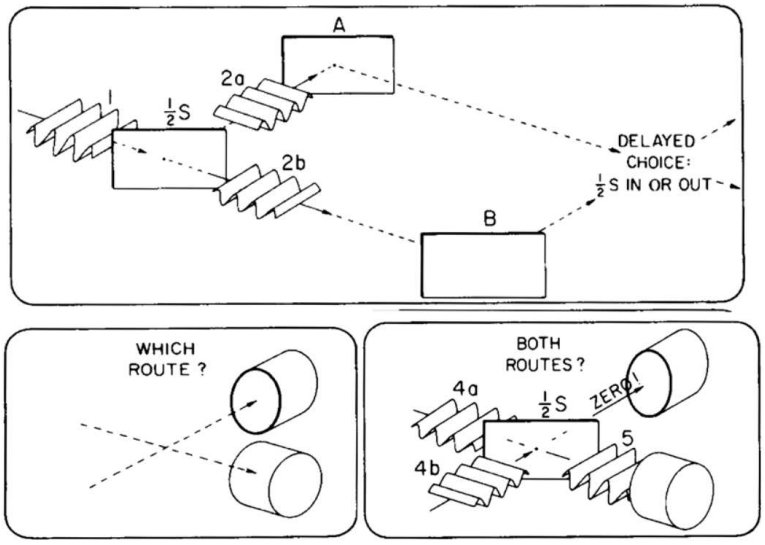

Figure 3.3: Original scheme of Wheeler's delayed-choice gedanken experiment with a single-photon wave packet in a Mach-Zehnder interferometer. **Top**: The second half-silvered mirror ($\frac{1}{2}S$) of the interferometer can be inserted or removed at will. **Bottom left**: When $\frac{1}{2}S$ is removed, the detectors allow one to determine through which path the photon propagated. Which detector fires for an individual photon is absolutely random. **Bottom right**: When $\frac{1}{2}S$ is inserted, detection probabilities of the two detectors depend on the length difference between the two arms. From Wheeler, 1983.

placed before the two detectors after the photon has entered the interferometer. In this sense, the observer makes a delayed-choice. If the observer decides to exhibit the particle nature of the photon, he leaves out the beam splitter (**bottom left** panel) since only one detector at a time will go off. Otherwise, he inserts it to not directly measure which path the photon chose (**bottom right** panel). Assuming the paths to be identical with each other, the photon will always end in only one of the two detectors due to constructive interference, hence revealing the wave-like behavior.

To rule out any causal influence from the entering in the interferometer to the choice of the observer, which might instruct the photon to behave as a particle or as a wave, the two events should be space-like separated. Furthermore, it is conceptually important to use true single photons rather than thermal light. This is because the indivisible particle nature of single photons guarantees that the two detectors will never click at the same time. Otherwise, one could explain the results by what is often called a semiclassical theory of light, where light propagates as a classical wave and is quantized only at the detection itself (Paul, 1982).

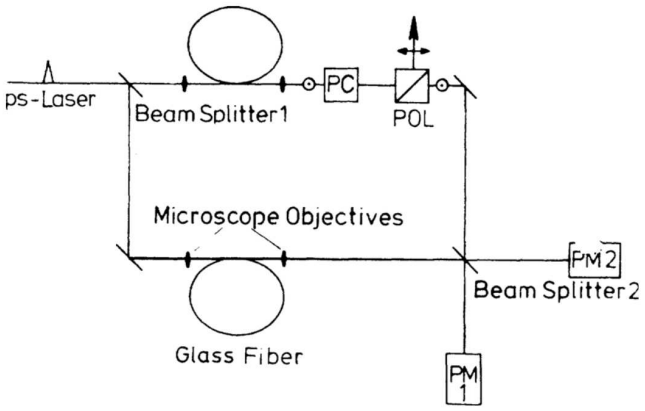

Figure 3.4: Setup of a delayed-choice experiment by Hellmuth et al., 1987. The combination of a Pockels cell (PC) and a polarizer (POL) in the upper arm of the interferometer was used as a shutter. From Hellmuth et al., 1987.

3.3 EXPERIMENTAL REALIZATIONS

Several proposals for an experimental implementation of the Wheeler's delayed-choice have been formulated for different quantum systems, including neutron interferometer (Greenberger et al., 1983; Miller, 1983; Miller and Wheeler, 1983) and photon interferometer (Alley et al., 1983).

One of the first photonic realizations have been performed by Hellmuth and collaborators (Hellmuth et al., 1987). The setup is illustrated in Fig. 3.4. The photons are generated by an attenuated picosecond laser with a mean number of photons per pulse of 0.2. The two arms of the Mach-Zehnder interferometer are made by 5 m glass fiber with a travel time of about 20 ns, which is the maximum delay time for the choice. The choice on the type of measurement is done by a Pockels cell (PC) and a polarizer (POL), that combined together behave as a shutter on the upper arm. A voltage applied on the Pockels cell rotates the polarization state of the photon so that it is reflected by the polarizer. Hence a measurement on which path the photon chose corresponds to a closed shutter, since only the photon that chooses the lower path will be detected. Vice versa, the open shutter will let the photon interfere on the second BS. The rise time of the Pockels cell was 4 ns, short enough to implement the choice when the photon was already inside the interferometer.

The experiment was run into two configurations: normal mode in which the choice was done when the photon was not already inside the interferometer and the delayed mode in which the choice was delayed. The results have shown no difference in the statistics of both modes, in agreement to the predictions of quantum mechanics. The main shortcomings of this experiment is the absence of a true source of single photons and of a random choice.

The first experimental implementation in which true single photons were used was realized by Baldzuhn and co-workers (Baldzuhn, Mohler, and Mar-

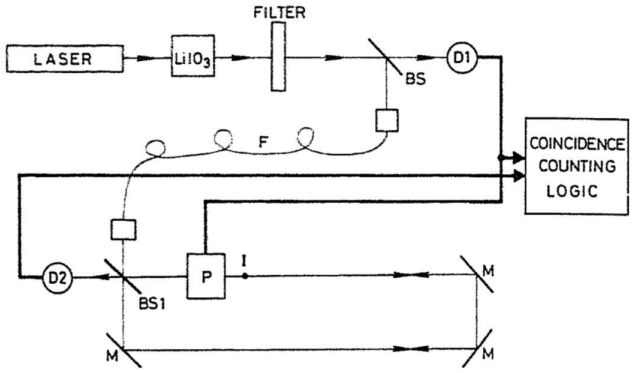

Figure 3.5: Setup of the delayed-choice experiment by Baldzuhn, Mohler, and Martienssen, 1989. True single photons were implemented using a single photon source based on SPDC. From Baldzuhn, Mohler, and Martienssen, 1989.

tienssen, 1989). They used a heralded single photon source based on Spontaneous Parametric Down Conversion (SPDC) (Friberg, Hong, and Mandel, 1985). The layout of the experiment is shown in Fig. 3.5. The detector D1 was used to herald the presence of the signal photon and also to trigger a Pockels cell placed in the interferometer. The signal photon, instead, was injected in the Sagnac interferometer by mean of an optical fiber. The wave-like or particle-like behaviors were exhibited choosing the operating mode of the Pockels cell. If the Pockels cell is continuously turned off, the polarization is not rotated neither for the photon propagating in the clockwise direction nor for the one propagating in the counterclockwise direction (a). In case of a continuous turn on of the Pockels cell, both the clockwise and counterclockwise photon change polarization such that the new state is orthogonal to the previous (b). In both cases (a) and (b), interference is observed since the two paths have the same polarization. On the contrary, if the Pockels cell is turned on when the photon reaches the reference point I and then kept on till the detection, only the counterclockwise photon changes its polarization. Hence the two paths can be distinguished via the measurement of the photon polarization.

The experimental results showed that if the Pockels cell was continuously on or off, one observed an interference pattern. This corresponds to the photon's wave-like behavior. On the other hand, if the Pockels cell was switched on at the time when the photon passed the reference point I, no interference pattern was observed. This corresponds to the particle-like behavior of the photon.

The delayed choice aspect was implemented delaying the injection of the interferometer by a optical fiber F, so that the voltage applied on the Pockels cell could be changed when the photon was at the reference point. However, the space-like separation between the choice of the measurement and the entering of the photon into the interferometer was not implemented in this experiment.

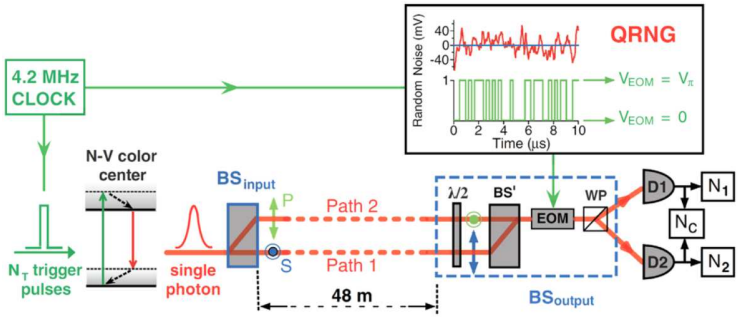

Figure 3.6: Layout of the setup by Jacques et al., 2007. Single photons were generated by NV color centers in diamond. A 48-m-long polarization interferometer and a fast EOM, controlled by a QRNG, were used to fulfill the relativistic space-like separation condition. From Jacques et al., 2007.

More recently, Jacques realized a delayed-choice wave-particle experiment fulfilling the requirements of single-particle quantum state as well as space-like separation between the choice of measurement and the entry of the particle into the interferometer (Jacques et al., 2007, 2008). As shown in Fig. 3.6, the setup consists of a single photon source based on nitrogen-vacancy (NV) color centers in diamonds (Kurtsiefer et al., 2000), a 48-m-long polarization interferometer and a Electro-Optic Modulator (EOM) controlled by a Quantum Random Number Generator (QRNG). The random choice were generated from the amplified shot noise of a white light beam.

To ensure space-like separation the QRNG generates the random bit simultaneously with the entering of the photon into the interferometer. Then, the voltage applied to the EOM takes 40 ns to rise, which is shorter than the time of propagation inside the interferometer (about 160 ns). If the EOM was off, the two paths were distinguishable, since each detector is coupled to only one arm, and no interference was observed. Whereas, if the EOM was on the two paths cannot be distinguished, revealing the interference pattern.

3.4 PROPOSAL FOR A DELAYED-CHOICE EXPERIMENT ON A SPACE CHANNEL

From a practical point of view, the most challenging requirement of the Wheeler's gedankenexperiment is probably the realization of the free-choice. Indeed, one has to ensure that the choice of the measurement must be done after the choice of the photon to be either a classical particle or a wave. Even on a LEO satellite-to-ground link the round-trip-time of a photon is too short (about 10 ms) to find a simple mechanical device fast enough to switch from a measurement to the other.

From the various flavors of delayed choice experiments that have been done, we find convenient the use of an ancillary state associated to the photon to control the final measurement. The degree of freedom we choose are

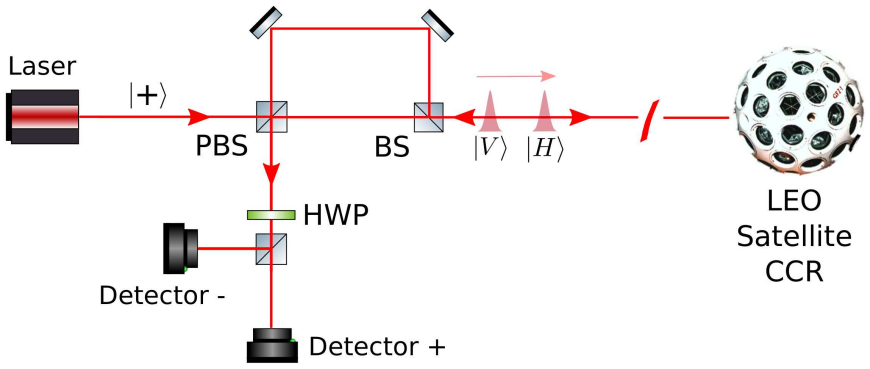

Figure 3.7: Interference of temporal modes controlled by polarization degrees of freedom.

the polarization and the time bin of the photon, which were already demonstrated to be preserved on a Space channel link by our group (Vallone et al., 2015, 2016). In our implementation, the property of being a particle or a wave is encoded in the time-bin degree of freedom, whereas we act on its polarization to switch the measurements.

3.4.1 *Revealing interference behavior*

Consider the setup shown in Fig. 3.7, in which diagonally polarized photon, $|+\rangle$, enters an unbalanced Mach-Zehnder interferometer, with the short (long) arm in the transmitted (reflected) line. The input port of the interferometer is a Polarized Beam Splitter (PBS) transmitting the horizontal polarization, $|H\rangle$, and reflecting the vertical one, $|V\rangle$. Then the two arms recombine on a BS that either transmits or reflects the photon. If we consider the output line towards the satellite, after the interferometer the state of the photon is

$$|\psi\rangle = \frac{1}{\sqrt{2}}(|H\rangle\,|s\rangle + |V\rangle\,|l\rangle), \tag{3.3}$$

being $|s\rangle$ and $|l\rangle$ the temporal modes of the photon. The above equation tells us that, in a quantum mechanical framework, the photon has traveled both the short and the long arm, moreover if we now measure the time of arrival of the photon we would see that if the photon arrives early (later) it would have an horizontal (vertical) polarization. Note that the above statement would have sense in a classical framework only if we assume the photon to behave like a wave. The photon then is reflected by the satellite, which introduces a phase ϕ between the temporal mode due to its radial velocity

$$|\psi\rangle = \frac{1}{\sqrt{2}}(|H\rangle\,|s\rangle - e^{i\phi}\,|V\rangle\,|l\rangle), \tag{3.4}$$

the minus sign appears because we are reflecting the direction of propagation of the photon, which is equivalent to a σ_z in the $|H\rangle$, $|V\rangle$ basis. In the way-back the photon re-enters into the interferometer. Considering the position

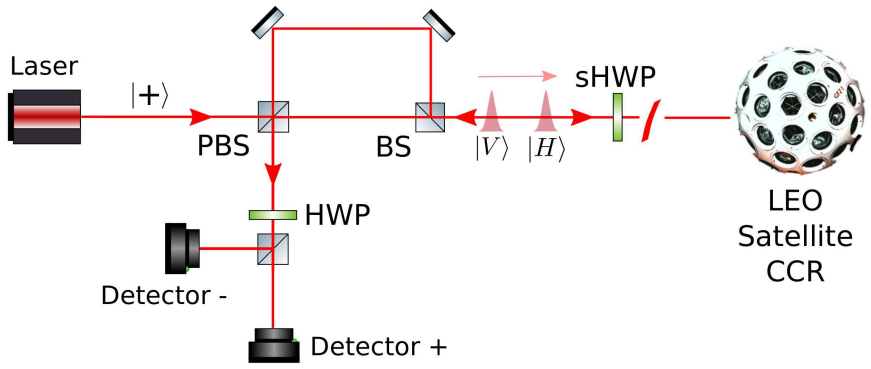

Figure 3.8: Which path controlled by polarization degrees of freedom.

of the detector, the photon will be measured only if the horizontal (vertical) component will go through the long (short) arm. Then, the state of the photon will become

$$|\psi\rangle = \frac{1}{\sqrt{2}}(|H\rangle\,|sl\rangle - e^{i\phi}\,|V\rangle\,|ls\rangle). \tag{3.5}$$

Since the temporal modes $|sl\rangle$ and $|ls\rangle$ are the same, the photon that, at the beginning, chose the short path is interfering with the one that chose the long arm. To calculate the probability of detection, we rewrite the state

$$|\psi\rangle = \frac{1}{\sqrt{2}}(|H\rangle - e^{i\phi}\,|V\rangle), \tag{3.6}$$

and then use the Born's rule

$$\begin{aligned} P_+ &= |\,\langle +,\psi\rangle\,|^2 = \frac{1}{2}(1-\cos\phi); \\ P_- &= |\,\langle -,\psi\rangle\,|^2 = \frac{1}{2}(1+\cos\phi). \end{aligned} \tag{3.7}$$

3.4.2 *Revealing which-path information*

Consider the setup shown in Fig. 3.8. As in the previous case the photon exits from the interferometer with state given in Eq. 3.3. However, this time the photon encounters a switchable HWP (sHWP) along the way towards the satellite. We assume the sHWP to be a device whose unitary matrix U_{sHWP} can be either an identity channel (deactivated), not perturbing the photon state, or a HWP with fast axis parallel to the diagonal polarization (activated), switching $|H\rangle$ to $|V\rangle$ and $|V\rangle$ to $|H\rangle$:

$$U_{\text{sHWP}} = \begin{bmatrix} 1 & 0 \\ 0 & 1 \end{bmatrix} \quad \text{or} \quad U_{\text{sHWP}} = \begin{bmatrix} 0 & 1 \\ 1 & 0 \end{bmatrix}. \tag{3.8}$$

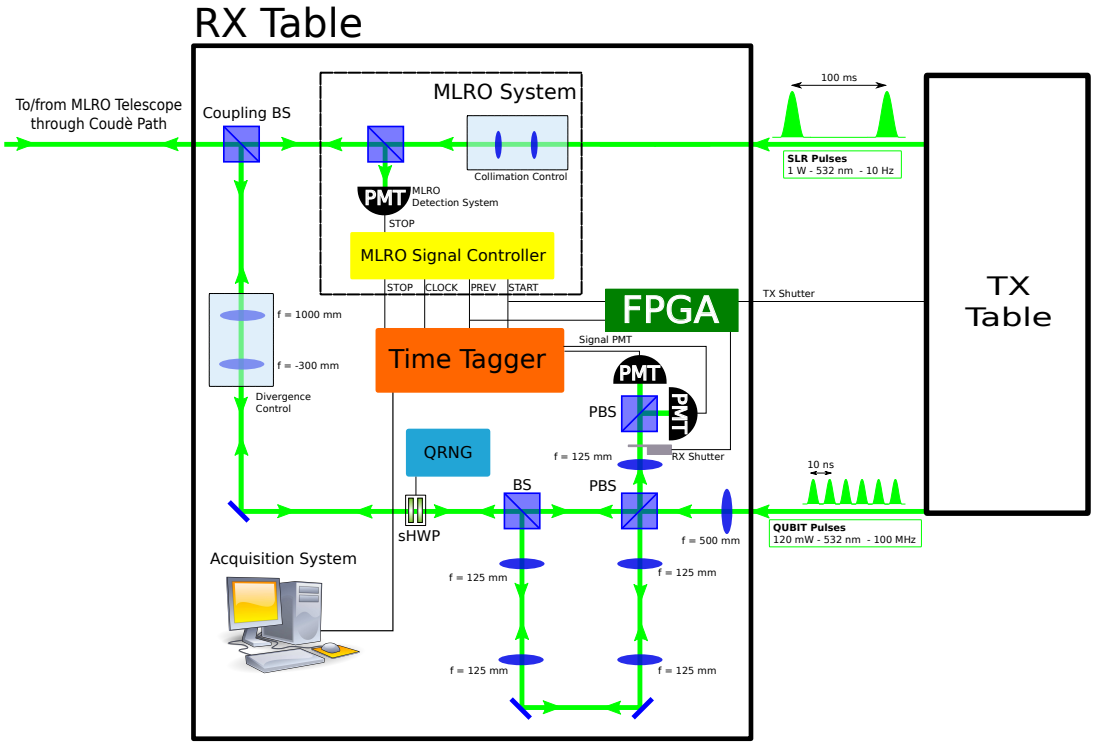

Figure 3.9: Receiving table implementing the Wheeler delayed-choice experiment.

In the up-going phase the sHWP is deactivated, preserving the photon state. Only in the way back from the satellite the sHWP is activated so that the state of the photon given in Eq. 3.4 becomes,

$$|\psi\rangle = \frac{1}{\sqrt{2}}(|V\rangle\,|s\rangle - e^{i\phi}\,|H\rangle\,|l\rangle). \tag{3.9}$$

Differently from the previous section, the photon will be measured only if the horizontal (vertical) component will go again through the short (long) arm of the interferometer. Hence, the state of the photon will be

$$|\psi\rangle = \frac{1}{\sqrt{2}}(|V\rangle\,|ss\rangle - e^{i\phi}\,|H\rangle\,|ll\rangle). \tag{3.10}$$

Then, the states $|ss\rangle$ and $|ll\rangle$ will be either detected by Det_+ or Det_-, and will be distinguishable by the time of arrival. If Δ is the temporal unbalance between the short and the long arms, then the difference in time of arrival of $|ss\rangle$ and $|ll\rangle$ will be 2Δ.

3.5 EXPERIMENT DESCRIPTION

3.5.1 *Setup*

The setup we implemented is similar to the one presented in Section 2.3. The transmission table is not changed with respect to the previous experiment

and is described in Fig. 2.10. The difference is in the state preparation and measurement on the quantum line, which is implemented in the receiving table. The new setup is depicted in Fig. 3.9. The state is prepared in the time-bin and polarization degrees of freedom by an unbalanced Mach-Zehnder interferometer composed by a PBS that splits two orthogonal polarization of the beam. Then, two mirrors are placed in the long arm to deviate the reflected beam towards a BS that merges them on the same optical path. The returning beam is coupled to the detectors through the output port of the PBS adjacent to the input port of the up-going beam. Finally, the beam goes through a series of QWP, HWP and PBS before being detected by two PMTs, placed at the transmitting and the reflecting ports of the PBS. The axes of the plates are rotated so that after the PBS the photon is projected on the two diagonal orthogonal states. In this way, each detector is coupled to the superposition of long and short paths, but with opposite phases.

In this case, the timing resolution on the arrival of the photon is fundamental to distinguish between the cases long-long, short-short, and long-short or short-long. For the best distinguishability we set the unbalance between the two arms to the maximum allowable by the repetition rate: the period between two consecutive photons is 10 ns that divided in three slots gives about 3.3 ns. Due to the jitter of the detectors and the TDC, we expect a statistical error of $\sigma = 200$ ps, which lets us to distinguish the three peaks with at least 10 σ separation.

In terms of length, the unbalance corresponds to about 1 m. Since we do not have a collimated beam inside the interferometer, such a long distance is sufficient to spoil the interferometer since the wavefront from the long arm will be much different from the one of the short arm. We decided to implement a double 4f-system in the long arm to match the two wavefronts. Fig. 3.10 illustrates the reshape of a gaussian beam passing through a single 4f-system. In this system two lenses, with equal focal length $f = 125$ mm, are placed so that their distance is two times f. The input plane at a focal length from the first lens is mapped into the output plane, preserving its dimension but rotating its image of 180 degrees. The latter effect is better explained by the ray tracing shown in Fig. 3.11. We consider two rays passing through a point in the input plane, one which is directed to the center of the first lens (ray A) and the other which is parallel to the optical axis of the system (ray B). Then, in the thin lens and paraxial approximation, A will not change its direction, while B will be redirected to the focal point of the lens. In the image plane of the first lens the rays are parallel with each other, hence they will meet on the focal plane after the second lens (the output plane). Ray B is also passing through the focal point of the second lens in the object plane, then it will be parallel to the optical axis after the second lens. From simple geometrical considerations the object point on the input plane and its image on the output plane are at the same distance from the optical axis, hence the

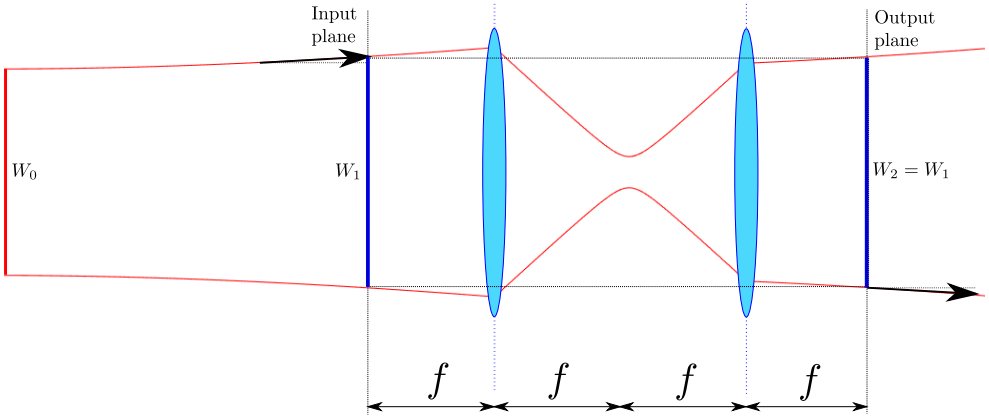

Figure 3.10: A gaussian beam passing through a 4f-system. The wavefront with width W_1 is mapped at four focal length distance on W_2, so that $W_2 = W_1$.

dimension are preserved. Moreover, there is a rotation along the optical axis of 180 degrees.

Hence, a 4f-system creates the reversed image of the BS on the subsequent mirror. Then, the beam propagates to the second mirror of the long arm, whose distance is equivalent to the short arm. Finally, the beam is imaged by the second 4f-system onto the PBS.

To reduce spherical aberration each lens is given by a doublet that comprises of a meniscus and a plano-convex lens each with $f = 250$ mm. Defocus aberration is controlled by moving a mirror on a micrometer sled. All the optics has a 2 inch diameter to avoid vignetting effect and an anti-reflection coating at wavelength 532 nm. The stability of the interferometer is reinforced by the cage system that rigidly holds the optics in place.

In this experiment, we aimed at the photons return from LEO satellites, with a round-trip-time shorter then 100 ms. The duty cycle is then different from what discussed in Section 2.3, being 100 ms instead of 200 ms. Here,

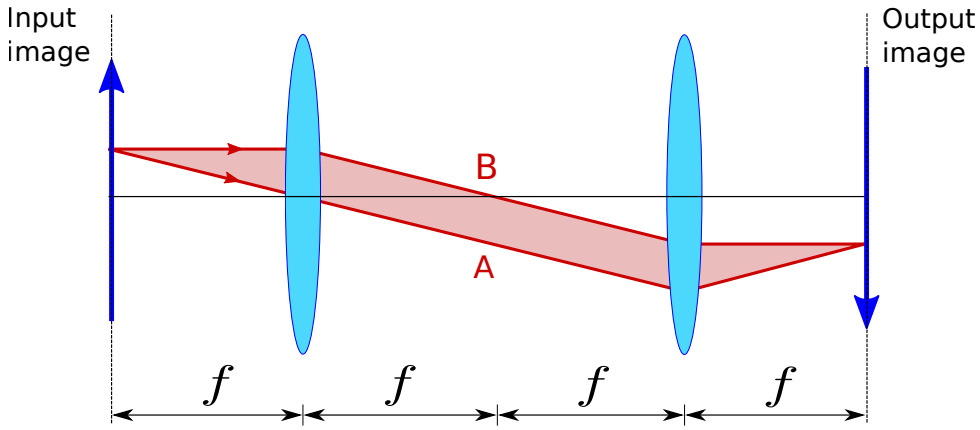

Figure 3.11: 4f-system with ray tracing

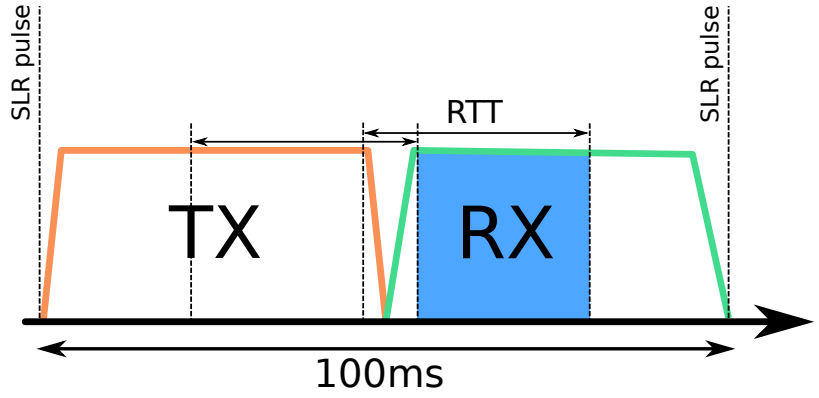

Figure 3.12: Scheme of the opening and closing time of the transmission (orange) and receiver (green) shutters.

the transmission shutter starts opening when the Start signal arrives at the FPGA and remains opened for the first half of the period. In the second half of the period, the transmission shutter is closed, whereas the receiver shutter is opened. The receiver shutter is then closed after another round-trip-time since no other photons are expected to arrive. The opening and closing times are schematized in Fig. 3.12. Because the shutters require a certain time to open and close completely, the effective detection time period is limited by the shutters transition time ($t_{\text{trans}} \sim 5$ ms), as sketched in the figure. On that basis, a precise temporal window $\tau = rtt - t_{\text{trans}}$ exists, where we expect to receive photons from the satellite.

The switchable HWP is implemented with two liquid crystal retarders mounted with the axes orthogonal to each other. Each liquid crystal introduces a phase between two linear orthogonal polarization states, defined by orienting their axes. By applying a voltage between 0 and 15 V the phase can be varied from $3\pi/4$ rad to almost 0 rad. The switching time we measured is about 500 μsec, much faster than what can be achieved by a mechanical switch.

The behavior of the liquid crystal is controlled by an on demand QRNG. The random bit is generated based on the differences of the times of arrival of the single photons in attenuated light (Stipčević and Rogina, 2007), if $b = 0$ the wave-like nature is revealed, otherwise if $b = 1$ the which-path information is measured. This protocol ensures the choice to be free and not predetermined, as would be the case for pseudo-random number generators. The random bit is extracted while the photons are propagating back to the ground station, so that these two events are space-like separated. To achieve this, we divided the receiving time into two windows each of half round-trip-time. Hence, every 100 ms we extract two random bits b_1 and b_2. The former is extracted during the shutter transition, whereas the latter is given at half round-trip-time (see Fig. 3.13). With this approach, each receiving window is characterized by two

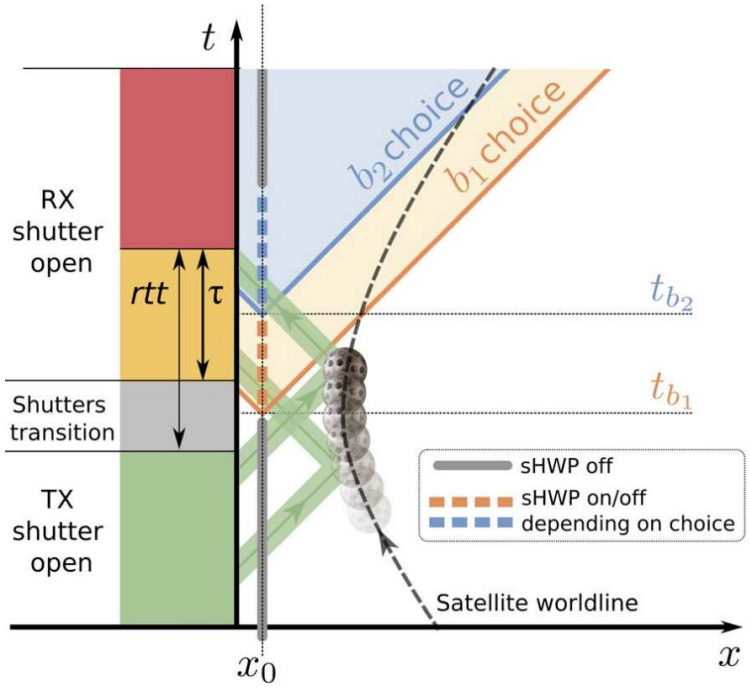

Figure 3.13: Minkowski diagram of the choice events with respect to photon propagation. Along the temporal axis (not to scale) a 100-ms cycle between two SLR pulses is represented. The x axis represents the radial coordinate (not to scale) from the detectors, where x 0 is the position of both the sHWP and the QRNG. The dotted line is the satellite worldline. We only considered the detections in the temporal window t. A fast FPGA controller synchronized in real time with the MLRO tracking system drives the two shutters and the QRNG. For each cycle, we performed two independent measurements via the random bit extracted by the QRNG at times t_{b_1} and t_{b_2}, causally disconnected from the photon reflection at the satellite. The cycle is repeated for each 100-MHz train between two SLR pulses.

independent choices in which the photons should have decided their nature at most at the reflection from the satellite.

3.5.1.1 *Alignment of the setup*

The alignment of the up-going beam is done using the same procedure described in Section 2.3, but with the long path of the interferometer blocked. Once this is done, we proceed by aligning the interferometer. First of all, the distances between the four lenses of the double 4f-system are optimized. For this optimization, we use as a figure of merit the image of the telescope aperture that forms after the interferometer (called pupil). Looking only at the short arm we place a CMOS camera on the plane of the pupil, in which the image of the spider that holds the secondary mirror of the telescope is formed. Then, we block the short arm, looking at the long path, and move the

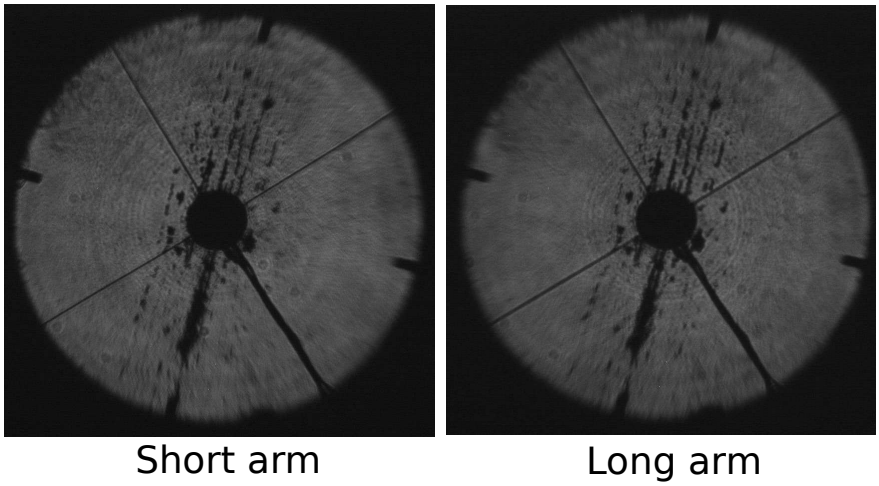

Figure 3.14: Images of the telescope aperture by pointing Vega.

lenses so that the image of the aperture is well formed on the camera and has the same dimension of the one that pass through the short arm (see Fig. 3.14). As a raw alignment of the interferometer mirrors, we unblock both arms and match the pupils from the long path over the pupil from the short arm. This procedure ensure a good match of the wavefront from the two arms.

The match of the spatial modes is performed by fine tip-tilting the interferometer mirrors and acting on the micrometer sled. In this case, we let the 100 MHz up-going pulses to go through the interferometer and be retroreflected by the CCR in front of the coudé path. We activate the liquid crystals to swap the polarization states to look at the interference pattern after the second pass through the interferometer. In the sub-optimal configuration the interference pattern shows several narrow fringes, as shown in Fig. 3.15. The type of pattern indicates the mismatch of the two beams and hence where to act as to have a single wide fringe. For instance, parallel fringes indicates a mismatch in the direction of propagation of the waves, while concentric fringes arises when the beams have different curvatures.

Finally, we couple the detectors to a bright star as discussed in Section 2.3, with the additional check of balancing the counts frequency of the long or short arms.

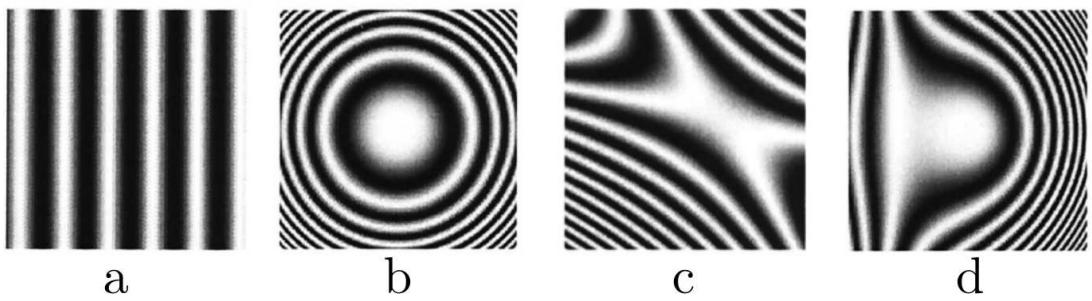

Figure 3.15: Typical interference patterns.

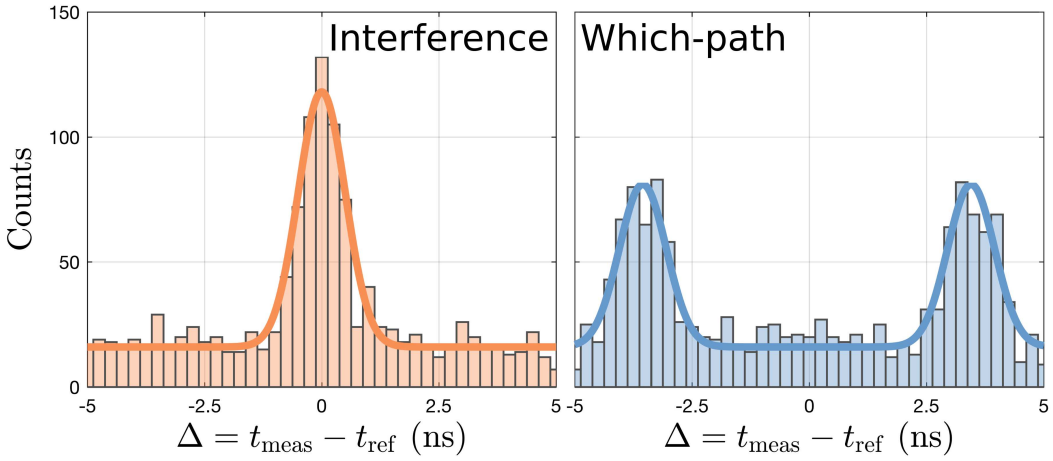

Figure 3.16: A sample of the extracted bits relative to 10 seconds of detections is shown. **Left**: temporal distribution of detections that refers to the group with $b = 0$. **Right**: temporal distribution of detections that refers to the group with $b = 1$. The counts in the central peak on the left histogram are comparable to the sum of the counts associated to the lateral peaks on the right one, as expected.

3.5.2 *Data analysis and results*

Here I will show the results obtained with the passages of two satellites: Beacon-C dated 1 November 2016 23:18 CEST (with a slant distance ranging from 1264 to 1376 km with respect to the MLRO) and Starlette dated 1 November 2016 22:00 CEST (with a slant distance ranging from 1454 to 1771 km). These two satellites are equipped with polarization preserving CCR array, which is necessary for our protocol.

As a first step we filter out the majority of the background by selecting only the times τ in which the receiving shutter is open. Then, we separate the remaining detection into two groups based on the value of the random bit b. For each group, we calculate the time difference Δ between the measured detection t_{meas} and the expected time of arrival t_{ref}. The result is shown in Fig. 3.16, for the detection on the anti-diagonal state (the other is analogous). The histogram on the **left** refers to the group with $b = 0$, in which the liquid crystals swap the polarization states of the returning photons so that the pulse that traveled the short arm has to pass through the long arm to hit the detector. Viceversa, the pulse that traveled the long arm has to pass through the short arm before being detected. In both cases the pulse takes the same round-trip-time to arrive at the detector as demonstrated by the single central peak in the figure. In this configuration, the information on which path the photon took is erased and the two modes are made to interfere. However, here we cannot calculate the visibility of the interference since we are not taking into account the kinematic phase introduced by the radial velocity of the satellite, but summing all the relative phases between the two modes. On

the **right** we show detection characterized by the choice of $b = 1$ in which the two modes are not made to interfere but we distinguish the path that the photon took. The peak centered at $\Delta = -3.5$ ns represents the detected pulses that took two times the short path, arriving before the expected time. On the contrary the peak at $\Delta = 3.5$ ns represents the detected pulses that both times took the long arm of the interferometer, arriving after the expected time. We note that the number of counts in the peak in the graph on the **left** is comparable to the sum of the two peaks in the graph on the **right**, which is what we expect since the QRNG has 50:50 chance to extract $b = 0$ or $b = 1$.

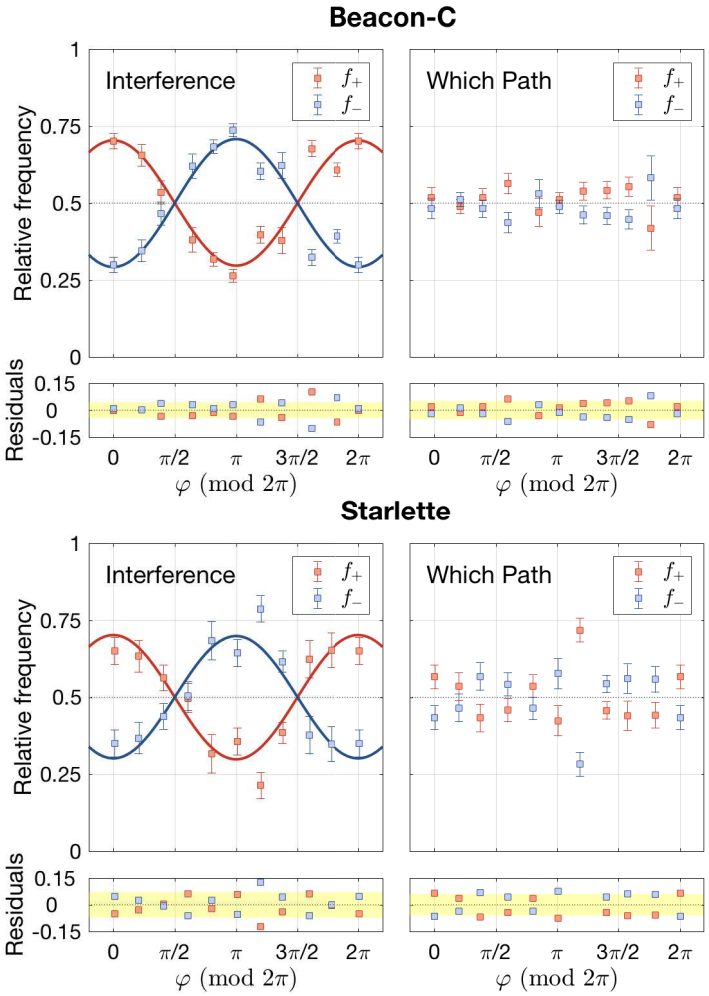

Figure 3.17: Experimental results for the interference and which-path configurations. Relative frequencies $f_\pm$ of counts in the two detectors $\text{Det}_\pm$ as a function of the kinematic phase ϕ introduced by the satellite for the passages of Beacon-C and Starlette satellites. The error bars are estimated using the Poissonian error associated to counts. Below each plot we show the relative residuals as a function of ϕ. We note that at the point $\phi \sim 0$ and $\phi \sim 2\pi$ the same subset of data was selected. In the "interference" configuration, we estimated from the fitted data a visibility $V_{\text{exp}} = 41 \pm 4\%$ for Beacon-C and $V_{\text{exp}} = 40 \pm 4\%$ for Starlette.

To reveal the wave-like nature of the photons we need to calculate the visibility of the interference. For this purpose we calculate the kinematic phase $\phi(t)(\mathrm{mod}\,2\pi)$, introduced by the satellite, associated to each detected pulse. Indeed, at a given instant t, the satellite motion determines a shift $R(t)$ of the reflector radial position, during the separation Δt between the two wave packets. This shift can be estimated at first order as $R(t) \simeq v_R(t)\Delta t$, being $v_R(t)$ the radial velocity of the satellite. From a special relativistic calculations it was found that the phase introduced by the satellite is given by (Vallone et al., 2016)

$$\phi(t) = \frac{2\beta(t)}{1+\beta(t)}\frac{2\pi c}{\lambda}\Delta t \simeq \frac{4\pi c}{\lambda}\Delta t, \tag{3.11}$$

with $\beta(t) = v_R(t)/c$. We further divided the detection depending on their phase into ten phase intervals $I_k = [(2k-1)\pi/10, (2k+1)\pi/10]$, with $k = 0, 1, \ldots, 9$. Then, for each phase interval we counted the detection $N_\pm$ from $\mathrm{Det}_\pm$. This is done by calculating the time difference Δ for each pulse, counting the events with $|\Delta| \leq 0.45$ ns and subtracting the background. The upper bound of 0.45 ns was chosen to optimize the trade-off between the signal-to-noise ratio and count rate. Then we calculate the relative detection frequency $f_\pm = \eta_\mp N_\pm(\eta_- N_+ + \eta_+ N_-)$, with $\eta_+ = 0.12$ and $\eta_- = 0.10$ the different quantum efficiency of the detectors. On the **left** panels of Figs. 3.17, we show the results for the subset of data with $b = 0$, where the photon's "which-path" information has been erased. The plot exhibits the typical behavior of two interfering waves, with a clear phase-modulation of the detector count frequency. By fitting the relative frequency with the equation

$$P_\pm = \frac{1}{2}(1 + V_{\mathrm{exp}}\cos(\phi)) \tag{3.12}$$

we find the experimental visibility $V_{\mathrm{exp}} \simeq 40\%$ for both satellites. Due to experimental imperfection on the alignment of the interferometer and on the residual birefringence caused by the coudé path mirrors, the experimental visibility is lower than the theoretical value of 100%.

On the **right** panels, the relative frequencies are constant, within the statistical fluctuations, for all values of the kinematic phase, as predicted by the theoretical model $P_\pm = 1/2$.

We can estimate the percentage of photons that acted as a particle when the "which-path" information was inquired as the sum of the lateral peaks over all the counts (subtracting the background). What we found is that the $88 \pm 1\%$ ($86 \pm 1\%$) acted as expected for the Beacon-C (Starlette) passage. Indeed, when a photon arrives at $\Delta = -3.5$ ns or $\Delta = 3.5$ ns the path of the photon is known, whereas if the photon arrives at $\Delta = 0$ ns it is hiding the path it took when this information was inquired. We may interpret this fact as if the photons were making the choice on their own nature before entering the interferometer, being 87% of the time classical particles and, hence, 13% of

the time classical waves. However, we have observed that when the wave-like nature of the photons is measured, 40% of the time the photons are found to be in that state, in contrast with the 13% derived by the previous assumption. Hence, we have to rule out the hypothesis that the photon is either a particle or a wave, in favor of a quantum interpretation of the light in which the photon is in a superposition of the two "classical" states (particle or wave) and only at the moment of the measurement its state becomes either of the two.

However, we note that to rule out semiclassical theories in which the classical electromagnetic field interacts with quantized matter at the detection, true single photons should be used instead of coherent attenuated light (Ma, Kofler, and Zeilinger, 2016).

We assessed the agreement between the theoretical model and the experimental results calculating the residuals between the fit and the data. As shown in Fig. 3.17, these are randomly distributed and most of them lay within 1.5 times the statistical error.

From what concerns the received mean number of photons, as discussed in Chapter 2 we can calculate it from the mean detection frequency and the channel losses. We found a mean number of photons at the primary mirror of the telescope of $\mu \sim 2.2 \times 10^{-3}$ for Starlette and $\mu \sim 1.9 \times 10^{-3}$ for Beacon-C. We can conclude that the particle- and wave-like properties of light are measured at the single photon level, since the probability of having more than one photon entering the interferometer on the way back is $\mu^2/2 \sim 10^{-6}$.

3.6 DISCUSSION

We realized Wheeler's delayed-choice gedankenexperiment along a space channel involving LEO satellites by combining two independent degrees of freedom of light. The experimental arrangement that allows the measurement of the complimentary wave or particle behaviors of light quanta was randomly set according to two alternative configurations while the photons were already inside the apparatus, as required in the delayed-choice paradigm. To measure interference with the first configuration, it is crucial to take into account the kinematic phase shift introduced by the satellite motion. By observing single-photon interference after the propagation along a 3500-km space channel, we can confute with clear statistical evidence of 5 sigmas the description of light quanta as classical particles. In the alternative configuration of the detection scheme, the phase-dependent modulation in the received clicks disappears, and the which-path information can be clearly reconstructed.

The high losses in the two-way propagation between the ground station and the satellite hampers the implementation of this scheme for the delayed-choice experiments using true single-photon sources or entangled particles, such as delayed-choice quantum erasure and entanglement swapping (Żukowski et al., 1993). These experiments, already demonstrated on the ground (Kaiser

et al., 2012; Ma, Kofler, and Zeilinger, 2016; Ma et al., 2012), require an active source on a satellite for the implementation in the space scenario. Our results extend the validity of the quantum mechanical description of complementarity to the spatial scale of LEO orbits. Furthermore, they support the feasibility of efficient encoding by exploiting both polarization and time bin for high-dimensional free-space quantum key distribution (Zhong et al., 2015) over long distances. Finally, our work paves the way for satellite implementation of other foundational-like tests and applications of quantum mechanics involving hyper-entangled states (Barbieri et al., 2006; Cabello, 2006; Graham et al., 2015; Steinlechner et al., 2017), around the planet and beyond.

We often discussed his notion on objective reality.
I recall that during one walk Einstein suddenly stopped,
turned to me and asked whether I really believed that
the moon exists only when I look at it.

— Abraham Pais (Pais, 1979)

4

THREE-OBSERVER BELL INEQUALITY VIOLATION ON A TWO-QUBIT ENTANGLED STATE

Bell's 1964 theorem has deeply influenced our perception and understanding of physics, and it arguably ranks among the most profound scientific discoveries ever made. With a simple argument it shows how predictions of quantum theory cannot be accounted for by any local theory, on which the physicist's intuition of how the world works was based. In the last two decades, with the advent of quantum information science, considerable interest has been devoted to Bell's theorem; the main motivation were the new resources provided by the nonlocality of quantum theory, underpinning many of the advantages afforded by a quantum processing of information.

This Chapter is devoted to the description of our work on the Bell inequality violation, in the unprecedent scenario with three observers sharing a two-qubit entangled state. I will start with an introduction to the EPR paradox that led Bell to formulate his theorem, followed by his definition of locality. Afterwards, I will go through the theoretical model, the design and results of our experiment.

4.1 EPR PARADOX AND BELL INEQUALITY

As we have discussed in Chapter 3, the measurements of physical properties do not simply reveal pre-existing or pre-determined values. The particular outcome of the measurement somehow "emerges" from the dynamical interaction of the system being measured with the measuring device. This is highlighted by the wave-particle duality, but we may devise other scenarios in which this counter-intuitive property arise. For instance, think about the possible measurements on the polarization of a single photon. Assume to have a photon prepared in a vertical polarization state and to measure

whether it is in a diagonal or anti-diagonal state. The output of the measurement will be the same photon now in either the diagonal or anti-diagonal polarization, with 50-50% outcome probability. Assume that, in a single run of the experiment, the photon is measured in the diagonal state. If another subsequent measurement is performed in the vertical and horizontal basis, the output state will be either vertical or horizontal, again with 50-50 probability. Therefore, the measurement is not revealing the state of the photon but it is determining the new state that "emerges" from the observation. According to QM, the knowledge on the particle's state before the measurement let us predict which is the probability of the outcomes after the measurement. While the actual values of the physical properties arise as a consequence of measurements performed upon the system. On the contrary, from a classical point of view, when we speak of an object such as a person or a tennis ball, we assume that the physical properties of that object have an existence independent of observation. Therefore, measurements merely act to reveal such physical properties (this is known as *realism* assumption).

In 1935, Albert Einstein, Boris Podolsky, and Nathan Rosen demonstrated that QM does not allow the existence of pre-determined values for any physical reality or, using their terminology, QM is not a complete theory (Einstein, Podolsky, and Rosen, 1935). In their definition:

> the following requirements for a complete theory seems to be a necessary one: every element of the physical reality must have a counter part in the physical theory. We shall call this the condition of completeness. [...] If, without in any way disturbing a system, we can predict with certainty (i.e., with probability equal to unity) the value of a physical quantity, then there exists an element of physical reality corresponding to this physical quantity.

Hence, a pre-determine value is given by the quantum state if the value of the physical reality (physical quantity) can be predicted with certainty before the actual measurement takes place. Considering for instance the polarization of the photon as a physical reality, as we said above, the horizontal/vertical and diagonal/anti-diagonal polarization cannot be pre-determined simultaneously (Bohm and Aharonov, 1957). In general, it can be demonstrated that any couple of non-commuting operators, corresponding to two different measurements on the system, do not admit the simultaneous knowledge of the two associated physical quantities.

> From this follows that either (1) the quantum mechanical description of reality given by the wave function is not complete or (2) when the operators corresponding to two physical quantities do not commute the two quantities cannot have simultaneous reality.

Consider now the presence of two photons whose initial state is known. For our purpose, the two photons are in a polarization entangled state

$$|\Psi^-\rangle = \frac{1}{\sqrt{2}}(|H_1V_2\rangle - |V_1H_2\rangle). \tag{4.1}$$

The photons are then allowed to travel far apart so that a measurement on the first photon would not immediately disturb the second photon. This state establish a perfect anti-correlation: if the photon 1 is in $|H_1\rangle$ state then photon 2 is in $|V_2\rangle$ state, and vice versa. Hence, after the measurement of photon 1, the second photon state is known with certainty without disturbing it. However, it is easy to show that the same state can be written as

$$|\Psi^-\rangle = \frac{1}{\sqrt{2}}(|D_1A_2\rangle - |A_1D_2\rangle), \tag{4.2}$$

where, if the photon 1 is found in $|D_1\rangle$ state then photon 2 will be in $|A_2\rangle$ state, and vice versa. Hence, after the measurement of photon 1, the second photon state is again known with certainty. As EPR noted, we can state the following:

> by measuring [on the first photon] either A [horizontal/vertical polarization] or B [diagonal/anti-diagonal polarization] we are in a position to predict with certainty, and without in any way disturbing the second system, either the value of the quantity [horizontal or vertical polarization] or the value of the quantity [diagonal or anti-diagonal polarization].

Hence, they conclude the argument:

> Starting then with the assumption that the wave function does give a complete description of the physical reality, we arrived at the conclusion that two physical quantities, with non-commuting operators, can have simultaneous reality. Thus the negation of (1) leads to the negation of the only other alternative (2). We are thus forced to conclude that the quantum-mechanical description of physical reality given by wave functions is not complete.

EPR was the first to recognize that the classical concept of realism could not hold in QM along with the assumption of locality (i.e. the fact that causal influences propagate at a maximum finite velocity).

Nearly thirty years after the EPR paper was published, an experimental test was proposed by Bell that could be used to check whether or not Nature is non local realism (Bell, 1964). In a typical Bell experiment we have a source of couples of particles and two distant observers, usually called Alice and Bob. In each run of the experiment, a couple of particles is distributed to the observers on which they perform two independent measurements. In

particular, each observer has two different apparatuses measuring the physical properties of the particle, say P_Q and P_R for Alice and P_S and P_T for Bob. For simplicity, assume that the measurements can have only two possible outcomes: $+1$ and -1. Moreover, Alice and Bob do not know in advance which measurement they are going to perform before the arrival of the particle, instead they wait for the arrival of the particle and then choose it randomly. Also the timing of the measurements is such that the corresponding events are space-like separated. Therefore, the measurement performed by Alice cannot disturb the result of Bob's measurement (or vice versa) since physical influences cannot propagate faster than light. Then consider the quantity

$$QS + RS + RT - QT = (Q + R)S + (R - Q)T. \tag{4.3}$$

Since Q, $R = \pm 1$, it follows that either $Q + R = 0$ (and $R - Q = \pm 2$) or $R - Q = 0$ (and $Q + R = \pm 2$), hence $QS + RS + RT - QT = \pm 2$. Suppose next that, before the measurement the system is in the state where $Q = q$, $R = r$, $S = s$ and $T = t$ with probability $p(q, r, s, t)$. Then the mean value will be

$$\begin{aligned} E(QS + RS + RT - QT) &= \sum_{qrst} p(q, r, s, t)(qs + rs + rt - qt) \\ &\leq \sum_{qrst} p(q, r, s, t)2 \\ &= 2. \end{aligned} \tag{4.4}$$

On the other side

$$E(QS + RS + RT - QT) = E(QS) + E(RS) + E(RT) - E(QT). \tag{4.5}$$

Finally we arrive at the following Bell inequality, better known as the Clauser, Horne, Shimony, and Holt (CHSH) inequality

$$E(QS) + E(RS) + E(RT) - E(QT) \leq 2. \tag{4.6}$$

This result is part of a larger set of inequalities known generically as Bell inequalities and it has been derived using some simple algebra and making the following assumptions:

- **Realism**. Before the measurements, the physical properties of the particles have defined values $Q = q$, $R = r$, $S = s$ and $T = t$ which are simply revealed by the observers.
- **Locality**. Alice and Bob's measurements do not disturb each other. Hence, in every run of the experiment, Bob's outcome does not depends on Alice's one and vice versa.

After repeating the experiment many times, Alice and Bob compare their results and calculate the left hand side of Eq. 4.6. We can predict what would

be the results using the QM framework. Assume the particles' state to be the singlet state

$$|\Psi^-\rangle = \frac{1}{\sqrt{2}}(|01\rangle - |10\rangle). \tag{4.7}$$

On their respective particle, Alice performs the measurements $Q = \sigma_z$ or $R = \sigma_x$ (with $\sigma_z = |0\rangle\langle 0| - |1\rangle\langle 1|$ and $\sigma_x = |0\rangle\langle 1| + |0\rangle\langle 1|$), whereas Bob chooses between

$$S = -\frac{1}{\sqrt{2}}(\sigma_z + \sigma_x) \quad \text{or} \quad T = \frac{1}{\sqrt{2}}(\sigma_z - \sigma_x). \tag{4.8}$$

Using the Born's rule we have that, for instance $E(QS) = \langle\Psi^-| QS |\Psi^-\rangle$. After simple calculations we obtain

$$E(QS) = E(RS) = E(RT) = -E(QT) = \frac{1}{\sqrt{2}}, \tag{4.9}$$

and hence

$$E(QS) + E(RS) + E(RT) - E(QT) = 2\sqrt{2} \geq 2, \tag{4.10}$$

which is violating the CHSH inequality that we stated in Eq. 4.6. Note that the entanglement is necessary to violate the inequality but still is not sufficient since the set of measurements chosen by Alice and Bob cannot be arbitrary. This result tells us that one or both of the assumptions we used to derive the Bell inequality cannot apply to QM.

4.2 LOCALITY AND LOCAL HIDDEN VARIABLE THEORIES

We may give a formal definition of locality (Brunner et al., 2014). We reformulate the Bell experiment: a and b represent the outcomes of Alice and Bob's measurement, respectively. The choice of the measurement is labeled respectively by x and y. In a run of the experiment, in general we may find that the outcome conditioned probabilities are correlated:

$$p(ab|xy) \neq p(a|x)p(b|y) \tag{4.11}$$

even if the two observers are far apart and the events, corresponding to the measurement, are space-like separated. This correlation is nothing mysterious, since it could be explained by a past interaction between the particles in which the correlation was established. As a simple example, assume that Alice and Bob measure either the color or the suit of a card, which is given to them by a third party, say Charlie. The color of the cards may be red (R) or blue (B) and the suit may be diamond (♢) or clubs (♣). Charlie may prepare couples of cards to give to the observers whose colors and suits are

Color 1	Suit 1	Color 2	Suit 2	λ
R	♢	B	♣	1
B	♢	R	♣	2
R	♣	B	♢	3
B	♣	R	♢	4

Table 4.1: Possible combinations of cards preparation.

anti-correlated. There are four possible combinations in which he can prepare the cards (see Tab. 4.1). Clearly, for Alice and also for Bob it holds that $p(\mathrm{R}|\mathrm{Color}) = p(\mathrm{B}|\mathrm{Color}) = 1/2$ and $p(♢|\mathrm{Suit}) = p(♣|\mathrm{Suit}) = 1/2$. However, we will have that for instance $p(\mathrm{R},\mathrm{B}|\mathrm{Color},\mathrm{Color}) = 1/2$. Still, this experiment will not violate the Bell inequality since $E(\mathrm{Color},\mathrm{Color}) = E(\mathrm{Suit},\mathrm{Suit}) = -1$ and $E(\mathrm{Color},\mathrm{Suit}) = E(\mathrm{Suit},\mathrm{Color}) = 0$. In this example, the correlation is established before the measurement by Charlie with the value of the physical properties (Color and Suit) predetermined and simply revealed by Alice and Bob.

In a locally realistic interpretation of the experiment, the above example may be generalized by introducing a variable λ, taking some predefined values before the measurement. This variable may even be impossible to measure, being hidden from the observer investigation. This is the characterizing property of the so called local hidden variable theories. The hidden variable must identify all the past factors having a joint casual influence on both outcomes, so that the probability for a and b should factorize

$$p(ab|xy,\lambda) = p(a|x,\lambda)p(b|y,\lambda). \tag{4.12}$$

As regard the previous example, the above equation now holds including the value of λ given in Tab. 4.1. This factorability condition simply expresses the fact that we have found an explanation according to which the probability for a depends only on the past variables λ and on the local measurement x, but not on the distant measurement and outcome, and analogously for the probability to obtain b. We may also allow λ to change its values during the experiment in a non-deterministic way. Therefore, we assign a probability $q(\lambda)$ to the particular realization of λ. The final definition of locality is

$$p(ab|xy) = \int_\Lambda \mathrm{d}\lambda\, q(\lambda)p(a|x,\lambda)p(b|y,\lambda), \quad \text{with} \quad p(\lambda|xy) = p(\lambda). \tag{4.13}$$

The right hand equation states that the measurements x and y can be freely chosen in a way that is independent from λ. Note that no assumptions of determinism are being involved in Eq. 4.13: we assumed that a (and similarly b) is only probabilistically determined by the measurement x and the variable λ, with no restrictions on the physical laws governing this causal relation.

From Eq. 4.13, we may derive the CHSH inequality. Consider an experiment in which the observers chooses between two measurements ($x, y \in \{0, 1\}$). Moreover, we limit to two the possible number of outcomes ($x, y \in \{+1, -1\}$). The expectation value of the product ab, given the choice of measurement (x, y), is defined by

$$\langle a_x b_y \rangle = \sum_{ab=\pm 1} abp(ab|xy). \tag{4.14}$$

Considering the quantity $I = \langle a_0 b_0 \rangle + \langle a_1 b_0 \rangle + \langle a_0 b_1 \rangle - \langle a_1 b_1 \rangle$ and using Eq. 4.13 we find (Clauser et al., 1969)

$$I = \langle a_0 b_0 \rangle + \langle a_1 b_0 \rangle + \langle a_0 b_1 \rangle - \langle a_1 b_1 \rangle \leq 2. \tag{4.15}$$

As we have seen in the previous section, this inequality is predicted to be violated by quantum mechanics.

These two assumptions together are known as the assumptions of local realism. They are certainly intuitively plausible assumptions about how the world works, and they fit our everyday experience. Yet Bell inequalities show that at least one of these assumptions is not correct. For physicists, the most important lesson is that their deeply held commonsense intuitions about how the world works are wrong. The first experimental confirmation of the violation of these inequalities were performed by Freedman and Clauser, 1972 and many others. Nonetheless, the previous realizations were affected by the limited performances of their devices, allowing for local hidden variable theory not to be ruled out (Larsson, 2014). Very recently, the works by Giustina et al., 2015; Hensen et al., 2015; Shalm et al., 2015 finally proved the violation of a Bell inequality even in the most paranoid scenario, confirming that the world is not locally realistic.

The crucial ingredient for the violation of a Bell inequality is the use of entanglement. Indeed, no separable states can violate a Bell inequality. Therefore, entanglement is a fundamental non-classical resource that goes beyond what could be achieved by classical means. Having realized this, a new field merging Quantum Mechanics and Information Theory was put forward (quantum computation and quantum information), whose major task is to exploit this new resource to do information processing tasks that were impossible or much more difficult to do with classical resources.

4.3 THREE-OBSERVER VIOLATION

An intriguing property of quantum entanglement is monogamy (Coffman, Kundu, and Wootters, 2000): given a tripartite state $\rho_{AB_1B_2}$, the larger is the entanglement between two observers, the lower is the entanglement of the third observer with any of the other two. A similar monogamy argument holds for "non-local-realistic" correlations (Masanes, Acin, and Gisin, 2006;

Toner, 2009), whose presence is associated with the violation of Bell inequalities. Indeed, given three observers (Alice, Bob1 and Bob2) and assuming non signaling, it is impossible to have a simultaneous violation between Alice-Bob1 and Alice-Bob2.

However, as realized by Silva et al., 2015, this restriction no longer holds if the non-signaling hypothesis is dropped. In this scenario, it is possible to violate the CHSH inequality between two different pairs of observers by using a single two-qubit entangled state and allowing the state received by Bob2 to be first measured by Bob1. In this case, the state received by Bob2 is dependent on Bob1's basis choice and therefore there is signaling between Bob1 and Bob2. However, the two Bobs do not have to agree on a common measurement strategy and can in principle be unaware of each other's presence, so they may be considered as independent. This no longer holds for more than two observers on the Bob's side: they would have to agree on a measurement strategy, that is, they cannot perform unbiased measurements in order to violate all together the CHSH inequality with Alice (Mal, Majumdar, and Home, 2016). In this section, I will describe the measurement performed by Bob1 and demonstrate the simultaneous violation of the two Bell inequalities, in the QM framework.

4.3.1 *Bob1's weak measurement*

To violate a Bell inequality between Alice and Bob2, Bob1 should not perform a *strong* measurement, since it would destroy the entanglement. Instead a weak measurement on the photon polarization, that extracts partial information on the state, is required. In Fig. 4.1, we show a circuital representation of Bob1's measurement. The weak measurement can be divided into a pre-measurement, in which the system state interacts with the meter (or ancilla), and a (strong) measurement on the meter, in which the actual information is extracted. The control phase gate of parameter ϵ is equivalent to a pre-measurement of the photon polarization, distinguishing between states $|H\rangle$ and $|V\rangle$. The unitary evolution of such gate, U_ϵ, can be written as

$$U_\epsilon = |H\rangle\langle H|_p \otimes \mathcal{I}_m + |V\rangle\langle V|_p \otimes \left(e^{i\epsilon\sigma_z}\right)_m . \tag{4.16}$$

The meter is prepared in the initial state $|+\rangle_m = \frac{1}{\sqrt{2}}(|0\rangle_m + |1\rangle_m)$, so that the evolved state is a linear combination of the following

$$U_\epsilon |H\rangle_p |+\rangle_m = |H\rangle_p |\phi_H\rangle_m = |H\rangle_p |+\rangle_m , \tag{4.17}$$

$$U_\epsilon |V\rangle_p |+\rangle_m = |V\rangle_p |\phi_V\rangle_m = |V\rangle_p (\cos\epsilon |+\rangle_m + i \sin\epsilon |-\rangle_m) . \tag{4.18}$$

The pre-measurement correlates the photon states $|H\rangle_p$ and $|V\rangle_p$ with the meter states $|\phi_H\rangle_m$ and $|\phi_V\rangle_m$ respectively. Consequently, the pre-measurement is a photon state measurement on the basis $(|H\rangle_p, |V\rangle_p)$. To perform a Bell

test, Bob1 needs to measure on two different bases. This is achieved by setting a rotation on the photon state, with R_p and $R_p^\dagger$. Indeed, consider R_p such that

$$R_p \left|\omega_{b1}\right\rangle_p = \left|H\right\rangle_p,$$
$$R_p \left|\omega_{b1}^\perp\right\rangle_p = \left|V\right\rangle_p.$$

As a consequence, the pre-measurement $R_p^\dagger U_\epsilon R_p$ evolves the states so that

$$R_p^\dagger U_\epsilon R_p \left|\omega_{b1}\right\rangle_p \left|+\right\rangle_m = \left|\omega_{b1}\right\rangle_p \left|\phi_H\right\rangle_m, \tag{4.19}$$
$$R_p^\dagger U_\epsilon R_p \left|\omega_{b1}^\perp\right\rangle_p \left|+\right\rangle_m = \left|\omega_{b1}^\perp\right\rangle_p \left|\phi_V\right\rangle_m. \tag{4.20}$$

In this way, the pre-measurement is performed on the basis $(\left|\omega_{b1}\right\rangle_p, \left|\omega_{b1}^\perp\right\rangle_p)$, that can be arbitrarily chosen by simply changing the rotation.

A measurement on the meter tries to distiguish the states $\left|\phi_H\right\rangle_m$ and $\left|\phi_V\right\rangle_m$. The distinguishability of $\left|\phi_H\right\rangle_m$ and $\left|\phi_V\right\rangle_m$, hence the strength of the measurement, is controlled by the phase parameter ϵ. Indeed, their overlap only depends on ϵ:

$$F = \left\langle\phi_H|\phi_V\right\rangle_m = \cos\epsilon. \tag{4.21}$$

The interesting cases are the ones in which ϵ goes from 0 to $\pi/2$. The strong measurement limit is given by $\epsilon = \pi/2$. In this case, $\left|\phi_H\right\rangle_m$ is orthogonal to $\left|\phi_V\right\rangle_m$, hence a projective measurement on the meter would distinguish $\left|\phi_H\right\rangle_m$ from $\left|\phi_V\right\rangle_m$. That would be equivalent to a projective (strong) measurement on the polarization of the photon. On the opposite side, when $\epsilon = 0$ the measurement is not taking place. Indeed, the meter does not interact with the photon and $\left|\phi_H\right\rangle_m = \left|\phi_V\right\rangle_m = \left|+\right\rangle_m$. Hence, any information on the meter state would be independent from the state of the photon.

The outcomes of Bob1's measurement are given by a projection on two orthogonal states, $\left|\phi_+\right\rangle_m$ and $\left|\phi_-\right\rangle_m$, of the meter. Corresponding to the projections onto $\left|\phi_+\right\rangle_m$ and $\left|\phi_-\right\rangle_m$, the outcomes of Bob1 measurements are respectively $b_1 = +$ and $b_1 = -$. The precision of the weak measurement G is given by the choice of these states so that

$$G = 1 - \left|\left\langle\phi_H|\phi_-\right\rangle\right|^2 - \left|\left\langle\phi_V|\phi_+\right\rangle\right|^2 \tag{4.22}$$

Since we want to distinguish $\left|\phi_H\right\rangle_m = \frac{1}{\sqrt{2}}(\left|0\right\rangle_m + \left|1\right\rangle_m)$ and $\left|\phi_V\right\rangle_m = \frac{1}{\sqrt{2}}(\left|0\right\rangle_m + e^{i2\epsilon}\left|1\right\rangle_m)$, we choose a family of two orthogonal states, parametrized by the real variable ϕ:

$$\left|\phi_+\right\rangle_m = \frac{1}{\sqrt{2}}(\left|0\right\rangle_m + e^{i\phi}\left|1\right\rangle_m), \tag{4.23}$$
$$\left|\phi_-\right\rangle_m = \frac{1}{\sqrt{2}}(\left|0\right\rangle_m - e^{i\phi}\left|1\right\rangle_m). \tag{4.24}$$

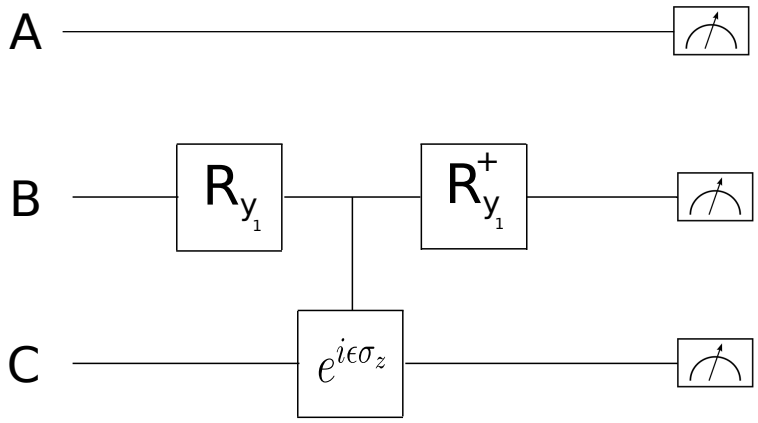

Figure 4.1: Logical circuit representing the unitary evolution U_{y_1}.

It follows that $G = \frac{1}{2}(\cos(\phi) - \cos(\phi + 2\epsilon))$. The extremes of G for ϕ gives $\epsilon = 0$, that corresponds to $G = 0$ and no interaction, or $\phi = \pi/2 - \epsilon$ for which $G = \sin\epsilon$. The last condition corresponds to the optimal weak measurement since $G^2 + F^2 = 1$ (Silva et al., 2015). In our experiment we choose to measure in the basis $|\phi_+\rangle_m = |+\rangle_m$ and $|\phi_-\rangle_m = |-\rangle_m$ which correspond to $G = \sin^2\epsilon$.

4.3.2 *Outline of the theoretical demonstrations*

The experiment can be represented by the logical circuit in Fig. 4.1. On the left, a tripartite state, $\rho_{ABC} \in H_A \bigotimes H_B \bigotimes H_C$, is prepared such that its density matrix is given by $\rho_{ABC} = \rho_{AB} \bigotimes |+\rangle\langle+|_C$, where ρ_{AB} is the singlet state and $|+\rangle = \frac{1}{\sqrt{2}}(|0\rangle + |1\rangle)$. The state is evolved by the unitary map U_{y_1} into

$$\rho'_{ABC} = U_{y_1}\rho_{ABC}U^\dagger_{y_1}, \tag{4.25}$$

which is then measured by the three observers Alice, Bob2 and Bob1, each one with access to the respective Hilbert spaces H_A, H_B and H_C. These are dichotomic measurements whose outcome we label as $a = \pm 1$, $b_2 = \pm 1$ and $b_1 = \pm 1$, respectively. The evolution depends on a random variable $y_1 = 0, 1$ with probability $P(y_1)$, that changes the transformation R_{y_1} such that

$$R^\dagger_{y_1}|0\rangle = |w_{y_1}\rangle, \tag{4.26}$$

$$R^\dagger_{y_1}|1\rangle = |w^\perp_{y_1}\rangle. \tag{4.27}$$

The evolution is the combination of a phase gate and two rotation that can be written as

$$U_{y_1} = R^\dagger_{y_1 B}\left(|0\rangle\langle 0|_B + |1\rangle\langle 1|_B (e^{i\epsilon\sigma_z})_C\right) R_{y_1 B} \tag{4.28}$$

$$= \pi_B^{+y_1} + \pi_B^{-y_1}(e^{i\epsilon\sigma_z})_C \tag{4.29}$$

where $\pi_B^{+y_1} = |w_{y_1}\rangle\langle w_{y_1}|_B$ and $\pi_B^{-y_1} = |w^\perp_{y_1}\rangle\langle w^\perp_{y_1}|_B$. Note that the evolution is not deterministic, as the operator U_{y_1} depends on a random variable y_1. Alice, Bob1 and Bob2's measurement apparatuses are projective measurements

$A_a^x = |u_a^x\rangle\langle u_a^x|_A$, $B_{b_1}^{y_1} = |b_1\rangle\langle b_1|_C$ and $B_{b_2}^{y_2} = |w_{b_2}^{y_2}\rangle\langle w_{b_2}^{y_2}|_B$, so Bob1 is the one that chooses the transformation R_{y_1} (but not which one of the two to use). From the final state ρ'_{ABC}, we can calculate the probabilities needed for the CHSH inequalities:

$$P(ab_1|xy_1) = \mathrm{Tr}(A_a^x B_{b_1}^{y_1} \rho'_{AC}), \qquad \rho'_{AC} = \mathrm{Tr}_B(\rho'_{ABC}), \tag{4.30}$$

$$P(ab_2|xy_2) = \sum_{y_1} P(y_1)\mathrm{Tr}(A_a^x B_{b_2}^{y_2} \rho'_{AB}), \qquad \rho'_{AB} = \mathrm{Tr}_C(\rho'_{ABC}). \tag{4.31}$$

Note that, since the evolution is random, in Eq. 4.31 we include the sum over all the possible realizations of y_1 weighted by their occurrence probability $P(y_1)$. Whereas, in Eq. 4.30 we require the probability given a certain realization of y_1, so we do not have to sum over y_1.

To get some insight into the system, we calculate the states ρ'_{ABC}, ρ'_{AB} and ρ'_{AC}. Henceforth, when it is not ambiguous, we drop the labels that specify the Hilbert space on which the operators act, together with a, b_i, x and y_i. The final state is easily calculated using Eq. 4.25

$$\rho'_{ABC} = \pi^+\rho_{ABC}\pi^+ + \pi^+\rho_{ABC}e^{-i\epsilon\sigma_z}\pi^- + \pi^- e^{i\epsilon\sigma_z}\rho_{ABC}\pi^+ + \pi^- e^{i\epsilon\sigma_z}\rho_{ABC}e^{-i\epsilon\sigma_z}\pi^-. \tag{4.32}$$

It is possible to show that the following equations hold

$$\mathrm{Tr}_C(\rho_{ABC}) = \mathrm{Tr}_C(e^{i\epsilon\sigma_z}\rho_{ABC}e^{-i\epsilon\sigma_z}) = \rho_{AB} \tag{4.33}$$

$$\mathrm{Tr}_C(\rho_{ABC}e^{-i\epsilon\sigma_z}) = \mathrm{Tr}_C(e^{i\epsilon\sigma_z}\rho_{ABC}) = \rho_{AB}\cos\epsilon, \tag{4.34}$$

with which it is easy to calculate Alice and Bob2's state, given a certain realization of y_1:

$$\rho'_{AB} = \pi^+\rho_{AB}\pi^+ + \cos\epsilon\left(\pi^+\rho_{AB}\pi^- + \pi^-\rho_{AB}\pi^+\right) + \pi^-\rho_{AB}\pi^- \tag{4.35}$$

$$= \rho_{AB}\cos\epsilon + (1-\cos\epsilon)\left(\pi^+\rho_{AB}\pi^+ + \pi^-\rho_{AB}\pi^-\right). \tag{4.36}$$

Eq. 4.36 shows that the final state shared by Alice and Bob2 is a linear combination of the initial singlet state and the decohered singlet state, weighted by a function of the parameter ϵ. If $\epsilon = 0$, the controlled gate, and hence U_{y_1}, acts as the identity, as a result $\rho'_{AB} = \rho_{AB}$. On the contrary, when $\epsilon = \pi/2$, ρ'_{AB} is completely decohered. According to Silva et al., 2015, $\cos\epsilon$ corresponds to the quality factor F of Bob1's measurement which quantifies the amount of disturbance given by Bob1's weak measurement. In particular, if $F = 0$ Bob1 performs a strong measurement, preventing Bob2 to be nonlocal with Alice, whereas if $F = 1$, Bob1 does not disturb the system at all.

Regarding Alice and Bob1's shared state, we have the following useful equations

$$\mathrm{Tr}_B(\pi_B^+\rho_{AB}\pi_B^+) = \pi_A^-/2, \tag{4.37}$$

$$\mathrm{Tr}_B(\pi_B^-\rho_{AB}\pi_B^-) = \pi_A^+/2, \tag{4.38}$$

$$\mathrm{Tr}_B(\pi_B^+\rho_{AB}\pi_B^-) = \mathrm{Tr}_B(\pi_B^-\rho_{AB}\pi_B^+) = 0, \tag{4.39}$$

hence

$$\rho'_{AC} = \frac{1}{2}\left(\pi_A^- |+\rangle\langle+| + \pi_A^+ e^{i\epsilon\sigma_z}|+\rangle\langle+| e^{-i\epsilon\sigma_z}\right). \tag{4.40}$$

We now explicitly calculate the outcome probabilities in Eqs. 4.30 and 4.31. Using the following equations

$$\mathrm{Tr}_A(A_a^x \pi_A^\pm) = \frac{1}{2}(1 \pm u_a^x \cdot w_{b_1}^{y_1}), \tag{4.41}$$

$$\mathrm{Tr}_C(B_{b_1}^{y_1}|+\rangle\langle+|) = \delta_{b_1+}, \tag{4.42}$$

$$\mathrm{Tr}_C(B_{b_1}^{y_1} e^{i\epsilon\sigma_z}|+\rangle\langle+| e^{-i\epsilon\sigma_z}) = \delta_{b_1+} - b_1 \sin^2\epsilon, \tag{4.43}$$

we obtain the outcome probabilities for Alice and Bob1's measurements

$$P(ab_1|xy_1) = \frac{1}{4}\left(1 + b_1 - b_1 \sin^2\epsilon(1 + a u^x \cdot w^{y_1})\right). \tag{4.44}$$

while using

$$\mathrm{Tr}_{AB}(A_a^x B_{b_2}^{y_2} \rho_{AB}) = \frac{1}{4}(1 - u_a^x \cdot v_{b_2}^{y_2}), \tag{4.45}$$

$$\mathrm{Tr}_{AB}(A_a^x B_{b_2}^{y_2} \pi^\pm \rho_{AB} \pi^\pm) = \frac{1}{8}(1 \mp u_a^x \cdot w_{b_1}^{y_1})(1 \pm v_{b_2}^{y_2} \cdot w_{b_1}^{y_1}), \tag{4.46}$$

we have the outcome probabilities for Alice and Bob2's measurements

$$P(ab_2|xy_2) = \frac{1}{4}\sum_{y_1} P(y_1)\Big(1 - ab_2(u^x \cdot v^{y_2})\cos\epsilon - ab_2(u^x \cdot w^{y_1})(v^{y_2} \cdot w^{y_1})(1 - \cos\epsilon)\Big). \tag{4.47}$$

We go on with the correlations $E_{xy_i} = \sum_{ab_i=\pm1} ab_i P(ab_i|xy_i)$. Note that whenever the probability has the form $P(ab_i|xy_i) = \Gamma_0 + a\Gamma_1 + b_i\Gamma_2 + ab_i\Gamma_3$ the correlations is $E_{xy_i} = 4\Gamma_3$. It follows that for Alice and Bob1

$$E_{xy_1} = -\sin^2\epsilon(u^x \cdot w^{y_1}) \tag{4.48}$$

while for Alice and Bob2

$$E_{xy_2} = -\sum_{y_1} P(y_1)\left(\cos\epsilon(u^x \cdot v^{y_2}) + (1 - \cos\epsilon)(u^x \cdot w^{y_1})(v^{y_2} \cdot w^{y_1})\right) \tag{4.49}$$

Finally, the CHSH inequalities $I = E_{00} + E_{10} + E_{01} - E_{11} \leq 2$ read

$$I_{CHSH}^{(1)} = \Theta_0 \sin^2\epsilon \leq 2, \tag{4.50}$$

$$I_{CHSH}^{(2)} = \Theta_1 \cos\epsilon + \Theta_2(1 - \cos\epsilon) = \Theta_2 + (\Theta_1 - \Theta_2)\cos\epsilon \leq 2, \tag{4.51}$$

with

$$\begin{aligned}
\Theta_0 &= -\left(u^0 \cdot w^0 + u^1 \cdot w^0 + u^0 \cdot w^1 - u^1 \cdot w^1\right),\\
\Theta_1 &= -\left(u^0 \cdot v^0 + u^1 \cdot v^0 + u^0 \cdot v^1 - u^1 \cdot v^1\right),\\
\Theta_2 &= -\sum_{y_1} P(y_1)\Big((u^0 \cdot w^{y_1})(v^0 \cdot w^{y_1}) + (u^1 \cdot w^{y_1})(v^0 \cdot w^{y_1}) + \\
&\qquad\qquad (u^0 \cdot w^{y_1})(v^1 \cdot w^{y_1}) - (u^1 \cdot w^{y_1})(v^1 \cdot w^{y_1})\Big).
\end{aligned}$$

We now give some insight on the set of measurements that have to be chosen to maximize the violation of both CHSH inequalities: $I^{(1)}_{CHSH} \leq 2$ and $I^{(2)}_{CHSH} \leq 2$. It is convenient to introduce the parameter $x = \sin^2\epsilon$ so that Eqs. (4.50) and (4.51) become

$$I^{(1)}_{CHSH} = \Theta_0 x \leq 2, \tag{4.52}$$

$$I^{(2)}_{CHSH} = \Theta_2 + (\Theta_1 - \Theta_2)\sqrt{1-x} \leq 2. \tag{4.53}$$

Since $x \in [0,1]$, the violation of Eq. (4.52) is possible only if $\Theta_0 > 0$, which is when $I^{(1)}_{CHSH}(x)$ is strictly increasing. We need also to restrict to the case $\Theta_1 > \Theta_2$, otherwise Eq. (4.53) cannot be violated. Indeed, in the case $\Theta_1 \leq \Theta_2$, $I^{(2)}_{CHSH}(x)$ is monotonically increasing, but since for $x = 1$ Alice and Bob2 are no more nonlocal, due to the strong measurement performed by Bob1, we have $I^{(2)}_{CHSH}(1) \leq 2$, therefore $I^{(2)}_{CHSH}(x) \leq I^{(2)}_{CHSH}(1) \leq 2$. Then the constraints $\Theta_0 > 0$ and $\Theta_1 > \Theta_2$ imply that if there is simultaneous violation then there is a unique $\tilde{x}$ such that $I^{(1)}_{CHSH}(\tilde{x}) = I^{(2)}_{CHSH}(\tilde{x})$, this can be easily understood looking at Fig. 4.2. In our set up, we want to have ϵ such that $\sin^2\epsilon = \tilde{x}$, so that we have the maximum violation of both inequalities. Our aim is to choose the set of measurements that maximize $I^{(1)}_{CHSH}(\tilde{x})$, being $\tilde{x}$ the solution of $I^{(1)}_{CHSH}(x) = I^{(2)}_{CHSH}(x)$:

$$\tilde{x} = \beta - \frac{1}{2}(\alpha-\beta)^2 + \frac{1}{2}\sqrt{(2\beta - (\alpha-\beta)^2)^2 - 4(\beta^2 - (\alpha-\beta)^2)} \tag{4.54}$$

where $\alpha = \Theta_1/\Theta_0$ and $\beta = \Theta_2/\Theta_0$. In all generality, this is an optimization problem over 11 free real parameters. 10 real parameters come from the vectors in the Bloch sphere that define Θ_i: two parameters per each of the vectors u^1, w^0, w^1, v^0, v^1; u^0 is omitted since Θ_i are invariant for a rotation in the Bloch sphere so u^0 can be fixed. The last real parameter comes from the probability $P(y_1)$. This problem is computationally intensive, but we may simplify it making the following approximation. It is quite natural to require Θ_0 to be the highest possible: $\Theta_0 = 2\sqrt{2}$. This is accomplished choosing:

$$w_0 = \sigma_z, \qquad u_0 = -\frac{\sigma_z + \sigma_x}{\sqrt{2}},$$

$$w_1 = \sigma_x, \qquad u_1 = \frac{-\sigma_z + \sigma_x}{\sqrt{2}}.$$

So we are left with 5 free real parameters: v^0, v^1 and $P(0)$. The numerical optimization leads to the final choice

$$w_0 = v_0 = \sigma_z, \qquad u_0 = -\frac{\sigma_z + \sigma_x}{\sqrt{2}}, \tag{4.55}$$

$$w_1 = v_1 = \sigma_x, \qquad u_1 = \frac{-\sigma_z + \sigma_x}{\sqrt{2}}, \tag{4.56}$$

and $P(y_1 = 0)$ being any number between 0 and 1. The corresponding Bloch vectors are

$$\begin{aligned} \vec{w}_0 = \vec{v}_0 &= (0,0,1), & \vec{w}_0^{\perp} = \vec{v}_0^{\perp} &= (0,0,-1), \\ \vec{w}_1 = \vec{v}_1 &= (1,0,0), & \vec{w}_1^{\perp} = \vec{v}_1^{\perp} &= (-1,0,0), \\ \vec{u}_0 &= \left(-\frac{1}{\sqrt{2}},0,-\frac{1}{\sqrt{2}}\right), & \vec{u}_0^{\perp} &= \left(\frac{1}{\sqrt{2}},0,\frac{1}{\sqrt{2}}\right), \\ \vec{u}_1 &= \left(\frac{1}{\sqrt{2}},0,-\frac{1}{\sqrt{2}}\right), & \vec{u}_1^{\perp} &= \left(-\frac{1}{\sqrt{2}},0,\frac{1}{\sqrt{2}}\right). \end{aligned}$$

For simplicity we choose $P(y_1) = \frac{1}{2}$. Since u, w and v lie on the same plane of the Boch sphere, we have $\sum_{y_1} P(y_1)(u^x \cdot w^{y_1})(v^{y_2} \cdot w^{y_1}) = \frac{1}{2} u^x \cdot v^{y_2}$. Consequently, $\Theta_2 = \frac{1}{2}\Theta_1$ and the inequalities read

$$I^{(1)}_{CHSH} = \Theta_0 \sin^2 \epsilon, \tag{4.57}$$

$$I^{(2)}_{CHSH} = \frac{1}{2}\Theta_1(1 + \cos\epsilon). \tag{4.58}$$

We also have $u^0 \cdot w^0 = u^1 \cdot w^0 = u^0 \cdot w^1 = -\frac{1}{\sqrt{2}}$ and $u^1 \cdot w^1 = \frac{1}{\sqrt{2}}$, the same equalities hold substituting w with v, hence $\Theta_0 = \Theta_1 = 2\sqrt{2}$ and finally

$$I^{(1)}_{CHSH} = 2\sqrt{2}\sin^2 \epsilon, \tag{4.59}$$

$$I^{(2)}_{CHSH} = \sqrt{2}(1 + \cos\epsilon). \tag{4.60}$$

Fig. 4.2 shows the result: the maximum violation is found at $\sin^2 \epsilon = 3/4$ so that $I^{(1)}_{CHSH} = I^{(2)}_{CHSH} = \frac{3}{2}\sqrt{2} \sim 2.12$.

4.4 EXPERIMENTAL IMPLEMENTATION

4.4.1 *Setup*

Fig. 4.3 illustrates the setup of our experiment. We generate single photon entangled pairs by SPDC in a 30 mm periodically poled KTP crystal placed in a polarization-based Sagnac interferometer (Kim, Fiorentino, and Wong, 2006). The crystal is pumped by a single mode UV laser at 405 nm and 4 mW of power. The pair of photons is collected into single-mode fibers to inject

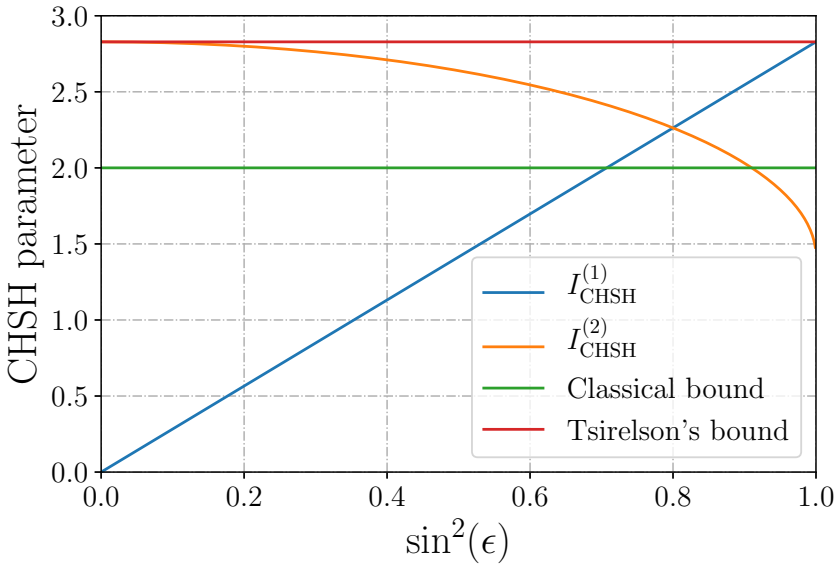

Figure 4.2: Inequalities for the best measurements.

them on the measurement apparatus (see Appendix A for more details). To preserve the singlet state after the birefringence introduced by the fibers we place a polarization controller at Alice's side. Indeed, one of the properties of the singlet state is to be preserved if a unitary transformation $\tilde{U} = U \otimes U$ is applied

$$|\Psi\rangle = \tilde{U}\,|\Psi\rangle\,, \tag{4.61}$$

with U acting on the single photon. Hence, the polarization control acting on a single photon is placed to tune the unitary of the Alice's fiber so to equal the one of Bob.

The receiving apparatuses of Alice and Bob2 implement a scheme for measuring the polarization of the photons. An half wave plate HWP is placed before a PBS to measure on two arbitrary orthogonal states in the X-Z plane of the Bloch sphere (linear polarization). The transmitted and reflected photons from the PBS are detected using SPADs. Before reaching Bob2, the photons pass through Bob1's apparatus. The unitaries R and $R^\dagger$ are performed by HWP2 and HWP5, respectively. The fast axis of both plates is rotated of the same angle to rotate the polarization. The control phase gate is implemented by exploiting a Sagnac interferometer, with clockwise and anticlockwise paths spatially separated, plus a LCR after one output port. In this configuration, the ancilla is given by the paths of the interferometer. HWP3 and HWP4 provide a phase retardation between horizontal and vertical polarization, say ϵ_0 and ϵ_1 respectively. Indeed, their slow axes are parallel to the vertical polarization and the phase retardation is adjusted by tilting them. The phase difference between the two paths ϕ is adjusted by tilting a thin glass plate. Finally, the liquid crystal is used as a phase retarder between horizontal and vertical

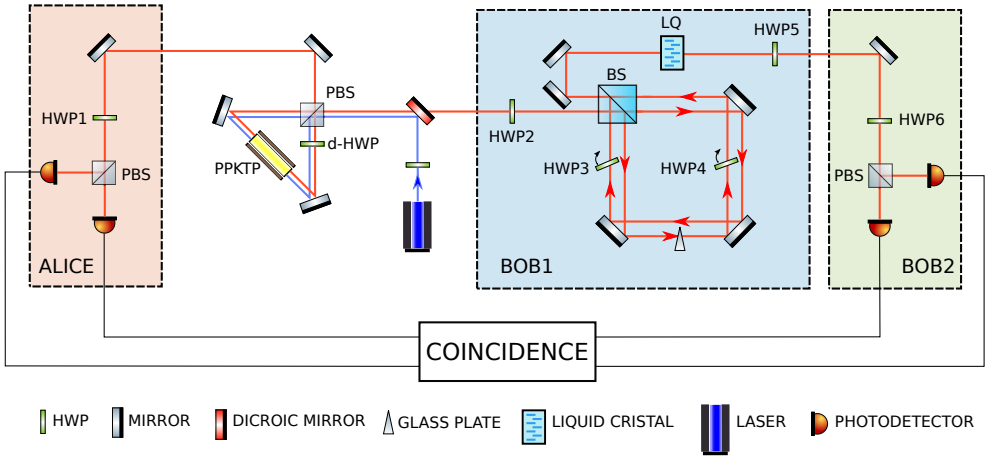

Figure 4.3: Scheme of the experimental setup. The polarization-entangled photon-pair source comprises a PPKTP crystal, in a Sagnac interferometer, pumped by a laser diode at 404.5 nm. The entangled photons are collected and sent to Alice and Bobs apparatuses. Alice and Bob2 implement a scheme, consisting of a HWP (HWP1 and HWP6) and a PBS, to measure the polarization on two linear bases. The transmitted and reflected photons from the PBS are detected by single photon avalanche diodes. Bob1's apparatus performs the weak measurement. HWP2 and HWP5 implement the transformations R and $R^\dagger$, respectively. HWP3 and HWP4 are placed in a Sagnac interferometer with clockwise and anticlockwise paths spatially separated. In particular, HWP3 (HWP4) is placed in the clockwise (anticlockwise) path, and is used as a phase retarder between horizontal and vertical polarization. The phase difference between the two paths is adjusted by tilting a thin glass plate. Finally, a LCR is used as a phase retarder between horizontal and vertical polarization.

polarization, to compensate for the mean polarization phase introduced by HWP3 and HWP4.

To show that Bob1's apparatus implements the scheme in Fig. 4.1, suppose a pure state $|\psi_{in}\rangle = \alpha\,|\omega_{y_1}\rangle + \beta\,|\omega_{y_1}^{\perp}\rangle$ is given as an input. The HWP2 rotates the state into $\alpha\,|H\rangle + \beta\,|V\rangle$, which enters the interferometer. After the first passage through the BS, the glass plate and the HWP3 and HWP4, the state, just before the impinging the BS for the second time, becomes

$$\frac{ie^{i\phi}}{\sqrt{2}}\left(\alpha\,|H\rangle + \beta e^{i\epsilon_0}\,|V\rangle\right)|0\rangle + \frac{1}{\sqrt{2}}\left(\alpha\,|H\rangle + \beta e^{i\epsilon_1}\,|V\rangle\right)|1\rangle\,, \tag{4.62}$$

being $|0\rangle$ and $|1\rangle$ the clockwise and anticlockwise path respectively and ϕ the phase difference between them. At the exit of the interferometer we have that, setting the glass plate such that $\phi = 0$, the state is

$$\alpha\,|H\rangle\,|2\rangle + \beta e^{i\frac{\epsilon_0+\epsilon_1}{2}}\,|V\rangle\,(\cos\epsilon\,|2\rangle + \sin\epsilon\,|3\rangle)\,, \tag{4.63}$$

where $|2\rangle$ and $|3\rangle$ are the two output ports of the interferometer and $\epsilon = \frac{\epsilon_1 - \epsilon_0}{2}$. If the phase retardation of the LCR [1] is set at $-\frac{\epsilon_0 + \epsilon_1}{2}$, the state is changed into

$$\alpha |H\rangle |2\rangle + \beta |V\rangle (\cos\epsilon |2\rangle + \sin\epsilon |3\rangle) . \tag{4.64}$$

Hence, the Sagnac interferometer plus the LCR implements a control phase gate with phase $\epsilon = \frac{\epsilon_1 - \epsilon_0}{2}$. Finally, the HWP5 rotates the state into

$$|\psi_{out}\rangle = \alpha |\omega_{y_1}\rangle |2\rangle + \beta |\omega_{y_1}^{\perp}\rangle (\cos\epsilon |2\rangle + \sin\epsilon |3\rangle) . \tag{4.65}$$

In our setup, we look at one single output port at a time, swapping $|2\rangle$ and $|3\rangle$ by tilting the glass plate. Indeed, by changing the global phase ϕ from 0 to π the transformation $|2\rangle \to -|3\rangle$ and $|3\rangle \to |2\rangle$ applies.

Alice chooses between the two measurement bases $(\sigma_x - \sigma_z)/\sqrt{2}$ and $-(\sigma_x + \sigma_z)/\sqrt{2}$; these bases are obtained from the HWP1 rotated by the angles 11.25° and 33.75° respectively. Bob1 and Bob2 choose between measurement bases σ_z and σ_x, given by a rotation of 0° and 22.5° of the couple HWP2-HWP5 and of HWP6, respectively. Furthermore, Bob1 tilts the glass plate into two positions corresponding to the phase difference $\phi = 0$ and $\phi = \pi$, to swap the output port. In total, a single measurement of the Bell parameters $I^{(1)}_{\text{CHSH}}$ and $I^{(2)}_{\text{CHSH}}$ requires 16 data acquisitions, one per each different configuration of the HWPs and the glass plate. In all measurements, we set 30 seconds of data acquisition, with an average coincidence rate of 700 counts per second.

4.4.2 *Alignment of the setup*

Our scheme requires that just after the fiber output from the source the entangled photons should be described by a singlet state. As said above, the presence of the single mode fibers acts as a unitary transformation that has to be compensated through the polarization control. However, the alignment must be verified via the polarization measurement of Alice and Bob2's apparatuses, while Bob1 should not alter the state. The procedure for the state preparation consists of the following steps:

- **Bob1 compensation**. We block the clockwise arm of the interferometer and rotate the HWP2 and HWP5 so that their fast axes are parallel to the horizontal polarization. In this configuration, the apparatus may introduce a phase between the horizontal and vertical polarizations. This can be compensated by applying the opportune voltage on the LCR. To find it we inject a 808 nm laser and insert a polarizer to project the beam polarization onto the diagonal state, before HWP2. Then, we make Bob2 measure on the diagonal and anti-diagonal basis, by rotating HWP6 at

1 The reasoning holds considering a LCR after each output port of the interferometer. In practice, we need a single LCR since we use only one output port.

22.5 degrees. Finally we set the voltage to minimize the power of the beam from the anti-diagonal port.

- **Fiber compensation**. Keeping the same arm of the interferometer unblocked, we remove the polarizer and inject the entangled-photons source. The anti-correlation between the horizontal and vertical basis is set by rotating HWP1 and HWP6 with horizontal fast axis (Alice and Bob2 measure on the $|H\rangle$ and $|V\rangle$ basis) and adjusting the polarization controller to minimize the coincidence counts for correlated results ($N_{H,H}$ and $N_{V,V}$). At this point the only degree of freedom left unset is a possible phase ϕ'

$$|\Psi'\rangle = \frac{1}{2}\left(|H\rangle|V\rangle + e^{i\phi'}|V\rangle|H\rangle\right), \tag{4.66}$$

that we compensate by tilting a HWP, with horizontal fast axis, after the polarization controller. To set the right tilt angle we let Alice and Bob2 measure on the diagonal and anti-diagonal base, and tilt the plate to minimize the coincidence counts for correlated results ($N_{D,D}$ and $N_{A,A}$).

After the state preparation, we optimize the measurement setup of Bob1. The procedure consists of setting the strength of the measurement by tilting the HWPs inside the interferometer and then compensating the polarization phase with the LCR.

- **Strength of the measurement**. HWP3 and HWP4 introduce a phase shift between the horizontal and vertical polarization, due to the birefringence, depending on the tilt angle θ. Considering the two polarization separately we model the phase change with the following equations

$$\begin{aligned} \phi_H &= \frac{\xi_H}{\cos\theta} + \phi_{0H} \quad \xi_H = \frac{2\pi}{\lambda} d(n_H - n_0) \\ \phi_V &= \frac{\xi_V}{\cos\theta} + \phi_{0V} \quad \xi_V = \frac{2\pi}{\lambda} d(n_V - n_0), \end{aligned} \tag{4.67}$$

where d is the thickness of the plate, n_H (n_V) is the refraction index along the horizontal (vertical) polarization, n_0 is the refractive index of the air. Hence, the phase is

$$\epsilon = \phi_V - \phi_H = \frac{\Delta\xi}{\cos\theta} + \Delta\phi, \tag{4.68}$$

with $\Delta\xi = \xi_V - \xi_H$ and $\Delta\phi = \phi_{0V} - \phi_{0H}$. By estimating the parameters $\Delta\xi$ and $\Delta\phi$ for HWP3 and HWP4 we characterize the phase shift ϵ for any tilt angle. Hence, we can set the strength of the measurement ϵ so that

$$\epsilon = \frac{\epsilon_1 - \epsilon_0}{2} = \frac{\Delta\xi_1}{\cos\theta_1} - \frac{\Delta\xi_0}{\cos\theta_0} + \Delta\phi_1 - \Delta\phi_0. \tag{4.69}$$

- **Interferometer compensation**. The voltage on the LCR is set with the following procedure. We remove any beam dump inside the interferometer, allowing the two paths to interfere. We set *Alice*'s measurement on the diagonal and anti-diagonal basis, so that the heralded photon, entering *Bob1* apparatus, is either in the anti-diagonal or diagonal state. We set HWP2 and HWP5 with the fast axis parallel to the diagonal polarization to left unaltered the state of the heralded photon. Considering the case in which the global phase of the interferometer is $\phi = 0$ and $a = \pm 1$ the outcome of *Alice* measurement, the state at the output of the interferometer becomes

$$|\psi_a\rangle = |H\rangle - ae^{i\frac{\epsilon_1+\epsilon_0}{2}} \cos\epsilon\, |V\rangle\,. \tag{4.70}$$

Let χ be the phase introduced by the LCR. Then the state becomes

$$|\psi_a\rangle = |H\rangle - ae^{i\left(\frac{\epsilon_1+\epsilon_0}{2}+\chi\right)} \cos\epsilon\, |V\rangle\,. \tag{4.71}$$

Therefore, the outcome probabilities for *Bob2* apparatus ($b_2 = \pm 1$), conditioned on the *Alice* measurement a are

$$\mathrm{P}\left(b_2|a\right) = \frac{1}{2}\left(1 - b_2 a \frac{\cos\epsilon}{(1+\cos^2\epsilon)} \cos\left(\chi + \frac{\epsilon_1+\epsilon_0}{2}\right)\right). \tag{4.72}$$

Hence, the condition $\chi = -\frac{\epsilon_1+\epsilon_0}{2}$ is found by maximizing the coincidence counts $N\left(b_2 = -a|a\right) \propto \mathrm{P}\left(b_2 = -a|a\right)$ and minimizing $N\left(b_2 = a|a\right) \propto \mathrm{P}\left(b_2 = a|a\right)$.

This concludes the alignment of the setup and we proceed with the run of the experiment.

4.4.3 *Data analysis and results*

According to the standard procedure in Bell inequality violation we did not subtract accidental coincidences.

We measured $I^{(1)}_{\mathrm{CHSH}}$ and $I^{(2)}_{\mathrm{CHSH}}$ for several values of ϵ in the range $[0, \pi/2]$. Fig. 4.4 shows the obtained experimental results, demonstrating a good agreement with the theoretical model. For $\epsilon = 0$, there is no interaction between the polarization and the ancillary state. Indeed, $I^{(1)}_{\mathrm{CHSH}}$ is comparable to 0, while $I^{(2)}_{\mathrm{CHSH}}$ is close to the Tsirelson's bound. By increasing ϵ, we demonstrate an increase of $I^{(1)}_{\mathrm{CHSH}}$ and a reduction of $I^{(2)}_{\mathrm{CHSH}}$, following the expected theoretical curves.

It is worth noticing that in Fig. 4.4, the experimental I_{CHSH} values underestimate those expected by the theoretical predictions. In our calculations we considered as sources of the errors on the CHSH parameters only the poissonian errors on the coincidences, obtaining an apparent incompatibility between

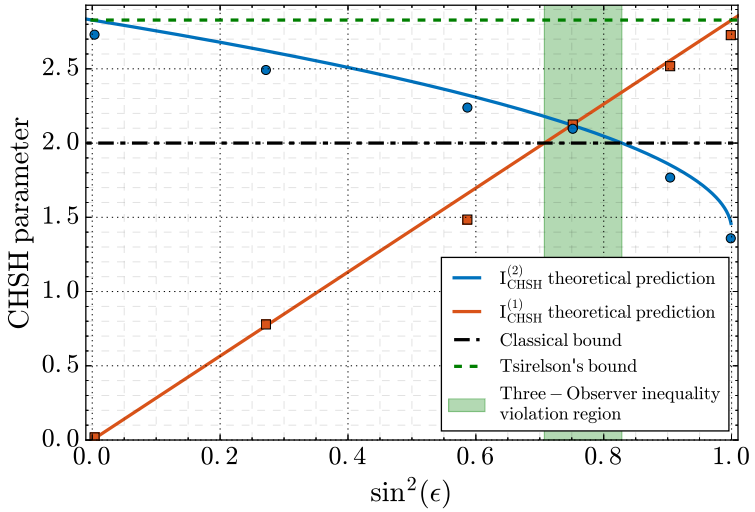

Figure 4.4: Measurements of $I^{(1)}_{\mathrm{CHSH}}$ (squares) and $I^{(2)}_{\mathrm{CHSH}}$ (circles) for several values of ϵ. The red and green solid lines show the expected values of $I^{(1)}_{\mathrm{CHSH}}$ and $I^{(2)}_{\mathrm{CHSH}}$ (Eq. 4.57), while the dash-dotted and dashed lines indicate classical and Tsirelson's bounds respectively. The green region highlights the values of ϵ in which double violation is expected. Poissonian errors are within the dimension of the points.

the experimental data and the predictions. The reason of this incompatibility is that in our experiment we do not have an easy-accessible procedure to estimate all the systematic errors affecting the I_{CHSH} measurement method. Factors as the impurity of the analyzed singlet state, or the systematic errors introduced by the basis exchangers (HWP rotators), or the errors due to the environment instability (that may affect optical fibers, the mirrors and the interferometer) are not kept into account by the poissonian variance. These sources of error act on the overall I_{CHSH} estimation reducing its value.

The interesting region is the one around $\epsilon = \pi/3$, where both $I^{(1)}_{\mathrm{CHSH}}$ and $I^{(2)}_{\mathrm{CHSH}}$ are expected to be above the classical bound – green region in Fig. 4.4. To give a larger statistical evidence of the double violation in this region, we performed consecutive measurements with two different values of ϵ. In Fig. 4.5 **(Left)**, we show the results of 8 consecutive measurements with $\epsilon = 1.049 \pm 0.002$. In all trials, both $I^{(1)}_{\mathrm{CHSH}}$ and $I^{(2)}_{\mathrm{CHSH}}$ were above the classical bound, fluctuating around the mean values $I^{(1)}_{\mathrm{CHSH}} = 2.125 \pm 0.003$ and $I^{(2)}_{\mathrm{CHSH}} = 2.096 \pm 0.003$. The data acquisition of a single trial took about eight minutes to finish, for a total acquisition time of one hour. This proves the reproducibility of the violation and the stability of our setup. A second series of trials, with $\epsilon = 1.053 \pm 0.002$ is shown in Fig. 4.5 **(Right)**. Similarly to the previous case, both $I^{(1)}_{\mathrm{CHSH}}$ and $I^{(2)}_{\mathrm{CHSH}}$ are above the classical bound

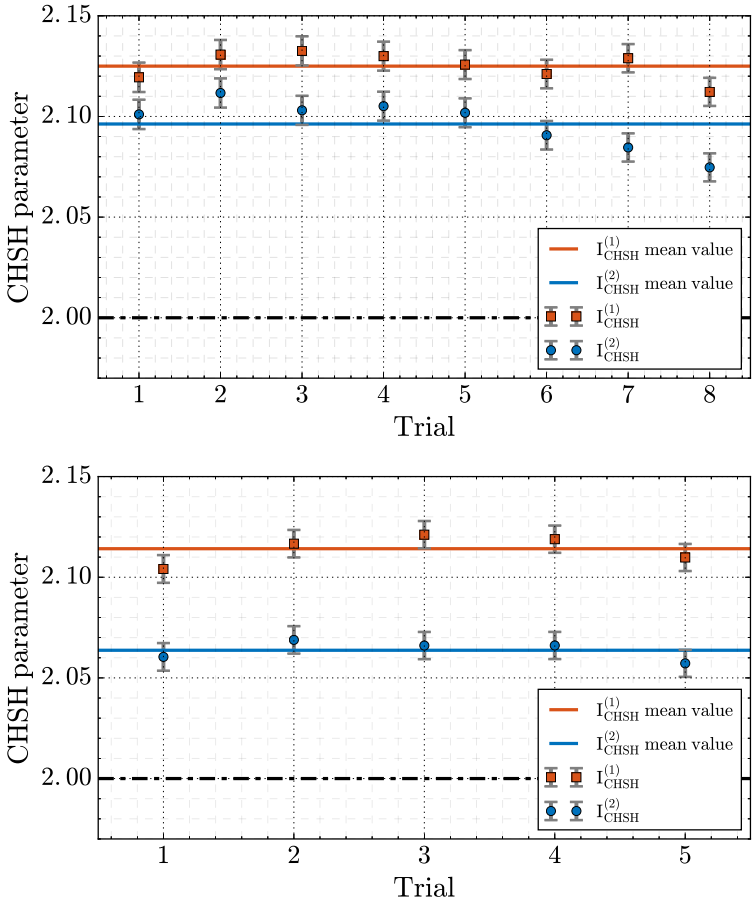

Figure 4.5: Measurements of $I^{(1)}_{\text{CHSH}}$ (squares) and $I^{(2)}_{\text{CHSH}}$ (circles) in two consecutive series of trials. Red and blue solid lines indicate the mean value of $I^{(1)}_{\text{CHSH}}$ and $I^{(2)}_{\text{CHSH}}$ respectively. **(Left)** Eight consecutive trials were performed in an hour, with $\epsilon = 1.049 \pm 0.002$. Considering the poissonian error, the measurements show a violation of 10 standard deviations, fluctuating around mean values of $I^{(1)}_{\text{CHSH}} = 2.125 \pm 0.003$ and $I^{(2)}_{\text{CHSH}} = 2.096 \pm 0.003$. **(Right)** Another series of five consecutive trials were performed within a hour, with $\epsilon = 1.053 \pm 0.002$. Similarly to the previous case, all the measurements show a violation of 10 standard deviation, fluctuating around mean values of $I^{(1)}_{\text{CHSH}} = 2.114 \pm 0.003$ and $I^{(2)}_{\text{CHSH}} = 2.064 \pm 0.003$.

for the entire period of the acquisition, with $I^{(1)}_{\text{CHSH}} = 2.114 \pm 0.003$ and $I^{(2)}_{\text{CHSH}} = 2.064 \pm 0.003$.

4.5 DISCUSSION

We have shown experimentally that a double CHSH inequality violation between two different pairs of observers can be achieved by using a single two-qubit entangled state of two photons. We recall that the three observers choose randomly between the two possible measurements, with no agree-

ment on the measurement strategy. Thanks to the stability of our setup (larger than 1 hour), we could perform several double violations increasing the statistical evidence of the experiment. The double violation was tested and repeated for different values of ϵ, the interaction strength of Bob1's weak measurement. The experimental data well reproduce the theoretical model when ϵ is changed.

Our measurement can be seen as a dimension-independent entanglement witness between Alice and Bob1 or between Alice and Bob2. Indeed, Bell inequalities, differently from most other entanglement witnesses, work without any assumption on the dimension of the input state. No separable states (in any dimension) can achieve the violation of a Bell inequality. However, the entanglement between Alice-Bob1 and between Alice-Bob2 does not violate the monogamy of entanglement since the Bob1 particle is sent to Bob2 after the (weak) measurement.

It is worth noticing that by slightly changing the measurement setting at Bob1's side it is possible to obtain an optimal weak measurement. Indeed, if the phases of the glass plate are set to $\phi = \phi_0$ and $\phi = \phi_0 + \pi$ the value of the A-$B1$ inequality can be varied as $I^{(1)}_{\mathrm{CHSH}} = 2\sqrt{2}[\cos\phi_0 - \cos(\phi_0 - \epsilon)])$, maximized to $I^{(1)}_{\mathrm{CHSH}} = 2\sqrt{2}\sin\epsilon$ for $\phi_0 = \epsilon - \pi/2$. The change in ϕ_0 does not change the value of $I^{(2)}_{\mathrm{CHSH}}$: this corresponds to a measurement that keeps the disturbance on the state fixed with a varying information gained on it. Our scheme demonstrates that even if the weak measurement is not optimal it is possible to achieve a double violation of the inequality.

The achievement of double violation and the realization of a simple weak measurement scheme have important applications for QRNG (Curchod et al., 2017), or for Quantum Key Distribution exploiting weak measurements (Troupe and Farinholt, 2015). In Curchod et al., 2017, for instance, it was shown that, by using sequences of weak measurements to violate a multi-user Bell inequality, it is possible to certify any amount of random bits from a pair of pure entangled qubits.

5

DIRECT RECONSTRUCTION OF A QUANTUM STATE

The measurement of the state of a system is one of the most important problems of quantum mechanics. The most common characterization of a general quantum state is given by a density operator. The usual way of reconstructing it is known as QST. If d is the dimension of the system, QST employs d^2 *linearly independent* projectors (James et al., 2001; Schmied, 2016) and can become impractical for large d. An alternative approach is based on the determination of the Moyal quasicharacteristic function by sequentially measuring two conjugate variables (Di Lorenzo, 2013a,b).

Recently, Lundeen *et al.* (Lundeen and Bamber, 2012; Lundeen et al., 2011) proposed new ways, called *Direct Reconstruction*, to determine the density matrix through weak measurements, processes in which the measuring device (called pointer) perturbs only slightly the system which it is coupled to, so as to limit the collapse of its state (Aharonov, Albert, and Vaidman, 1988; Duck, Stevenson, and Sudarshan, 1989; Ritchie, Story, and Hulet, 1991). These techniques have already been experimentally verified (Salvail et al., 2013; Thekkadath et al., 2016) and thoroughly compared to QST (Maccone and Rusconi, 2014). One of such protocols has the advantage of finding an entire density operator by interacting with only $d + 1$ components of the state of a system (however, we note that the total number of measurements is $O(d^2)$ as in QST). However, the use of weak values implies that all these strategies are approximated and affected by great statistical errors: there is a trade-off between the validity of the approximation (improved by weakening the interaction) and the statistical uncertainties (improved by increasing the interaction).

It has been shown that for pure states it is possible to extend these schemes to arbitrary coupling strength (even to the case of *strong measurements*) without any approximation (Denkmayr et al., 2017; Gross et al., 2015; Vallone and Dequal, 2016; Zhang, Wu, and Chen, 2016; Zou, Zhang, and Song, 2015). Other methods valid for pure states were presented by Baldwin, Deutsch, and Kalev, 2016; Goyeneche et al., 2015, whereas a generalization for mixed states was also proposed by Vallone and Dequal, 2016 and Zhu, Zhang, and Wu, 2016.

In this Chapter, we introduce a protocol for the (exact) Direct Reconstruction of the density operator without weak measurements. We also report on our experimental realization applied to the polarization state of single pho-

tons. We finally show that our method overcomes the weak measurement proposal (Thekkadath et al., 2016) in terms of accuracy and statistical uncertainty and we discuss the relation with standard QST.

5.1 DIRECT MEASUREMENT OF THE WAVE FUNCTION

By *direct measurement of the wave function* we mean a measurement whose outcome is proportional to the element of the wave function. More precisely, suppose to have a pure state described by an unknown unit vector $|\phi_S\rangle$ in a d-dimensional Hilbert space $\mathscr{H}_S$. Given an orthonormal basis $\{|a_j\rangle \mid j = 1..d\}$, the state is fully characterized by the elements $\{c_j \equiv \langle a_j|\phi_S\rangle \mid j = 1..d\}$, since

$$\phi_S = \sum_{j=1}^{d} c_j \, |a_j\rangle \, . \tag{5.1}$$

Therefore, the outcome of a direct measurement is such that its value is proportional to either $\Re(c_j)$ or $\Im(c_j)$. Note that c_j is in general a complex number, hence we have to indicate the real or imaginary part since the mere result of a measurement is a real number.

On the contrary, with the standard methods of state reconstruction, i.e. QST, the single element c_j requires a sequence of measurement whose results are then post-processed.

In this section, I will briefly describe the idea behind the direct measurement from the original point of view, in which the *weak measurement* plays a fundamental role. I will first introduce the case of pure states and then move to the general method for density operators.

5.1.1 *Direct Weak Reconstruction of Pure States*

The demonstration is quite straightforward, in the case of pure states, once understood what a weak value is (see Section 1.7). Consider the case in which, after a weak interaction between the system and the pointer, the system state is post-selected into a state $|b_0\rangle = \frac{1}{\sqrt{d}} \sum_{j=1}^{d} |a_j\rangle$. Then the weak value will be

$$\langle \hat{\Pi}^W_{a_j} \rangle^{b_0}_{\phi} \equiv \frac{\langle b_0|a_j\rangle\langle a_j|\phi_S\rangle}{\langle b_0|\phi_S\rangle} = \nu \langle a_j|\phi_S\rangle, \tag{5.2}$$

being $\nu = \langle b_0|a_j\rangle \,/\, \langle b_0|\phi_S\rangle = 1/\sum_{j=1}^{d} c_j$ a constant value. Since the weak value can be determined by measuring the pointer state, as described in Section 1.7, such result will be proportional to $\langle a_j|\phi_S\rangle \equiv c_j$. By scanning over j, hence changing the interacting Hamiltonian, we get all the elements c_j (the constant ν can be eliminated by normalizing the state).

As an example, I report the proof of principle described by Lundeen et al., 2011. The system state is the transverse spatial wavefunction of a photon

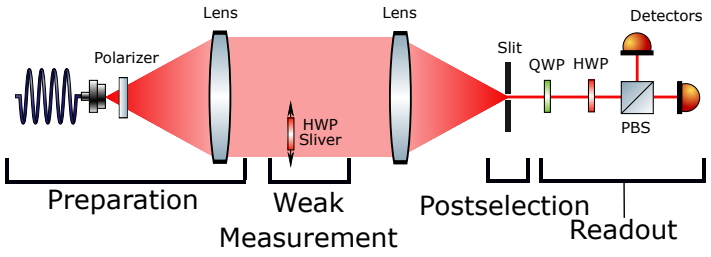

Figure 5.1: Scheme of the experiment by Lundeen et al., 2011 that implements the direct reconstruction of a pure state via weak measurements.

$\phi_S(x)$, while the pointer is encoded in its polarization degree of freedom. We choose the horizontal and vertical polarization as the computational basis. Then, we prepare many copies of the photon in the following initial state

$$|\psi\rangle = |\phi_S\rangle \otimes |0_A\rangle \tag{5.3}$$

and let them evolve through the unitary

$$\hat{U}(x_j) = e^{-i\theta\hat{\Pi}_{x_j}\otimes\hat{\sigma}_y} \approx \mathbb{1}_S \otimes \mathbb{1}_A - i\theta\hat{\Pi}_{x_j} \otimes \hat{\sigma}_y, \tag{5.4}$$

describing an interaction between the transverse spatial wavefunction and the polarization, parametrized by θ. In particular, $\hat{\Pi}_{x_j}$ is a projection onto the position x_j. Therefore, if the photon passes through position x_j, its polarization gets rotated of an angle θ. The approximation holds if θ is small. In practice, this is realized by placing in position x_j a HWP rotated of an angle $\theta/2$ as in Fig. 5.1. Clearly, a discretization of the theoretically infinite dimensional and continuous Hilbert space of transverse modes $\mathscr{H}_S$ is here implicit since the plate has a finite width and interacts with a range of positions that is necessarily larger than point-like. The interaction is changed by sliding the plate in d different position. As a result, we will obtain d samples which will be interpolated by the actual transverse spatial wavefunction.

The system state is post-selected onto the state

$$|b_0\rangle = |p_0\rangle \equiv \frac{1}{\sqrt{d}} \sum_{j=1}^{d} |x_j\rangle, \tag{5.5}$$

which is accomplished via a Fourier lens and a slit that blocks all photons except for those with momentum $p_x = 0$. Finally, the pointer state is described by the normalized vector

$$|F_{p_0,A}\rangle = \frac{\langle p_0|\hat{U}(x_j)|\psi\rangle}{\langle p_0|\phi_S\rangle} \approx |0_A\rangle + \theta\frac{\phi_S(x_j)}{\tilde{\phi}}|1_A\rangle \tag{5.6}$$

where the weak value appears as $\frac{\phi_S(x_j)}{\tilde{\phi}}$ and $\tilde{\phi} \equiv \sum_{j=1}^{d} \phi_S(x_j)$. By choosing the overall phase of ϕ_S so that $\tilde{\phi}$ is real and positive, one easily recognizes that

$$\begin{aligned} \Re(\phi_S(x_j)) &\approx \frac{\tilde{\phi}}{2\theta} \langle \hat{\sigma}_x^{(j)} \rangle_{F_{p_0,A}} \\ \Im(\phi_S(x_j)) &\approx \frac{\tilde{\phi}}{2\theta} \langle \hat{\sigma}_y^{(j)} \rangle_{F_{p_0,A}} \end{aligned} \tag{5.7}$$

After scanning the values of x_j, the factor $\frac{\tilde{\phi}}{2\theta}$ can be eliminated by normalization. One may devise an experimental setup in which the proportionality constant is known either a priori or with a limited number of additional measurements. That would make this technique able to find the single element $\phi_S(x_j)$, which can be advantageous if one is not interested in the value of the other elements.

Note that, provided that the necessary couplings can be implemented, this methods gives a universal recipe to measure any pure state with a fixed amount of measurements on the pointer, regardless of the dimension of the system's space.

5.1.2 *Direct Weak Reconstruction of the Density Operator*

Consider a density operator $\hat{\varrho}$, whose matrix elements are $\hat{\varrho}_{jk} \equiv \langle a_j|\hat{\varrho}|a_k\rangle$, being $\{|a_j\rangle \mid j = 1..d\}$ a orthonormal basis for the d-dimensional Hilbert space $\mathscr{H}_S$. If we define $\hat{\Pi}_{a_j a_k} \equiv \hat{\Pi}_{a_k} \hat{\Pi}_{b_0} \hat{\Pi}_{a_j}$, with $|b_0\rangle \equiv \frac{1}{\sqrt{d}} \sum_{j=1}^{d} |a_j\rangle$, it is easy to show that

$$\langle a_j|\hat{\varrho}|a_k\rangle = d \cdot \mathrm{Tr}(\hat{\Pi}_{a_j a_k} \hat{\varrho}). \tag{5.8}$$

The right-hand side of the above expression resembles the Born's rule for the mean value of the operator $\hat{\Pi}_{a_j a_k}$. However, since $\hat{\Pi}_{a_j a_k}$ is a product of non-commuting operators, it is not hermitian and hence is not an observable. In this sense, there is no set of projective measurements whose mean value is equivalent to $\mathrm{Tr}(\hat{\Pi}_{a_j a_k} \hat{\varrho})$.

The solution is to consider $\mathrm{Tr}(\hat{\Pi}_{a_j a_k} \hat{\varrho})$ as the weak average of the product $\hat{\Pi}_{a_k} \hat{\Pi}_{b_0} \hat{\Pi}_{a_j}$. This can be achieved by weakly coupling three different pointers (on $\mathscr{H}_A$, $\mathscr{H}_B$, $\mathscr{H}_C$) to the system's state and performing three *sequential* projections on them. It is sufficient to consider qubit pointers coupled via the operator $\hat{\sigma}_y$. The unitary interaction is parametrized by three real variables θ_A, θ_B, θ_C and reads:

$$\hat{U} = \hat{U}_C \hat{U}_B \hat{U}_{A,j} = e^{-i\theta_C \hat{\Pi}_{a_k} \otimes \hat{\sigma}_{yC}} e^{-i\theta_B \hat{\Pi}_{b_0} \otimes \hat{\sigma}_{yB}} e^{-i\theta_A \hat{\Pi}_{a_j} \otimes \hat{\sigma}_{yA}} \tag{5.9}$$

As demonstrated by Lundeen and Resch, 2005, the weak average of the products of operators is proportional to the mean value of the products of com-

muting operators acting on the pointer states. This has been extended by Foletto, 2017 to the case of qubit pointers, so that

$$\mathrm{Tr}(\hat{\Pi}_{a_j a_k}\hat{\varrho}) \approx \frac{1}{\theta_A\theta_B\theta_C}\langle\hat{\Sigma}_A\hat{\Sigma}_B\hat{\Sigma}_C\rangle_{F_{ABC}}, \tag{5.10}$$

being $\hat{\Sigma}_l \equiv \frac{\hat{\sigma}_{xl}+i\hat{\sigma}_{yl}}{2}$. Since each $\hat{\Sigma}_l$ acts on a different Hilbert space, the right-hand side of Eq. 5.10 reduces to the sum of mean value of sigma Pauli operators applied on the pointer states.

The above result requires the coupling to be weak so that the measurement on the first pointer does not affect the next one. For this reason, the last interaction may be strong, projecting the system's state on $|a_k\rangle$, instead of coupling it to a third pointer. Being the system post-selected at the end of the evolution, the matrix element is found through the weak value

$$\varrho_{jk} \equiv \langle a_j|\hat{\varrho}|a_k\rangle = d\mathrm{Tr}(\hat{\Pi}_{a_k}\hat{\varrho})\langle(\hat{\Pi}_{b_0}\hat{\Pi}_{a_j})^W\rangle_{\hat{\varrho}}^{a_k} \tag{5.11}$$

This fact makes any practical realization much simpler by reducing to 2 the number of needed ancillae and has been used in the first verification of this protocol Thekkadath et al., 2016, and in the experimental part of this work. From Eq. 5.11 it follows that

$$\begin{aligned}\Re(\varrho^W_{jk}) &= \mathcal{N}_{AB}\left(\langle\hat{\sigma}_{xA}\hat{\sigma}_{xB}\rangle_{j,k} - \langle\hat{\sigma}_{yA}\hat{\sigma}_{yB}\rangle_{j,k}\right)\\ \Im(\varrho^W_{jk}) &= \mathcal{N}_{AB}\left(\langle\hat{\sigma}_{yA}\hat{\sigma}_{xB}\rangle_{j,k} + \langle\hat{\sigma}_{xA}\hat{\sigma}_{yB}\rangle_{j,k}\right),\end{aligned} \tag{5.12}$$

where $\mathcal{N}_{AB} = \frac{d}{4\theta_A\theta_B}$. For consistency with most of the literature, in the above equations we do not explicitly mention the projector $\hat{\Pi}_{a_k} = |a_k\rangle\langle a_k|$; however, the symbol $\langle\hat{\sigma}_{xA}\hat{\sigma}_{yB}\rangle_{j,k}$ indicates the mean value of observable $\hat{\Pi}_{a_k}\otimes\hat{\sigma}_{xA}\otimes\hat{\sigma}_{yB}$ on the tripartite state after the evolution $\hat{U}_B\hat{U}_{A,j}$, namely

$$\langle\hat{\sigma}_{xA}\hat{\sigma}_{yB}\rangle_{j,k} = \mathrm{Tr}[\hat{\Pi}_{a_k}\otimes\hat{\sigma}_{xA}\otimes\hat{\sigma}_{yB}(\hat{U}_B\hat{U}_{A,j}\hat{\varrho}\hat{U}^\dagger_{A,j}\hat{U}^\dagger_B)]. \tag{5.13}$$

The state independent factor $\mathcal{N}_{AB}$ can be determined by knowing the values of $\theta_{A,B}$ or by normalizing ϱ^W (i.e. by determining its diagonal terms and dividing the matrix by its trace)

5.2 EXACT DIRECT MEASUREMENT OF THE WAVE FUNCTION

Recently Vallone and Dequal, 2016 showed that, in the case of pure states, the weak interaction is not needed for the purpose of state reconstruction, but actually represents a limitation. The pointer scheme is still necessary because it separates the interesting variables from those that are actually observed but the strength of the interaction can be set to an arbitrary value. Indeed, they found that the strongest interaction is the most convenient, since it minimize the inherently bias of the weak approach and allows to extract more information per measurement.

In the following sections, I will describe the main idea of the above results and I will show how to extended it to the case of density operator.

5.2.1 *Exact Direct Reconstruction of Pure States*

To introduce the idea of this work, let's start with the extension of the most fundamental of Lundeen's protocols (Section 5.1.1). Consider again the example of the transverse spatial wavefunction of a photon, coupled to its polarization. The interacting Hamiltonian is still $H_{\text{int}} = \theta \hat{\Pi}_{x_j} \otimes \hat{\sigma}_y$, with $\hat{\Pi}_{x_j} = |x_j\rangle \langle x_j|$ the projector onto the position x_j. The unitary evolution can be easily calculated in its exact form:

$$\hat{U}(x_j) = e^{-i\theta \hat{\Pi}_{x_j} \otimes \hat{\sigma}_y} = (\mathbb{1}_S - \hat{\Pi}_{x_j}) \otimes \mathbb{1}_A + \hat{\Pi}_{x_j} \otimes e^{-i\theta \hat{\sigma}_y}. \tag{5.14}$$

The above equation now holds for any θ, taking the values in $]0,\ \pi/2]$. The evolution is still a rotation in the polarization of the photon whenever it is found in position x_j, while no interaction occurs in the other positions. Here $\theta = 0$ means no interaction at all, whereas $\theta = \pi/2$ implies a rotation of the polarization to its orthogonal state (maximum strength).

The system's state is then post-selected into $|p_0\rangle$, so that the final normalized state becomes

$$\begin{aligned} |F_{p_0,A}\rangle =& \frac{\langle p_0|\hat{U}(x_j)|\psi\rangle}{\langle p_0|\phi_S\rangle}, \\ =& \left(1 + (\cos(\theta) - 1)\frac{\phi_S(x_j)}{\tilde{\phi}}\right)|0_A\rangle + \sin(\theta)\frac{\phi_S(x_j)}{\tilde{\phi}}|1_A\rangle . \end{aligned} \tag{5.15}$$

Note that, although the coupling is strong, the weak value $\frac{\phi_S(x_j)}{\tilde{\phi}}$ formally appears again here. Finally, projective measurements are carried out on the pointer to find that

$$\begin{aligned} \Re(\phi_S(x_j)) &= \frac{\tilde{\phi}}{2\sin(\theta)}\left(\langle \hat{\sigma}_x^{(a_j)} \rangle_{F_{p_0,A}} + 2\tan\left(\frac{\theta}{2}\right)\langle \hat{\Pi}_1^{(a_j)} \rangle_{F_{p_0,A}}\right) \\ \Im(\phi_S(x_j)) &= \frac{\tilde{\phi}}{2\sin(\theta)}\langle \hat{\sigma}_y^{(a_j)} \rangle_{F_{p_0,A}} \end{aligned} \tag{5.16}$$

The resemblance to (5.7) is remarkable. However, one additional pointer measurement is needed, that of $\hat{\Pi}_1$, where $|1_A\rangle$ is defined as the orthogonal state of the initial $|0_A\rangle$. The entire cost of strong couplings is in this single further step. Again, if one knows the normalization factor $\frac{\tilde{\phi}}{2\sin(\theta)}$, they can extract each coordinate of the state vector in a fixed number of measurements regardless of the dimension of the object Hilbert Space.

5.2.2 *Exact Reconstruction of the Density Operator*

The generalization of the previous result can be extended to the case of the density operator by applying the result of Eq. 5.14 in the framework of Section 5.1.2.

Let the initial object system be prepared in state $\hat{\varrho}_S$ of unknown matrix elements $\varrho_{jk} = \langle a_j|\hat{\varrho}_S|a_k\rangle$, with $\{|a_j\rangle \mid j = 1..d\}$ being an orthornormal basis for the Hilbert space $\mathscr{H}_S$. Two qubit pointers, defined in the Hilbert spaces $\mathscr{H}_A$ and $\mathscr{H}_B$ respectively, are prepared in pure states $\hat{\varrho}_A = |0_A\rangle\langle 0_A|$ and $\hat{\varrho}_B = |0_B\rangle\langle 0_B|$, so that in the total initial state is described by the separable tensor product

$$\hat{\varrho}_{tot} = \hat{\varrho}_S \otimes \hat{\varrho}_A \otimes \hat{\varrho}_B \tag{5.17}$$

Suppose we want to measure the matrix element ϱ_{jk}. Therefore, the first interaction between the system and pointer $\hat{\varrho}_A$ will be given by the unitary

$$\hat{U}_A(a_j) \otimes \mathbb{1}_B = e^{-i\theta_A \hat{\Pi}_{a_j} \otimes \hat{\sigma}_{yA}} \otimes \mathbb{1}_B. \tag{5.18}$$

Afterwards, a second coupling involves the pointer $\hat{\varrho}_B$. In particular, given the projector $\hat{\Pi}_{b_0}$, with $|b_0\rangle \equiv \frac{1}{\sqrt{d}}\sum_{j=1}^{d}|a_j\rangle$ as usual, the unitary reads

$$\hat{U}_B \otimes \mathbb{1}_A = e^{-i\theta_B \hat{\Pi}_{b_0} \otimes \hat{\sigma}_{yB}} \otimes \mathbb{1}_A. \tag{5.19}$$

After both interactions, the total system is in a state described by:

$$\hat{\varrho}'_{tot}(a_j) = \hat{U}_B \hat{U}_A(a_j) \hat{\varrho}_{tot} \hat{U}_A^\dagger(a_j) \hat{U}_B^\dagger \tag{5.20}$$

Subsequently, we post-select the system's state on $|a_k\rangle$, leaving the pointers in a state that we call $\hat{\varrho}_{AB}$.

It is useful to define the following for the calculation of the final state (From now on I will use symbols $c_{A,B}$, $s_{A,B}$ and $t_{A,B}$ in place of $\cos(\theta_{A.B})$, $\sin(\theta_{A,B})$ and $\tan\left(\frac{\theta_{A,B}}{2}\right)$, for the ease of notation):

$$\begin{aligned}
\hat{\alpha}_0 &\equiv \mathbb{1} + (c_A - 1)\hat{\Pi}_{a_j} \\
\hat{\alpha}_1 &\equiv s_A \hat{\Pi}_{a_j} \\
\hat{\beta}_0 &\equiv \mathbb{1} + (c_B - 1)\hat{\Pi}_{b_0} \\
\hat{\beta}_1 &\equiv s_B \hat{\Pi}_{b_0},
\end{aligned} \tag{5.21}$$

with which we can rewrite the unitaries as

$$\hat{U}_A(a_j) = \sum_{n=0}^{1} (-i)^n \hat{\alpha}_n \hat{\sigma}_{yA}^n \qquad \hat{U}_B = \sum_{m=0}^{1} (-i)^m \hat{\beta}_m \hat{\sigma}_{yB}^m. \tag{5.22}$$

Before the post-selection the total state is

$$\begin{aligned}
\hat{\varrho}'_{tot}(a_j) &\equiv \hat{U}_B \hat{U}_A(a_j) \hat{\varrho} \hat{U}_A^\dagger(a_j) \hat{U}_B^\dagger \\
&= \sum_{n,n',m,m'} i^{n'+m'-n-m} \hat{\beta}_m \hat{\alpha}_n \hat{\varrho}_S \hat{\alpha}_{n'} \hat{\beta}'_m \otimes \hat{\sigma}_{yA}^n |0_A\rangle\langle 0_A| \hat{\sigma}_{yA}^{n'} \otimes \hat{\sigma}_{yB}^m |0_B\rangle\langle 0_B| \hat{\sigma}_{yB}^{m'}
\end{aligned}$$

(5.23)

and after the system's state projection on $|a_k\rangle$ we have

$$|a_k\rangle\langle a_k| \otimes \langle a_k|\hat{\varrho}'_{tot}(a_j)|a_k\rangle = |a_k\rangle\langle a_k| \otimes \frac{1}{4}\sum_{\mu,\nu=0}^{3} r^{(jk)}_{\mu\nu} \cdot \hat{\sigma}_{\mu A} \otimes \hat{\sigma}_{\nu B} \tag{5.24}$$

where $\hat{\sigma}_0 = \mathbb{1}$, $\hat{\sigma}_1 = \hat{\sigma}_x$, $\hat{\sigma}_2 = \hat{\sigma}_y$, $\hat{\sigma}_3 = \hat{\sigma}_z$ and

$$\begin{aligned} r^{(jk)}_{\mu\nu} &\equiv \mathrm{Tr}(\langle a_k|\hat{\varrho}'_{tot}(a_j)|a_k\rangle \otimes \hat{\sigma}_{\mu A} \otimes \hat{\sigma}_{\nu B}) \\ &= \sum_{n,n',m,m'} i^{n'+m'-n-m'} \langle a_k|\hat{\beta}_m\hat{\alpha}_n\hat{\varrho}_S\hat{\alpha}_{n'}\hat{\beta}_{m'}|a_k\rangle \cdot \langle 0_A|\hat{\sigma}^{n'}_{yA}\hat{\sigma}_{\mu A}\hat{\sigma}^{n}_{yA}|0_A\rangle \cdot \langle 0_B|\hat{\sigma}^{m'}_{yB}\hat{\sigma}_{\nu B}\hat{\sigma}^{m}_{yB}|0_B\rangle \\ &= \sum_{n,n',m,m'} i^{n'+m'-n-m'} \langle a_k|\hat{\beta}_m\hat{\alpha}_n\hat{\varrho}_S\hat{\alpha}_{n'}\hat{\beta}_{m'}|a_k\rangle \cdot G^{\mu}_{n,n'}G^{\nu}_{m,m'} \end{aligned} \tag{5.25}$$

in which

$$G^{\mu}_{n,n'} \equiv \delta_{\mu,0}\delta_{n,n'} + \delta_{\mu,1}i^{2n-1}\delta_{n,1-n'} + \delta_{\mu,2}\delta_{n,1-n'} + \delta_{\mu,3}(-1)^n\delta_{n,n'} \tag{5.26}$$

We can then define:

$$\hat{A}_\mu \equiv \sum_{n,n'} i^{n'-n}\hat{\alpha}_n\hat{\varrho}_S\hat{\alpha}_{n'}G^{\mu}_{n,n'} \tag{5.27}$$

so that

$$\begin{aligned} \hat{A}_0 &= \hat{A}_0^\dagger = \hat{\alpha}_0\hat{\varrho}_S\hat{\alpha}_0 + \hat{\alpha}_1\hat{\varrho}_S\hat{\alpha}_1 = \hat{\varrho}_S + (c_A - 1)(\hat{\Pi}_{a_1}\hat{\varrho}_S + \hat{\varrho}_S\hat{\Pi}_{a_1} - 2\hat{\Pi}_{a_1}\hat{\varrho}_S\hat{\Pi}_{a_1}) \\ \hat{A}_1 &= \hat{A}_1^\dagger = \hat{\alpha}_0\hat{\varrho}_S\hat{\alpha}_1 + \hat{\alpha}_1\hat{\varrho}_S\hat{\alpha}_0 = s_A\left(\hat{\varrho}_S\hat{\Pi}_{a_1} + \hat{\Pi}_{a_1}\hat{\varrho}_S + 2(c_A - 1)\hat{\Pi}_{a_1}\hat{\varrho}_S\hat{\Pi}_{a_1}\right) \\ \hat{A}_2 &= \hat{A}_2^\dagger = i(\hat{\alpha}_0\hat{\varrho}_S\hat{\alpha}_1 - \hat{\alpha}_1\hat{\varrho}_S\hat{\alpha}_0) = is_A\left(\hat{\varrho}_S\hat{\Pi}_{a_1} - \hat{\Pi}_{a_1}\hat{\varrho}_S\right) \\ \hat{A}_3 &= \hat{A}_3^\dagger = \hat{\alpha}_0\hat{\varrho}_S\hat{\alpha}_0 - \hat{\alpha}_1\hat{\varrho}_S\hat{\alpha}_1 = \hat{\varrho}_S + (c_A - 1)(\hat{\Pi}_{a_1}\hat{\varrho}_S + \hat{\varrho}_S\hat{\Pi}_{a_1} + 2c_A\hat{\Pi}_{a_1}\hat{\varrho}_S\hat{\Pi}_{a_1}) \end{aligned} \tag{5.28}$$

Then (5.25) becomes

$$r^{(jk)}_{\mu\nu} = \sum_{m,m'} i^{m'-m}\langle a_k|\hat{\beta}_m\hat{A}_\mu\hat{\beta}_{m'}|a_k\rangle \cdot G^{\nu}_{m,m'} \tag{5.29}$$

In particular, considering that

$$\hat{\beta}_0|a_k\rangle = |a_k\rangle + \frac{c_B - 1}{d}\sum_{l=1}^{d}|a_l\rangle \qquad \hat{\beta}_1|a_k\rangle = \frac{s_B}{d}\sum_{l=1}^{d}|a_l\rangle \tag{5.30}$$

one can write:

$$\begin{aligned}
r^{(jk)}_{\mu 0} &= \langle a_k|\hat{\beta}_0\hat{A}_\mu\hat{\beta}_0|a_k\rangle + \langle a_k|\hat{\beta}_1\hat{A}_\mu\hat{\beta}_1|a_k\rangle \\
&= \langle a_k|\hat{A}_\mu|a_k\rangle + \frac{2(c_B-1)}{d}\left(\sum_l \Re(\langle a_k|\hat{A}_\mu|a_l\rangle) - \frac{1}{d}\sum_{l,l'}\langle a_{l'}|\hat{A}_\mu|a_l\rangle\right) \\
r^{(jk)}_{\mu 1} &= \langle a_k|\hat{\beta}_0\hat{A}_\mu\hat{\beta}_1|a_k\rangle + \langle a_k|\hat{\beta}_1\hat{A}_\mu\hat{\beta}_0|a_k\rangle \\
&= \frac{2s_B}{d}\left(\sum_l \Re(\langle a_k|\hat{A}_\mu|a_l\rangle) + \frac{c_B-1}{d}\sum_{l,l'}\langle a_{l'}|\hat{A}_\mu|a_l\rangle\right) \\
r^{(jk)}_{\mu 2} &= i\langle a_k|\hat{\beta}_0\hat{A}_\mu\hat{\beta}_1|a_k\rangle - i\langle a_k|\hat{\beta}_1\hat{A}_\mu\hat{\beta}_0|a_k\rangle \\
&= -\frac{2s_B}{d}\sum_l \Im(\langle a_k|\hat{A}_\mu|a_l\rangle) \\
r^{(jk)}_{\mu 3} &= \langle a_k|\hat{\beta}_0\hat{A}_\mu\hat{\beta}_0|a_k\rangle - \langle a_k|\hat{\beta}_1\hat{A}_\mu\hat{\beta}_1|a_k\rangle \\
&= \langle a_k|\hat{A}_\mu|a_k\rangle + \frac{2(c_B-1)}{d}\left(\sum_l \Re(\langle a_k|\hat{A}_\mu|a_l\rangle) + \frac{c_B}{d}\sum_{l,l'}\langle a_{l'}|\hat{A}_\mu|a_l\rangle\right)
\end{aligned} \tag{5.31}$$

Then it is possible to evaluate

$$\begin{aligned}
\langle a'_l|\hat{A}_0|a_l\rangle &= \varrho_{ll'} + (c_A-1)(\delta_{jl'}\varrho_{jl} + \delta_{jl}\varrho_{l'j} - 2\delta_{jl'}\delta_{jl}\varrho_{jj}) \\
\langle a'_l|\hat{A}_1|a_l\rangle &= s_A\left(\delta_{jl}\varrho_{l'j} + \delta_{jl'}\varrho_{jl} + 2(c_A-1)\delta_{jl'}\delta_{jl}\varrho_{jj}\right) \\
\langle a'_l|\hat{A}_2|a_l\rangle &= is_A\left(\delta_{jl}\varrho_{l'j} - \delta_{jl'}\varrho_{jl}\right) \\
\langle a'_l|\hat{A}_3|a_l\rangle &= \varrho_{l'l} + (c_A-1)(\delta_{jl'}\varrho_{jl} + \delta_{jl'}\varrho_{l'j} + 2c_A\delta_{jl'}\delta_{jl}\varrho_{jj})
\end{aligned} \tag{5.32}$$

Considering that $r^{(jk)}_{\mu\nu} = \mathrm{Tr}(\langle a_k|\hat{\varrho}'_{tot}(a_j)|a_k\rangle \otimes \hat{\sigma}^{(a_j)}_{\mu A} \otimes \hat{\sigma}^{(b_0)}_{\nu B}) = \mathrm{Tr}(\hat{\Pi}_{a_k}\hat{\varrho}_S)\langle \hat{\sigma}^{(a_j)}_{\mu A}\hat{\sigma}^{(b_0)}_{\nu B}\rangle_{F_{a_k,AB}}$, one finds:

$$\begin{aligned}
\langle \hat{\Pi}^{(a_j)}_{1A}\hat{\Pi}^{(b_0)}_{1B}\rangle_{F_{a_k,AB}}\mathrm{Tr}(\hat{\Pi}_{a_k}\hat{\varrho}_S) &= r^{(jk)}_{00} - r^{(jk)}_{30} - r^{(jk)}_{03} + r^{(jk)}_{33} = \frac{s_A^2 s_B^2}{d^2}\varrho_{jj} && \forall k \\
\langle \hat{\sigma}^{(a_j)}_{yA}\hat{\sigma}^{(b_0)}_{yB}\rangle_{F_{a_k,AB}}\mathrm{Tr}(\hat{\Pi}_{a_k}\hat{\varrho}_S) &= r^{(jk)}_{22} = -\frac{2s_A s_B}{d}\Re(\varrho_{jk}) && j \neq k \\
\langle \hat{\sigma}^{(a_j)}_{xA}\hat{\sigma}^{(b_0)}_{yB}\rangle_{F_{a_k,AB}}\mathrm{Tr}(\hat{\Pi}_{a_k}\hat{\varrho}_S) &= r^{(jk)}_{12} = \frac{2s_A s_B}{d}\Im(\varrho_{jk}) && j \neq k
\end{aligned} \tag{5.33}$$

That can be recast into

$$\begin{aligned}
\varrho^{II}_{jj} &= 16\mathcal{N}^2_{AB}\langle \hat{\Pi}_{1A}\hat{\Pi}_{1B}\rangle_{j,k} && \forall k \\
\Re(\varrho^{II}_{jk}) &= -2\mathcal{N}_{AB}\langle \hat{\sigma}_{yA}\hat{\sigma}_{yB}\rangle_{j,k} && j \neq k \\
\Im(\varrho^{II}_{jk}) &= 2\mathcal{N}_{AB}\langle \hat{\sigma}_{xA}\hat{\sigma}_{yB}\rangle_{j,k} && j \neq k
\end{aligned} \tag{5.34}$$

where $\hat{\Pi}_1 = |1\rangle\langle 1| = (1-\sigma_z)/2$ is the projector on the -1 eingenstate of σ_z.

Another form akin to the Lundeen's formulas of Eq. 5.12 can be found, considering the following

$$\begin{aligned}
\langle \hat{\Pi}_{1A}^{(a_j)} \hat{\sigma}_{xB}^{(b_0)} \rangle_{F_{a_k,AB}} \mathrm{Tr}(\hat{\Pi}_{a_k} \hat{\varrho}_S) &= r_{01}^{(jk)} - r_{31}^{(jk)} = \delta_{jk} \frac{2 s_A^2 s_B}{d} \varrho_{jk} + \frac{2 s_A^2 s_B (c_B - 1)}{d^2} \varrho_{jj} \\
\langle \hat{\sigma}_{xA}^{(a_j)} \hat{\Pi}_{1B}^{(b_0)} \rangle_{F_{a_k,AB}} \mathrm{Tr}(\hat{\Pi}_{a_k} \hat{\varrho}_S) &= r_{10}^{(jk)} - r_{13}^{(jk)} = \frac{2 s_A s_B^2}{d^2} \sum_l \Re(\varrho_{jl}) + \frac{2 s_A s_B^2 (c_A - 1)}{d^2} \varrho_{jj} \\
\langle \hat{\sigma}_{yA}^{(a_j)} \hat{\Pi}_{1B}^{(b_0)} \rangle_{F_{a_k,AB}} \mathrm{Tr}(\hat{\Pi}_{a_k} \hat{\varrho}_S) &= r_{20}^{(jk)} - r_{23}^{(jk)} = \frac{2 s_A s_B^2}{d^2} \sum_l \Im(\varrho_{jl})
\end{aligned} \tag{5.35}$$

that can be recast into

$$\begin{aligned}
\Re(\varrho_{jk}^I) =& \Re(\varrho_{jk}^W) + 2\mathcal{N}_{AB} (t_B \langle \hat{\sigma}_{xA} \hat{\Pi}_{1B} \rangle_{j,k} \\
&+ t_A \langle \hat{\Pi}_{1A} \hat{\sigma}_{xB} \rangle_{j,k} + 2 t_A t_B \langle \hat{\Pi}_{1A} \hat{\Pi}_{1B} \rangle_{j,k}) \\
\Im(\varrho_{jk}^I) =& \Im(\varrho_{jk}^W) + 2\mathcal{N}_{AB} t_B \langle \hat{\sigma}_{yA} \hat{\Pi}_{1B} \rangle_{j,k}.
\end{aligned} \tag{5.36}$$

Eq. 5.36 represents the direct generalization of the reconstructing method through weak measurement (Eq. 5.12). It needs more measurements than the weak counterpart (8 compared to 4 correlations should be measured for each element ϱ_{jk}), but the increased complexity is compensated by a better estimation of the density matrix. Nonetheless, a simpler expression requiring even fewer measurements is given by Eq. 5.34. Although Eqs. 5.12, 5.36 and 5.34 are valid in general for $\theta_A \neq \theta_B$, from now on we will only consider the case $\theta_A = \theta_B = \theta$ for simplicity.

The fundamental advantage of the two latter schemes is that they are accurate for any value of θ. Consequently, there is no need to tune the strength into the range of the weak approximation and it is possible to use more practical strong measurements, which are more akin to standard quantum projections and less prone to statistical errors. Indeed, inverting the above relations shows that the experimental data are proportional to $\sin^2\theta$ (except for the diagonal elements in Eq. 5.34, for which the factor is $\sin^4\theta$) that greatly weakens the signal when θ is small, making statistical errors more relevant.

We can evaluate the *mean square statistical error* $\delta\varrho$ by summing the absolute squares of the standard deviations on all the elements ϱ_{jk}:

$$\delta\varrho = \sqrt{\sum_{j,k} |\delta\varrho_{jk}|^2}\,. \tag{5.37}$$

If N labels the number of events used to measure each correlation term in (5.12) (or (5.36) and (5.34)), we find that in the weak approximation $\delta\varrho$ has a lower bound:

$$\delta\varrho \geq \frac{\alpha(d)}{\theta^2\sqrt{N}} \tag{5.38}$$

where $\alpha(d) = \frac{(d-1)\sqrt{d}}{2\sqrt{2}}$ for the protocols of Eqs. (5.12) and (5.36) and $\alpha(d) = \frac{\sqrt{d(d-1)(d-4)}}{2}$ for Eq. (5.34). The factor $1/\theta^2$ highlights that the weaker the coupling is, the greater the statistical errors become. The above equation was derived under the assumption of reconstructing the entire matrix, taking its hermitian part and normalizing it at the end of the procedure.

Weak measurements are also more vulnerable to some experimental systematic biases. Indeed, terms like $\langle \hat{\sigma}_{xA}\hat{\sigma}_{yB}\rangle_{j,k}$ are obtained from linear combinations of four contributions, each of them representing one projector that appears in the spectral decomposition of the Pauli operators. A small proportional bias in one of them becomes relevant when such linear combinations are also bound to be small by factor $\sin^2\theta$.

To summarize, our protocol breaks the aforementioned trade-off of weak measurements. Our proposed methods work with no approximation in the strong measurement regime, which allows more precise and accurate results. Moreover, the method of (5.34) needs fewer measurements than its weak counterpart (three different pointer operators, $\hat{\sigma}_{xA}\hat{\sigma}_{yB}$, $\hat{\sigma}_{yA}\hat{\sigma}_{yB}$, $\hat{\Pi}_{1A}\hat{\Pi}_{1B}$, instead of four).

5.3 EXPERIMENTAL IMPLEMENTATION

With the purpose of experimentally comparing the state reconstruction methods, we have devised an optical setup that could easily switch between the different techniques. In particular, we compare the reconstruction of the polarization of a single photon. Of course, the fact that the system Hilbert space is only bidimensional puts our measurement schemes at a disadvantage compared with the standard QST, which can reconstruct any polarization density operator with only $d^2 = 4$ data points. However, this experiment has to be interpreted as a *proof of concept*, the goal of which is to show that direct reconstruction can be performed using strong measurements with improved results compared to those obtained in the weak case.

5.3.1 *Setup*

The state preparation is as follows. We produce polarization-entangled photon pairs by pumping laser light at 404.5 nm on a 30 mm periodically poled KTP crystal in a polarization-based Sagnac interferometer (see Appendix A for more details). Down-converted photons at 809 nm are collected into two single-mode fibers. One photon of the pair is used to herald the presence of the other and is detected by a single photon avalanche detector (SPAD). The other photon is sent to the measurement apparatus, which reconstructs its polarization state. With this source we can tailor the purity of the measured qubit, preparing also mixed states. Indeed, by properly adjusting the linear polarization of the pump (acting on the HWP before the Sagnac interferome-

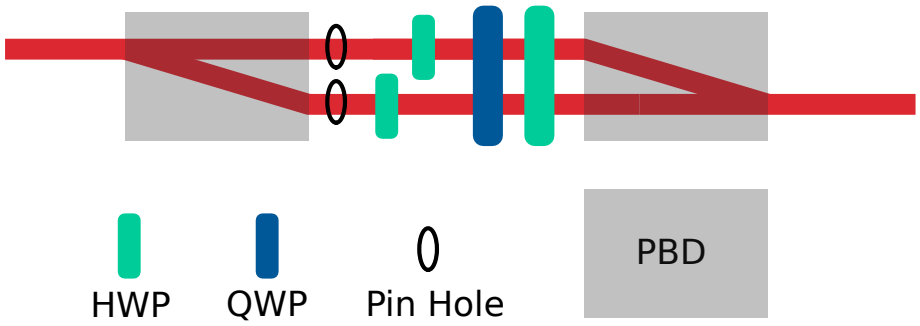

Figure 5.2: Scheme of the Mach-Zehnder interferometer implementing the interaction between system and pointer and the measurement on the pointer.

ter) we change the amount of entanglement between the photon-pairs. With a maximally entangled state, the measured qubit will be maximally mixed. On the contrary, with a separable state we can prepare a pure state.

The building block for the pointer preparation, interaction and measurement is implemented via a Mach-Zehnder interferometer (see Fig. 5.2). Two Polarized Beam Displacer (PBD) correspond to the input and output ports. These employ birefringent calcite crystals to separate light into two parallel beams at a distance of approximately (4.1 ± 0.1) mm at the operating wavelength of 809 nm. The resulting state after the first PBD is an entangled state in the polarization and path degrees of freedom. This allows us to swap the encoding of the system from the polarization to the interferometer path. Since the pointer has to be projected on several orthonormal bases, we find convenient to encode it on the polarization degree of freedom within the interferometer, so that the measurement can be easily setup using a QWP and a HWP before the closing PBD.

The interaction between the system and the pointer is such that if the state is in the eigenstate of the projector $1 - \hat{\Pi}$, the pointer does not change its state, otherwise the unitary $e^{-i\theta\sigma_y}$ applies on it (see Eq. 5.22). This operator corresponds to a rotation on the linear polarization, that we implement via a rotated HWP acting only on the right arm of the interferometer. The angle between its fast axis and the horizontal plane is $\alpha = \theta/2$. Another HWP is placed on the other arm to compensate the optical path difference, but rotated in order to not change the polarization.

Finally, the measurement on the pointer state of σ_x and σ_y is performed using a QWP and a HWP, whereas the measurement of σ_z is done by blocking alternatively one arm of the interferometer. Each configuration of these plates and of the shutters corresponds to a particular pointer projector that appears in the spectral decomposition of one Pauli operator. After the second PBD, which is oriented like the first one, we placed an HWP with axis at 45 degrees relative to the horizontal plane. Only one of the two exit paths is considered, so that the output polarization is the result of the collapse of the system after

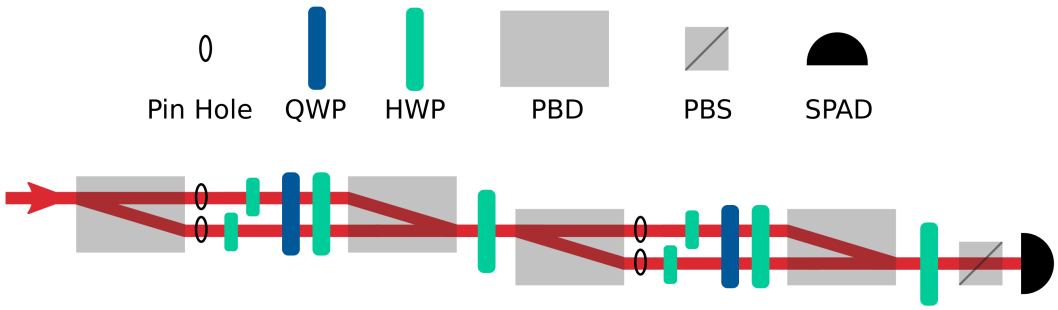

Figure 5.3: Scheme of the entire measurement system.

a successful pointer projection identified by the orientation of the internal plates.

The whole measurement apparatus consists of two interferometer in cascade implementing the unitaries $U_{A,j}$ and U_B (see Fig. 5.3). We choose the horizontal and vertical polarization states as the orthonormal basis for the state representation. That is $|a_0\rangle = |H\rangle$ and $|a_1\rangle = |V\rangle$. Therefore, the first interferometer, implementing the unitary $U_{A,j}$, is such that the two arms spatially separate the horizontal and vertical polarization component of the system. Instead, the second interferometer separates the diagonal and anti-diagonal states, since $|b_0\rangle = |D\rangle$. This is done by adding two HWPs, rotated of $22,5$ degrees, before and after the interferometer. Postselection on $|a_k\rangle \in \{|H\rangle, |V\rangle\}$ is carried out on the system state using a HWP and a PBS. Photons are detected by a SPAD.

To perform the standard QST, we add, at the beginning of the measurement, a QWP and a HWP just before the first interferometer. The first PBD is then used as a polarizer to project the system state.

5.3.2 *Calibration and alignment*

The alignment of the source is not repeated in this section as it has been described in Section 4.4.2. Regarding the measurement apparatus, the alignment consist in calibrating the angle of the wave plates' fast axes and aligning the two interferometers. The former is easily done, with the wave plate in place, by preparing a known linear polarized state placed before the plate and measuring the orthogonal one after it. By rotating the wave plate we minimize the count rate of the detected photons, such that the plate's axis is aligned with the incoming polarization. The angle is then measured either by a goniometer reported on the mount (for manual rotators) or registerd by an encoder (for motorized rotation mounts).

Regarding the interferometers, the overlap of the two paths is straightforward to setup since the only degree of freedom is the relative orientation of the opening and closing PBD. Being identical, a very good overlap is found

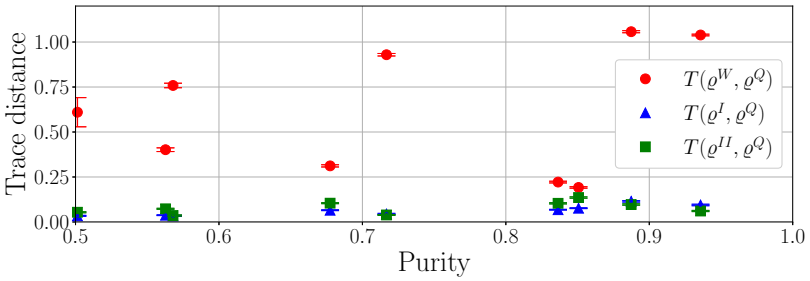

Figure 5.4: Trace distance between reconstructed states and reference states for different input purity: $T(\varrho^W, \varrho^Q)$ (circles), $T(\varrho^I, \varrho^Q)$ (triangles), $T(\varrho^{II}, \varrho^Q)$ (squares).

just by putting them one in front of the other. The fine adjustment requires a small change on the tilt angle that modifies the optical path difference of the two arms. Since the coherence length of the produced photons is relatively small we set the angle such that the maximum visibility of the interference is reached, which we found higher than 98% for both interferometers. In particular, this is done by injecting a diagonal state into the interferometer, setting all the plates inside such that the axis is horizontal, other than the last one, which have to be at 45 degrees, and measuring the anti-diagonal state at the output. In this configuration, the vertical and horizontal components are spatially separated, thus going through different optical paths. Thus, a phase is introduced between the two components whose effect is measured. Indeed with a non-null phase the photon have a probability different from zero to be projected on the anti-diagonal state and being detected. Therefore, the tilt angle is set to a minimum of the interference pattern, corresponding to the maximum visibility.

5.3.3 *Analysis and results*

The main experiment consisted of two phases: the first was aimed at verifying the validity of our protocols at full strength, whereas the second focused on the role of the coupling strength. In both cases we tested all the methods at our disposal ((5.12), (5.36) and (5.34)) using as a figure of merit the trace distance between each reconstructed state and ϱ^Q, which is used as a fixed reference for all values of the coupling strength. For a fair comparison we kept the reconstructed states as raw as possible by taking their hermitian part and normalizing the trace, but without applying any further post-processing such as a maximum likelihood estimation James et al., 2001. We underline that these techniques, aimed at ensuring the positivity of the final matrices, could be applied to both direct reconstruction and QST.

In the first phase, we generated nine states of different degrees of purity, measured as $\mathrm{Tr}[(\varrho^Q)^2]$. We were able to produce a state very close to being

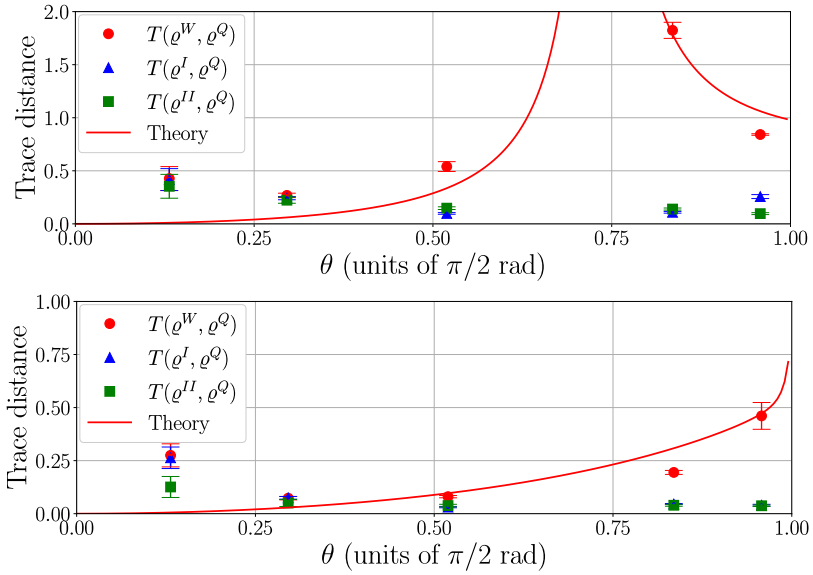

Figure 5.5: Trace distance between reconstructed states and reference state, for input states: $|D\rangle$ **(Top)** and maximally mixed **(Bottom)**. The solid line represents the theoretical trace distance between the expected value of ϱ^W and the experimental ϱ^Q.

completely mixed, indeed its purity is 0.501 ± 0.003. The maximum purity we observed is only 0.936 ± 0.006, due to the fact that the pump light entering in the Sagnac interferometer was not perfectly linearly polarized. Moreover, imperfections in the PBS caused imbalanced extinction ratios in the two arms.

We measured each of the state, setting the maximum strength in the measurement apparatus and then applying the three reconstructing equations. The dots of Fig. 5.4 report the trace distance between the measured reconstructed states and the reference state: $T(\varrho^W, \varrho^Q)$ (circles), $T(\varrho^I, \varrho^Q)$ (triangles), $T(\varrho^{II}, \varrho^Q)$ (squares). As expected, the results given by the method of Eq. (5.12) are inaccurate, since the high value of strength invalidates the weak approximation. There is no direct relation between purity and these errors, which are rather influenced by the particular input states. Instead, our two protocols show a lower trace distance in the entire range of purity, confirming the validity of our proposals for both mixed and almost pure states.

In the second phase of the experiment we varied the coupling strength and focused only on two fixed input states. The results are shown in Fig. 5.5 with the two prepared states being $|D\rangle$ **(Top)** and the maximally mixed one **(Bottom)**. The solid lines display the expected trace distance for the calculated state ϱ^W of Eq. (5.12) using the experimental ϱ^Q as an estimate of ϱ_S. Again, they show how the weak approach reconstructs states that diverge from the correct ones as the strength increases. In the strong regime, these curves well reproduce the measured data $T(\varrho^W, \varrho^Q)$, but we see larger trace distances than expected for weak coupling. This is probably due to the aforementioned greater vulnerability to small inaccuracies in the pointer projections, which

only become relevant at low values of θ. The protocol of Eq. (5.36) is similarly affected, because $\varrho^I \approx \varrho^W$ for small strength as the higher order corrective terms become negligible. These biases have the same effect in the extraction of non-diagonal elements of Eq. (5.34), but terms like $\langle \hat{\Pi}_{1A} \hat{\Pi}_{1B} \rangle_{j,k}$ in the diagonal ones are a source of errors too. Indeed, the corresponding photon counts are weakened by factor $\sin^4 \theta$ which is extremely small for low strength. Errors in the experimental realization of the projector or miscalculations of θ can cause the diagonal matrix elements to be much greater than expected and the subsequent normalization of the trace can render the non-diagonal ones close to zero. This explains the high trace distance in Fig. 5.5 **(Top)** for $\varrho_S = |D\rangle \langle D|$ (for which the non-diagonal elements are 0.5) and the slightly lower one in Fig. 5.5 **(Bottom)** for the maximally mixed state (which has null non-diagonal elements).

However, Fig. 5.5 also shows how ϱ^I and ϱ^{II} become compatible with the reference state for large values of strength, confirming the correctness of these approaches. It is also clear that the weak measurement proposal is not accurate even at very small θ due to the high sensitivity to imperfections and systematic errors. Our method presents similar features at low θ, but drastically improves the performance at large θ.

We also evaluated the mean square statistical error $\delta\varrho$ given in Eq. (5.37) associated to the reconstructed matrices, which can be seen in Fig. 5.6. The lines display the theoretical expectation values of these errors, evaluated with the total number of events $N \approx 8 \cdot 10^3$ and $N \approx 4 \cdot 10^4$ used in the experiments (respectively for the **(Top)** and **(Bottom)** figures). Our results closely follow such curves and further prove that the errors dramatically increase for small values of θ. The lower trace distances and statistical errors in the right side of Figs. 5.5 and 5.6 clearly demonstrate the superiority of our strong measurement method with respect to the weak counterparts. Increasing the value of θ, as allowed by the method proposed here, has a double advantage: it reduces the statistical errors and makes the protocol more robust against imperfections.

5.4 DISCUSSION

We have proposed a new scheme to directly reconstruct the density matrix that extends the existing idea based on weak measurement, making it exact for any value of the coupling strength with the pointers. In particular, we have shown that the use of strong measurements makes our protocol less vulnerable to experimental statistical and systematic errors in comparison to the original proposal (Thekkadath et al., 2016), while the lack of approximations in our expressions makes the results devoid of any inherent biases. In particular, our method uses the same resources and experimental operations of the weak counterpart, but achieves much better performance.

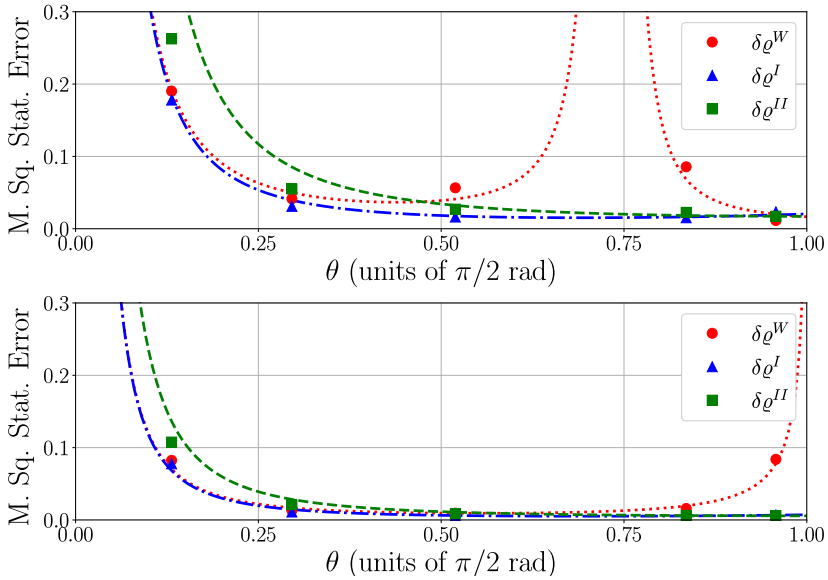

Figure 5.6: Mean square statistical error on the reconstructed states, for input states: $|D\rangle$ **(Top)** and maximally mixed **(Bottom)**. The lines represent the theoretical expectations for $\delta\varrho^W$ (points), $\delta\varrho^I$ (dashes and points), $\delta\varrho^{II}$ (dashes).

It is worth noticing that our protocol, the weak measurement proposal (Thekkadath et al., 2016), or the QST (James et al., 2001) allow to extract information on the system from which a raw density matrix is obtained. As also underlined by Thekkadath et al., 2016, if (semi)positivity is required, a post-processing on the data (such as MLE or equivalent techniques) is necessary for any method. On the other hand, if a single matrix element is required (in this case the positivity is not an issue), eq. (5.36) and (5.34) give it directly in terms of the measured observables. We note that in the QST framework, the single matrix element ϱ_{jk} can be obtained by measuring the four projectors $\hat{\Pi}_{a_j}$, $\hat{\Pi}_{a_k}$, $\hat{\Pi}_{|+\rangle}$ and $\hat{\Pi}_{|i\rangle}$ with $|+\rangle = 2^{-1/2}(|a_j\rangle + |a_k\rangle)$ and $|i\rangle = 2^{-1/2}(|a_j\rangle + i\,|a_k\rangle)$. Differently from the direct method, a QST-like approach requires projectors on states that are outside of the basis used to express the density matrix and that are different for each matrix element. If all elements are required, d^2 independent projectors are indeed needed: for large dimension systems this may become a very hard experimental challenge.

For this reason, we advocate that our scheme might be preferable to QST when the dimension d of the system is large (in both cases of few elements or full matrix reconstruction). This is because in our method (and the weak counterpart), to determine all the matrix element it is sufficient to realize $d+1$ different couplings (and not d^2 independent projectors as in QST-like methods) between the system and the measuring device and to measure a limited number of different pointer observables (just three, $\hat{\sigma}_{xA}\hat{\sigma}_{yB}$, $\hat{\sigma}_{yA}\hat{\sigma}_{yB}$, $\hat{\Pi}_{1A}\hat{\Pi}_{1B}$, in the case of 5.34). The different couplings are represented by the unitary operators $\hat{U}_{A,j}$ and $\hat{U}_B$ in Eq. 5.22. While the total number of measurements

is $O(d^2)$ as in QST, the numbers of building blocks required to realize them is drastically lower than QST.

Our experimental realization proves the validity of our proposal and shows that strong measurements are a feasible and convenient way to reconstruct the density operator even in single photon regime.

6

CONCLUSIONS

The main results of this thesis are here summarized.

In Chapter 2, we investigated the possibility of the quantum communication between a GNSS satellite and a ground station. By means of the SLR technique, we simulated an attenuated source on the satellite at the single photon level, with mean photon number $\mu_{\text{sat}} \simeq 10$. We have shown a detection frequency on ground of about 60 Hz, with a pulse frequency of 100 MHz over a total channel losses of 74 dB. Compared to the background the signal is such that the resulting SNR is about 0.5. Based on these results, we estimated the performances of a transmitter and receiver needed for the practical realization of a QC protocol from GNSS satellite. Using a state–of–art transmitter with 10 μrad of angular aperture, the geometric losses can be considerably reduced with respect to our simulated source (about 20 dB). Together with some optimization on the receiver side, we have shown that a SNR of 100 and a detection rate of 10 kHz is achievable.

Chapter 3 is dedicated to our realization of the Wheeler's delayed-choice experiment over a satellite–to–ground link. We encoded on the time bin degree of freedom the wave or particle properties to be tested and on the polarization of the photons the ancilla state the setup configuration. This scheme could be used for high-dimensional free-space quantum key distribution over long distances, since it exploits both polarization and time bin. By observing single-photon interference after the propagation along a 3500-km space channel, we can confute with clear statistical evidence of 5 sigma the description of light quanta as classical particles. In the alternative configuration of the detection scheme, the phase-dependent modulation in the received clicks disappears, and the which-path information can be clearly reconstructed. Our results extend the validity of the quantum mechanical description of complementarity to the spatial scale of LEO orbits. This work paves the way for satellite implementation of other foundational-like tests and applications of quantum mechanics involving hyper-entangled states.

In Chapter 4, I report on the implementation of a Bell inequality violation in a unprecedented scenario with three observers sharing a two-qubit entangled state. We designed and realized a weak measurement such that the amount of entanglement between Alice and Bob1, and Alice and Bob2, were enough to have a simultaneous violation of the two Bell inequalities. Indeed, in two set

of measurements each with 8 trials, the resulting mean CHSH parameter were $I^{(1)}_{\mathrm{CHSH}} = 2.125 \pm 0.003$ and $I^{(2)}_{\mathrm{CHSH}} = 2.096 \pm 0.003$ and $I^{(1)}_{\mathrm{CHSH}} = 2.114 \pm 0.003$ and $I^{(2)}_{\mathrm{CHSH}} = 2.064 \pm 0.003$. The achievement of double violation and the realization of a simple weak measurement scheme have important applications for QRNG, or for QKD.

Chapter 5 describes our proposed scheme for the direct reconstruction of the density matrix that extends the existing idea based on weak measurement. We have shown that our approach is exact for any value of the coupling strength between the system to be reconstructed and the pointers. In particular, the use of strong measurements makes our protocol less vulnerable to experimental statistical and systematic errors in comparison to the original proposal, while the lack of approximations in our expressions makes the results devoid of any inherent biases. In particular, our method uses the same resources and experimental operations of the weak counterpart, but achieves much better performance.

A

SOURCE OF POLARIZATION–BASED ENTANGLED PHOTONS

This appendix describes the working principles and performances of the polarization–based entangled photons source in our laboratory, which has been used to perform the experiments described in chapters 4 and 5. The source has been developed by Schiavon, 2016 as part of his PhD project.

A.1 SPONTANEOUS PARAMETRIC DOWN CONVERSION PROCESS

The generation of the photon-pairs is based on the SPDC. This process originates from the interaction between light and the non-linear optical properties of certain materials. The mathematical model is given by the following Maxwell's equations for the Electromagnetic field inside a medium:

$$\begin{aligned} \vec{\nabla} \cdot \vec{D}(\vec{r},t) &= \rho(\vec{r},t) \\ \vec{\nabla} \cdot \vec{B}(\vec{r},t) &= 0 \\ \vec{\nabla} \times \vec{E}(\vec{r},t) + \frac{\partial \vec{B}(\vec{r},t)}{\partial t} &= 0 \\ \vec{\nabla} \times \vec{H}(\vec{r},t) - \frac{\partial \vec{D}(\vec{r},t)}{\partial t} &= \vec{J}(\vec{r},t) \end{aligned} \tag{A.1}$$

where $\vec{D} = \varepsilon_0 \vec{E} + \vec{P}$ and $\vec{H} = \frac{1}{\mu_0}\vec{B} - \vec{M}$ are respectively the displacement and magnetizing fields, and $\vec{E}$ and $\vec{B}$ label the classical components of an EM field. Since most optical components are uncharged, non-conducting and non-magnetic, the density of free charges ρ, that of free currents $\vec{J}$ and the magnetization vector $\vec{M}$ are all null, so that the interaction is entirely captured by the polarization vector $\vec{P}$.

In the general case, the polarization vector can be expressed as a power series:

$$P_i = \varepsilon_0 \left(\sum_j \chi^{(1)}_{ij} E_j + \sum_{jk} \chi^{(2)}_{ijk} E_j E_k + \sum_{jkl} \chi^{(3)}_{ijkl} E_j E_k E_l + \dots \right) \tag{A.2}$$

where χ is the non-linear electric susceptibility of the medium. The term in the first order of E gives rise to the refraction phenomenon, whereas the other

with higher order give rise to non–linear effects. Using the Poynting theorem, it is possible to write the field energy density (i.e., the Hamiltonian density) in the medium as:

$$\begin{aligned}\mathcal{H} &= \frac{1}{2}\left(\vec{E}\cdot\vec{D}+\vec{B}\cdot\vec{H}\right)\\ &= \frac{1}{2}\varepsilon_0|\vec{E}|^2+\frac{1}{2\mu_0}|\vec{B}|^2+\frac{\varepsilon_0}{2}\sum_{ij}\chi^{(1)}_{ij}E_iE_j+\frac{\varepsilon_0}{2}\sum_{ijk}\chi^{(2)}_{ijk}E_iE_jE_k+\dots\\ &= \mathcal{H}_0+\mathcal{H}_I\end{aligned} \tag{A.3}$$

in which $\mathcal{H}_I$ describes the interaction between fields and matter.

Without delving too much into the details of quantum field theory, suffice it to say that fields can be transformed into operators as prescribed by second quantization so that the interaction Hamiltonian density becomes

$$\begin{aligned}\hat{\mathcal{H}}_I \propto &\sum_{ij}\chi^{(1)}_{ij}\left(\hat{E}^{(+)}_i+\hat{E}^{(-)}_i\right)\left(\hat{E}^{(+)}_j+\hat{E}^{(i)}_j\right)\\ &+\sum_{ijk}\chi^{(2)}_{ijk}\left(\hat{E}^{(+)}_i+\hat{E}^{(-)}_i\right)\left(\hat{E}^{(+)}_j+\hat{E}^{(i)}_j\right)\left(\hat{E}^{(+)}_k+\hat{E}^{(i)}_k\right)+\dots\end{aligned} \tag{A.4}$$

where $\hat{E}^{(+)}$ and $\hat{E}^{(-)}$ can respectively annihilate and create a field. The term of the Hamiltonian representing the pair generation is the following:

$$\hat{H}_{SPDC}=\int d^3r\sum_{i_pj_sk_i}\chi^{(2)}_{i_pj_sk_i}\hat{E}^{(+)}_{i_p}\hat{E}^{(-)}_{j_s}\hat{E}^{(-)}_{k_i} \tag{A.5}$$

in which symbol p stands for the annihilated *pump* photon, whereas i and s label the created *idler* and *signal* photons.

In order for the flow of energy to steadily move from the pump to the produced photons during the propagation in the medium, the so-called *phase matching* conditions have to be valid:

$$\begin{aligned}\omega_p &= \omega_s+\omega_i\\ \vec{k}_p &= \vec{k}_s+\vec{k}_i\end{aligned} \tag{A.6}$$

If the second is not verified, which can happen because of dispersion, the SPDC process is canceled out by its opposite an the net efficiency stays low. There are various ways to achieve phase matching, some of which are connected to the polarization of the involved light:

- *Type I birefringent phase matching*. A birefringent crystal is used, the pump sees the extraordinary refractive index while idler and signal see the ordinary one (or viceversa). This means that the produced photons share the same polarization which is orthogonal to that of the pump. One way of verifying phase matching is:

  $$\omega_s=\omega_i \quad\text{and}\quad n_o(\omega_s)+n_o(\omega_i)=2n_o(\omega_s)=2n_e(\omega_p) \tag{A.7}$$

  Photons are emitted symmetrically in a cone the axis of which coincides with the propagation direction of the pump.

- *Type II birefringent phase matching*. A birefringent crystal is used, pump and signal share the same polarization, orthogonal to that of the idler. One way of verifying phase matching is:

$$\omega_s = \omega_i \quad \text{and} \quad n_e(\omega_s) + n_o(\omega_i) = 2n_e(\omega_p) \tag{A.8}$$

  Photons are emitted in two different cones.

- *Quasi phase matching*. The crystal is engineered so that the sign of $\chi^{(2)}$ changes periodically and the production contributions always sum constructively. This can be achieved also without birefringence and with only one polarization involved (a configuration known as *type o phase matching*).

In all cases the polarization states are correlated with one another.

A.2 SAGNAC BASED SOURCE

The nonlinear material in our source is a $KTiOPO_4$ crystal (RAICOL Crystals PPKTP). The crystal is designed to achieve quasi phase matching when the pump is horizontally polarized, but the produced polarization states have the properties of type II SPDC (idler and signal are orthogonally polarized).

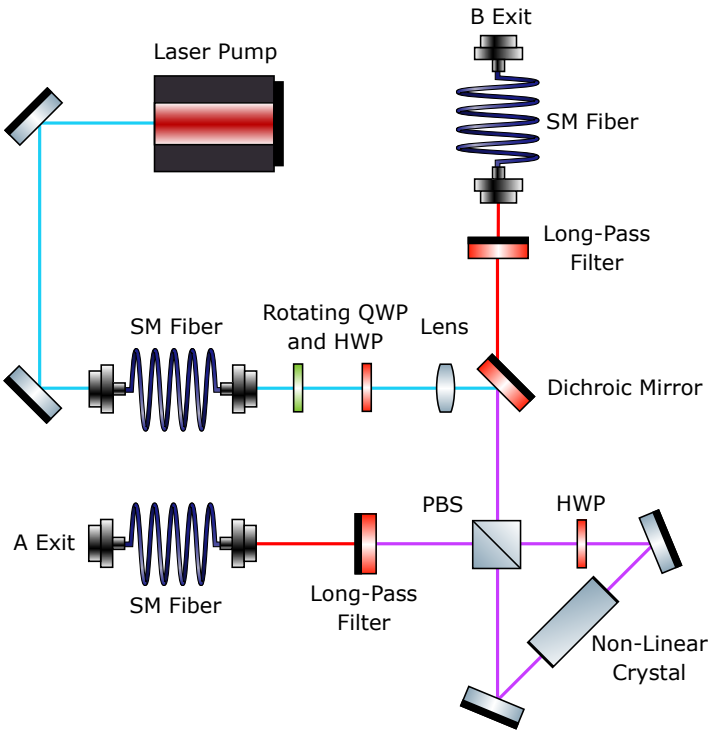

Figure A.1: Scheme of the entangled photon source.

The scheme of the setup is illustrated in Fig. A.1. The crystal is placed in the middle of a Sagnac interferometer, which comprises two mirrors and a PBS as input-output port. In this configuration the two arms share the same physical path, making the phase difference stable in time. The clockwise path comes from the reflection of the input pump into the PBS, therefore is vertically polarized. A HWP, working at double wavelength (405 nm and 810 nm), changes its polarization into the horizontal. Both arms of the interferometer trigger the SPDC process, producing an idler and signal photons either in the clockwise or counterclockwise path. Those of the latter path encounter the HWP that exchange their polarization. At the PBS, the two idler photons proceed towards the A exit and the two signals towards B, where they are collected into two single mode fibers and sent to the rest of the experiment. The superposition request is fulfilled by the fact that it is impossible to ascertain from which arm each of the signal (or idler) photons have come from. The pump light exiting the interferometer from the entrance port is deflected by dichroic mirrors and filtered out.

This source can generate any maximally entangled states such as the singlet

$$|\Psi^-\rangle = \frac{|H_A V_B\rangle - |V_A H_B\rangle}{\sqrt{2}} \tag{A.9}$$

At the output port of the PBS, the state is described by

$$|\psi_{pre}\rangle = \alpha|H_A V_B\rangle - e^{i\phi}\beta|V_A H_B\rangle \tag{A.10}$$

where α and β are the amplitude probabilities of the pump state $\alpha\,|H_p\rangle + \beta\,|V_p\rangle$, and ϕ is the phase difference of the interferometer arms. To adjust the pump polarization, we placed a QWP and a HWP. Maximally entangled state can be obtain rotating them such that $\alpha = \beta = \frac{1}{\sqrt{2}}$. The phase difference ϕ is compensated by introducing a birefringent material so that the photon exiting from A (or equivalently B) acquires a phase ϕ between the horizontal and vertical polarization. Finally, the compensation of the fiber transformation is realized using at least a polarization controller as discussed in Sec. 4.4.2.

A.3 PERFORMANCE AND POLARIZATION STABILITY

The number of produced pairs depends on many different factors, the most important of which is of course the power of the pump laser. Due to the small $\chi^{(2)}$ coefficient, only a tiny fraction of the photons that hit the crystal is converted. Of the results, many are lost in the fiber coupling and some are not detected because of the imperfect SPAD efficiency (nominally $\eta_{SPAD} \sim 45\%$).

We analyzed the production for different power values by counting photons just after the two exit fibers of the source (see Tab. A.1). The ratio between coincident and total counts is $\eta_{coinc} \approx 7\%$, which suggests that the

Driving Current (mA)	Pump power on the crystal (μW)	Photon counts (kHz)	Coincident Photon counts (kHz)
20	10.76 ± 0.01	2.8 ± 0.1	0.19 ± 0.01
25	343 ± 1	116 ± 1	10.3 ± 0.1
30	2302 ± 2	598 ± 1	44.3 ± 0.2
35	3331 ± 1	961 ± 5	67.2 ± 0.4
40	6840 ± 1	1580 ± 7	106.2 ± 0.3
45	9210 ± 2	2065 ± 2	138.2 ± 0.5
50	11050 ± 4	2509 ± 3	166.0 ± 0.5
55	12660 ± 4	2962 ± 4	196.6 ± 0.5

Table A.1: Detected photons with different power settings. The pump power on the crystal does not coincide with the optical power emitted by the diode laser, much of which is lost at the first fiber coupling and some is reflected by the optical components before the interferometer. The third column lists the average tally of the two SPADs.

efficiency of the fiber coupling is around $\eta_{coupling} = \frac{\eta_{coinc}}{\eta_{SPAD}} \approx 16\%$. Such a small value is mostly due to the fact that the signal and idler beams are not collimated because of the lens that focuses the pump light at the center of the crystal. This compromise was made as it greatly improves the production efficiency of the material itself.

BIBLIOGRAPHY

Agnesi, Costantino et al. (2018). "Exploring the boundaries of quantum mechanics: Advances in satellite quantum communications." In: *Philosophical Transactions of the Royal Society A: Mathematical, Physical and Engineering Sciences* 376.2123, p. 20170461. ISSN: 1364503X. DOI: 10.1098/rsta.2017.0461.

Aharonov, Yakir, David Z. Albert, and Lev Vaidman (1988). "How the result of a measurement of a component of the spin of a spin- 1/2 particle can turn out to be 100." In: *Physical Review Letters* 60.14, pp. 1351–1354. ISSN: 0031-9007. DOI: 10.1103/PhysRevLett.60.1351.

Alley, C.O., O. Jakubowicz, C.A. Steggerda, and W.C. Wickes (1983). "A delayed random choice quantum mechanics experiment with light quanta." In: *International symposium foundations of quantum mechanics in the light of new technology*. Tokyo: Physical Society of Japan.

Arnold, DA (1979). "Method of calculating retroreflector-array transfer functions." In: *SAO Special Report* 382.

Baldwin, Charles H., Ivan H. Deutsch, and Amir Kalev (2016). "Strictly-complete measurements for bounded-rank quantum-state tomography." In: *Physical Review A* 93.5, p. 052105. ISSN: 2469-9926. DOI: 10.1103/PhysRevA.93.052105.

Baldzuhn, J., E. Mohler, and W. Martienssen (1989). "A wave-particle delayed-choice experiment with a single-photon state." In: *Zeitschrift f{\"u}r Physik B Condensed Matter* 77.2, pp. 347–352. DOI: 10.1007/BF01313681.

Barbieri, Marco, Francesco De Martini, Paolo Mataloni, Giuseppe Vallone, and Adán Cabello (2006). "Enhancing the Violation of the Einstein-Podolsky-Rosen Local Realism by Quantum Hyperentanglement." In: *Physical Review Letters* 97.14, p. 140407. ISSN: 0031-9007. DOI: 10.1103/PhysRevLett.97.140407.

Bell, John Stewart (1964). "On the Einstein Podolsky Rosen paradox." In: *Physics* 1, pp. 195–200.

Bianco, G., R. Devoti, V. Luceri, and C. Sciarretta (2001a). "A review of SLR contributions to geophysics in Eurasia by CGS." In: *Surveys in Geophysics* 22.5-6, pp. 481–490. ISSN: 01693298. DOI: 10.1023/A:1015620201801.

Bianco, G., M. Chersich, R. Devoti, V. Luceri, and M. Selden (2001b). "Measurement of LAGEOS-2 rotation by satellite laser ranging observations." In: *Geophysical Research Letters* 28.10, pp. 2113–2116. ISSN: 00948276. DOI: 10.1029/2000GL012435.

Bohm, D. and Y. Aharonov (1957). "Discussion of Experimental Proof for the Paradox of Einstein, Rosen, and Podolsky." In: *Physical Review* 108.4,

pp. 1070–1076. ISSN: 0031-899X. DOI: 10.1103/PhysRev.108.1070. URL: https://link.aps.org/doi/10.1103/PhysRev.108.1070.

Bohr, Niels (1928). "The Quantum Postulate and the Recent Development of Atomic Theory." In: *Nature* 121.3050, pp. 580–590. ISSN: 0028-0836. DOI: 10.1038/121580a0. arXiv: arXiv:1001.0131.

Brodutch, Aharon, Alexei Gilchrist, Thomas Guff, Alexander R.H. Smith, and Daniel R. Terno (2015). "Post-Newtonian gravitational effects in optical interferometry." In: *Physical Review D - Particles, Fields, Gravitation and Cosmology* 91.6, p. 064041. ISSN: 15502368. DOI: 10.1103/PhysRevD.91.064041.

Brunner, Nicolas, Daniel Cavalcanti, Stefano Pironio, Valerio Scarani, and Stephanie Wehner (2014). "Bell nonlocality." In: *Reviews of Modern Physics* 86.2, pp. 419–478. ISSN: 15390756. DOI: 10.1103/RevModPhys.86.419.

Bruschi, David Edward, Timothy C. Ralph, Ivette Fuentes, Thomas Jennewein, and Mohsen Razavi (2014). "Spacetime effects on satellite-based quantum communications." In: *Physical Review D - Particles, Fields, Gravitation and Cosmology* 90.4, p. 045041. ISSN: 15502368. DOI: 10.1103/PhysRevD.90.045041. arXiv: 1309.3088.

Cabello, Adán (2006). "Bipartite Bell Inequalities for Hyperentangled States." In: *Physical Review Letters* 97.14, p. 140406. ISSN: 0031-9007. DOI: 10.1103/PhysRevLett.97.140406.

Cao, Yuan et al. (2018). "Bell Test over Extremely High-Loss Channels: Towards Distributing Entangled Photon Pairs between Earth and the Moon." In: *Physical Review Letters* 120.14, p. 140405. ISSN: 10797114. DOI: 10.1103/PhysRevLett.120.140405.

Clauser, John F., Michael A. Horne, Abner Shimony, and Richard A. Holt (1969). "Proposed Experiment to Test Local Hidden-Variable Theories." In: *Physical Review Letters* 23.15, pp. 880–884. ISSN: 0031-9007. DOI: 10.1103/PhysRevLett.23.880.

Coffman, Valerie, Joydip Kundu, and William K. Wootters (2000). "Distributed entanglement." In: *Physical Review A* 61.5, p. 052306. ISSN: 1050-2947. DOI: 10.1103/PhysRevA.61.052306.

Curchod, F. J., M. Johansson, R. Augusiak, M. J. Hoban, P. Wittek, and A. Acín (2017). "Unbounded randomness certification using sequences of measurements." In: *Physical Review A* 95.2, p. 020102. ISSN: 2469-9926. DOI: 10.1103/PhysRevA.95.020102.

Davisson, C. J. (1928). "The Diffraction of Electrons by a Crystal of Nickel." In: *Bell System Technical Journal* 7.1, pp. 90–105. ISSN: 15387305. DOI: 10.1002/j.1538-7305.1928.tb00342.x.

Degnan, John J. (1993). "Contributions of Space Geodesy to Geodynamics: Technology." In: *Contributions of Space Geodesy to Geodynamics: Technology* 25.January 1993, pp. 133–162. ISSN: 0277-6669. DOI: 10.1029/GD025.

Denkmayr, Tobias, Hermann Geppert, Hartmut Lemmel, Mordecai Waegell, Justin Dressel, Yuji Hasegawa, and Stephan Sponar (2017). "Experimental

Demonstration of Direct Path State Characterization by Strongly Measuring Weak Values in a Matter-Wave Interferometer." In: *Physical Review Letters* 118.1, p. 010402. ISSN: 0031-9007. DOI: 10.1103/PhysRevLett.118.010402.

Dequal, Daniele, Giuseppe Vallone, Davide Bacco, Simone Gaiarin, Vincenza Luceri, Giuseppe Bianco, and Paolo Villoresi (2016). "Experimental single-photon exchange along a space link of 7000 km." In: *Physical Review A* 93.1, p. 010301. ISSN: 24699934. DOI: 10.1103/PhysRevA.93.010301.

Di Lorenzo, Antonio (2013a). "Quantum state tomography from a sequential measurement of two variables in a single setup." In: *Physical Review A* 88.4, p. 042114. ISSN: 1050-2947. DOI: 10.1103/PhysRevA.88.042114.

Di Lorenzo, Antonio (2013b). "Sequential Measurement of Conjugate Variables as an Alternative Quantum State Tomography." In: *Physical Review Letters* 110.1, p. 010404. ISSN: 0031-9007. DOI: 10.1103/PhysRevLett.110.010404.

Duck, I. M., P. M. Stevenson, and E. C. G. Sudarshan (1989). "The sense in which a "weak measurement" of a spin-½ particle's spin component yields a value 100." In: *Physical Review D* 40.6, pp. 2112–2117. ISSN: 0556-2821. DOI: 10.1103/PhysRevD.40.2112.

Einstein, A. (1905). "Zur Elektrodynamik bewegter Körper." In: *Annalen der Physik* 322.10, pp. 891–921. ISSN: 00033804. DOI: 10.1002/andp.19053221004.

Einstein, A., B. Podolsky, and N. Rosen (1935). "Can Quantum-Mechanical Description of Physical Reality Be Considered Complete?" In: *Physical Review* 47.10, pp. 777–780. ISSN: 0031-899X. DOI: 10.1103/PhysRev.47.777.

Feynman, Richard P (1982). *Simulating Physics with Computers*. Tech. rep. 6.

Fink, Matthias, Ana Rodriguez-Aramendia, Johannes Handsteiner, Abdul Ziarkash, Fabian Steinlechner, Thomas Scheidl, Ivette Fuentes, Jacques Pienaar, Timothy C. Ralph, and Rupert Ursin (2017). "Experimental test of photonic entanglement in accelerated reference frames." In: *Nature Communications* 8, p. 15304. ISSN: 20411723. DOI: 10.1038/ncomms15304. arXiv: 1608.02473.

Foletto, Giulio (2017). "Direct Reconstruction of the Quantum Density Operator via Measurements of Arbitrary Strength." MA thesis. Università Degli Studi di Padova.

Freedman, Stuart J. and John F. Clauser (1972). "Experimental Test of Local Hidden-Variable Theories." In: *Physical Review Letters* 28.14, pp. 938–941. ISSN: 0031-9007. DOI: 10.1103/PhysRevLett.28.938.

Friberg, S., C. K. Hong, and L. Mandel (1985). "Measurement of Time Delays in the Parametric Production of Photon Pairs." In: *Physical Review Letters* 54.18, pp. 2011–2013. ISSN: 0031-9007. DOI: 10.1103/PhysRevLett.54.2011.

Giustina, Marissa et al. (2015). "Significant-Loophole-Free Test of Bell's Theorem with Entangled Photons." In: *Physical Review Letters* 115.25, p. 250401. ISSN: 0031-9007. DOI: 10.1103/PhysRevLett.115.250401.

Glonass K1 corner cube retroreflector array. URL: https://ilrs.cddis.eosdis.nasa.gov/docs/glonass125{_}array.pdf.

Goyeneche, D., G. Cañas, S. Etcheverry, E. S. Gómez, G. B. Xavier, G. Lima, and A. Delgado (2015). "Five Measurement Bases Determine Pure Quantum States on Any Dimension." In: *Physical Review Letters* 115.9, p. 090401. ISSN: 0031-9007. DOI: 10.1103/PhysRevLett.115.090401.

Graham, Trent, Christopher Zeitler, Joseph Chapman, Paul Kwiat, Hamid Javadi, and Herbert Bernstein (2015). "Superdense teleportation and quantum key distribution for space applications." In: *2015 IEEE International Conference on Space Optical Systems and Applications (ICSOS)*. IEEE, pp. 1–7. ISBN: 978-1-5090-0281-8. DOI: 10.1109/ICSOS.2015.7425090.

Greenberger, D.M., M.A. Horne, C.G. Shull, and A. Zeilinger (1983). "Delayed-choise experiments with the neutron interferometer." In: *International Symposium on Foundations of Quantum Mechanics in the Light of New Technology*. Tokyo: Physical Society of Japan.

Gross, Jonathan A., Ninnat Dangniam, Christopher Ferrie, and Carlton M. Caves (2015). "Novelty, efficacy, and significance of weak measurements for quantum tomography." In: *Physical Review A* 92.6, p. 062133. ISSN: 1050-2947. DOI: 10.1103/PhysRevA.92.062133.

Hellmuth, T., H. Walther, A. Zajonc, and W. Schleich (1987). "Delayed-choice experiments in quantum interference." In: *Physical Review A* 35.6, pp. 2532–2541. ISSN: 0556-2791. DOI: 10.1103/PhysRevA.35.2532.

Hensen, B. et al. (2015). "Loophole-free Bell inequality violation using electron spins separated by 1.3 kilometres." In: *Nature* 526.7575, pp. 682–686. ISSN: 0028-0836. DOI: 10.1038/nature15759.

Hooke, Robert (1665). *Micrographia: or, Some physiological descriptions of minute bodies made by magnifying glasses*. The Royal Society.

Huygens, Christiaan. (1690). *Traité de la Lumière*. Leiden: Pieter van der Aa, p. 347. ISBN: 9781615303748.

Hwang, Won Young (2003). "Quantum Key Distribution with High Loss: Toward Global Secure Communication." In: *Physical Review Letters* 91.5, p. 057901. ISSN: 10797114. DOI: 10.1103/PhysRevLett.91.057901.

Idani, Hitoshi et al. (2013). ""Hook and roll technique" using an articulating hook cautery to provide a critical view during single-incision laparoscopic cholecystectomy." In: *Acta Medica Okayama* 67.4, pp. 259–263. ISSN: 0386300X. DOI: 10.1063/1.3610677.

Ilrs. *ILRS Home Page*. URL: https://ilrs.cddis.eosdis.nasa.gov/ (visited on 08/26/2018).

Jacques, Vincent, E Wu, Frédéric Grosshans, François Treussart, Philippe Grangier, Alain Aspect, and Jean-François Roch (2007). "Experimental realization of Wheeler's delayed-choice gedanken experiment." In: *Science (New York, N.Y.)* 315.5814, pp. 966–8. ISSN: 1095-9203. DOI: 10.1126/science.1136303.

Jacques, Vincent, E Wu, Frédéric Grosshans, François Treussart, Philippe Grangier, Alain Aspect, and Jean-François Roch (2008). "Delayed-Choice Test of Quantum Complementarity with Interfering Single Photons." In: *Physical Review Letters* 100.22, p. 220402. ISSN: 0031-9007. DOI: 10.1103/PhysRevLett.100.220402.

James, Daniel F. V., Paul G. Kwiat, William J. Munro, and Andrew G. White (2001). "Measurement of qubits." In: *Physical Review A* 64.5, p. 052312. ISSN: 1050-2947. DOI: 10.1103/PhysRevA.64.052312.

Jennewein, T., C. Grant, E. Choi, C. Pugh, C. Holloway, JP. Bourgoin, H. Hakima, B. Higgins, and R. Zee (2014). "The NanoQEY mission: ground to space quantum key and entanglement distribution using a nanosatellite." In: ed. by Mark T. Gruneisen, Miloslav Dusek, John G. Rarity, Keith L. Lewis, Richard C. Hollins, Thomas J. Merlet, and Alexander Toet. Vol. 9254. International Society for Optics and Photonics, p. 925402. ISBN: 9781628413175. DOI: 10.1117/12.2067548.

Joshi, Siddarth Koduru et al. (2018). "Space QUEST mission proposal: Experimentally testing decoherence due to gravity." In: *New Journal of Physics* 20.6, p. 063016. ISSN: 13672630. DOI: 10.1088/1367-2630/aac58b.

Kaiser, Florian, Thomas Coudreau, Pérola Milman, Daniel B Ostrowsky, and Sébastien Tanzilli (2012). "Entanglement-enabled delayed-choice experiment." In: *Science (New York, N.Y.)* 338.6107, pp. 637–40. ISSN: 1095-9203. DOI: 10.1126/science.1226755.

Kim, Taehyun, Marco Fiorentino, and Franco N C Wong (2006). "Phase-stable source of polarization-entangled photons using a polarization Sagnac interferometer." In: *Physical Review A* 73.1, p. 12316. ISSN: 1050-2947. DOI: 10.1103/PhysRevA.73.012316.

Kirchner, G., Grunwaldt, L., Neubert, R., Koidl, F., Barschke, M., Yoon, Z., Fiedler, H., Hollenstein, C. (2013). "Laser Ranging to Nano Satellites in LEO Orbits: Plans, Issues, Simulations." In: *18th International Workshop on Laser Ranging*. Fujiyoshida, Japan.

Kurtsiefer, Christian, Sonja Mayer, Patrick Zarda, and Harald Weinfurter (2000). "Stable Solid-State Source of Single Photons." In: *Physical Review Letters* 85.2, pp. 290–293. ISSN: 0031-9007. DOI: 10.1103/PhysRevLett.85.290.

Larsson, Jan-Åke (2014). "Loopholes in Bell inequality tests of local realism." In: *Journal of Physics A: Mathematical and Theoretical* 47.42, p. 424003. ISSN: 1751-8113. DOI: 10.1088/1751-8113/47/42/424003.

Liao, Sheng-Kai et al. (2017). "Satellite-to-ground quantum key distribution." In: *Nature* 549.7670, pp. 43–47. ISSN: 0028-0836. DOI: 10.1038/nature23655.

Lloyd, S. (1994). "Envisioning a Quantum Supercomputer." In: *Science* 263.5147, pp. 695–695. ISSN: 0036-8075. DOI: 10.1126/science.263.5147.695.

Lundeen, J.S. and K.J. Resch (2005). "Practical measurement of joint weak values and their connection to the annihilation operator." In: *Physics Letters*

A 334.5-6, pp. 337–344. ISSN: 0375-9601. DOI: 10.1016/J.PHYSLETA.2004.11.037.

Lundeen, Jeff S. and Charles Bamber (2012). "Procedure for Direct Measurement of General Quantum States Using Weak Measurement." In: *Physical Review Letters* 108.7, p. 070402. ISSN: 0031-9007. DOI: 10.1103/PhysRevLett.108.070402.

Lundeen, Jeff S., Brandon Sutherland, Aabid Patel, Corey Stewart, and Charles Bamber (2011). "Direct measurement of the quantum wavefunction." In: *Nature* 474.7350, pp. 188–191. ISSN: 0028-0836. DOI: 10.1038/nature10120.

Ma, Xiao Song, Johannes Kofler, and Anton Zeilinger (2016). "Delayed-choice gedanken experiments and their realizations." In: *Reviews of Modern Physics* 88.1, pp. 1–25. ISSN: 15390756. DOI: 10.1103/RevModPhys.88.015005.

Ma, Xiao-song, Stefan Zotter, Johannes Kofler, Rupert Ursin, Thomas Jennewein, Časlav Brukner, and Anton Zeilinger (2012). "Experimental delayed-choice entanglement swapping." In: *Nature Physics* 8.6, pp. 479–484. ISSN: 1745-2473. DOI: 10.1038/nphys2294.

Maccone, Lorenzo and Cosimo C. Rusconi (2014). "State estimation: A comparison between direct state measurement and tomography." In: *Physical Review A* 89.2, p. 022122. ISSN: 1050-2947. DOI: 10.1103/PhysRevA.89.022122.

Mal, Shiladitya, A. S. Majumdar, and Dipankar Home (2016). "Sharing of Nonlocality of a single member of an Entangled Pair Is Not Possible by More Than Two Unbiased Observers on the other wing." In: arXiv: 1604.08718.

Masanes, Ll., A. Acin, and N. Gisin (2006). "General properties of nonsignaling theories." In: *Physical Review A* 73.1, p. 012112. ISSN: 1050-2947. DOI: 10.1103/PhysRevA.73.012112.

Miller, W.A. (1983). "A proposed delayed-choice experiment using ultra-cold neutrons." In: *International symposium foundations of quantum mechanics in the light of new technology*. Tokyo: Physical Society of Japan.

Miller, W.A. and J.A. Wheeler (1983). "Delayed-choice experiments and Bohr's elementary quantum phenomenon." In: *International symposium foundations of quantum mechanics in the light of new technology*. Tokyo: Physical Society of Japan.

Montenbruck, O., R. Schmid, F. Mercier, P. Steigenberger, C. Noll, R. Fatkulin, S. Kogure, and A. S. Ganeshan (2015). "GNSS satellite geometry and attitude models." In: *Advances in Space Research* 56.6, pp. 1015–1029. ISSN: 18791948. DOI: 10.1016/j.asr.2015.06.019.

Murphy, Thomas W. and Scott D. Goodrow (2013). "Polarization and far-field diffraction patterns of total internal reflection corner cubes." In: *Applied Optics* 52.2, p. 117. ISSN: 0003-6935. DOI: 10.1364/AO.52.000117.

Neumann, John von (1932). *Mathematical Foundations of Quantum Mechanics*.

Newton, Isaac (1730). *Opticks: Or, A Treatise of the Reflections, Refractions, Inflections and Colours of Light*. London: William Innys at the West-End of St. Paul's, p. 382.

Nielsen, Michael A. and Isaac L. Chuang (2010). *Quantum Computation and Quantum Information*. Cambridge University Press, Cambridge. ISBN: 9780511976667. DOI: https://doi.org/10.1017/CBO9780511976667.

Otsubo, Toshimichi, GM Appleby, and Philip Gibbs (2001). "GLONASS laser ranging accuracy with satellite signature effect." In: *Surveys in geophysics* 22.5/6, pp. 509–516. ISSN: 1573-0956. DOI: 10.1023/A:1015676419548.

Pais, A. (1979). "Einstein and the quantum theory." In: *Reviews of Modern Physics* 51.4, pp. 863–914. ISSN: 00346861. DOI: 10.1103/RevModPhys.51.863.

Paul, H. (1982). "Photon antibunching." In: *Reviews of Modern Physics* 54.4, pp. 1061–1102. ISSN: 00346861. DOI: 10.1103/RevModPhys.54.1061.

Pearlman, M. R., J. J. Degnan, and J. M. Bosworth (2002). "The International Laser Ranging Service." In: *Advances in Space Research* 30.2, pp. 135–143. ISSN: 02731177. DOI: 10.1016/S0273-1177(02)00277-6.

Ren, Ji Gang et al. (2017). "Ground-to-satellite quantum teleportation." In: *Nature* 549.7670, pp. 70–73. ISSN: 14764687. DOI: 10.1038/nature23675.

Renes, Joseph M (2015). *Quantum Information Theory*. Lecture no.

Rideout, David et al. (2012). "Fundamental quantum optics experiments conceivable with satellites - Reaching relativistic distances and velocities." In: *Classical and Quantum Gravity* 29.22, p. 224011. ISSN: 02649381. DOI: 10.1088/0264-9381/29/22/224011.

Ritchie, N. W. M., J. G. Story, and Randall G. Hulet (1991). "Realization of a measurement of a "weak value"." In: *Physical Review Letters* 66.9, pp. 1107–1110. ISSN: 0031-9007. DOI: 10.1103/PhysRevLett.66.1107.

Rityn, N. E. (1967). "Optics of corner cube retroreflectors." In: *Soviet Journ.Opt. Tech.* 34, pp. 198 –201.

Salvail, Jeff Z., Megan Agnew, Allan S. Johnson, Eliot Bolduc, Jonathan Leach, and Robert W. Boyd (2013). "Full characterization of polarization states of light via direct measurement." In: *Nature Photonics* 7.4, pp. 316–321. ISSN: 1749-4885. DOI: 10.1038/nphoton.2013.24.

Scheidl, T., E. Wille, and R. Ursin (2013). "Quantum optics experiments using the International Space Station: A proposal." In: *New Journal of Physics* 15.4, p. 043008. ISSN: 13672630. DOI: 10.1088/1367-2630/15/4/043008.

Schiavon, Matteo (2016). "Space Quantum Communication." PhD thesis. Università Degli Studi di Padova.

Schmied, Roman (2016). "Quantum state tomography of a single qubit: comparison of methods." In: *Journal of Modern Optics* 63.18, pp. 1744–1758. ISSN: 0950-0340. DOI: 10.1080/09500340.2016.1142018.

Shalm, Lynden K. et al. (2015). "Strong Loophole-Free Test of Local Realism." In: *Physical Review Letters* 115.25, p. 250402. ISSN: 0031-9007. DOI: 10.1103/PhysRevLett.115.250402.

Silva, Ralph, Nicolas Gisin, Yelena Guryanova, and Sandu Popescu (2015). "Multiple Observers Can Share the Nonlocality of Half of an Entangled Pair by Using Optimal Weak Measurements." In: *Physical Review Letters* 114.25, p. 250401. ISSN: 0031-9007. DOI: 10.1103/PhysRevLett.114.250401.

Steinlechner, Fabian, Sebastian Ecker, Matthias Fink, Bo Liu, Jessica Bavaresco, Marcus Huber, Thomas Scheidl, and Rupert Ursin (2017). "Distribution of high-dimensional entanglement via an intra-city free-space link." In: *Nature Communications* 8, p. 15971. ISSN: 2041-1723. DOI: 10.1038/ncomms15971.

Stipčević, M. and B. Medved Rogina (2007). "Quantum random number generator based on photonic emission in semiconductors." In: *Review of Scientific Instruments* 78.4, p. 045104. ISSN: 00346748. DOI: 10.1063/1.2720728.

Strutt, John William and Baron Rayleigh (1878). *The Theory of Sound*. Vol. 2. New York: Dover Publ., p. 480.

Thekkadath, G. S., L. Giner, Y. Chalich, M. J. Horton, J. Banker, and J. S. Lundeen (2016). "Direct Measurement of the Density Matrix of a Quantum System." In: *Physical Review Letters* 117.12, p. 120401. ISSN: 0031-9007. DOI: 10.1103/PhysRevLett.117.120401.

Toner, B. (2009). "Monogamy of non-local quantum correlations." In: *Proceedings of the Royal Society A: Mathematical, Physical and Engineering Sciences* 465.2101, pp. 59–69. ISSN: 1364-5021. DOI: 10.1098/rspa.2008.0149.

Troupe, J E and J M Farinholt (2015). *A Contextuality Based Quantum Key Distribution Protocol*. Tech. rep. arXiv: 1512.02256v2.

Ursin, Rupert et al. (2008). "Space-QUEST: Experiments with quantum entanglement in space." In: *Europhysics News* 40.3, pp. 26–29. ISSN: 0531-7479. DOI: 10.1051/epn/2009503. arXiv: 0806.0945.

Vallone, Giuseppe and Daniele Dequal (2016). "Strong Measurements Give a Better Direct Measurement of the Quantum Wave Function." In: *Physical Review Letters* 116.4, p. 040502. ISSN: 0031-9007. DOI: 10.1103/PhysRevLett.116.040502.

Vallone, Giuseppe, Davide Bacco, Daniele Dequal, Simone Gaiarin, Vincenza Luceri, Giuseppe Bianco, and Paolo Villoresi (2015). "Experimental Satellite Quantum Communications." In: *Physical Review Letters* 115.4, p. 040502. ISSN: 0031-9007. DOI: 10.1103/PhysRevLett.115.040502.

Vallone, Giuseppe, Daniele Dequal, Marco Tomasin, Francesco Vedovato, Matteo Schiavon, Vincenza Luceri, Giuseppe Bianco, and Paolo Villoresi (2016). "Interference at the Single Photon Level Along Satellite-Ground Channels." In: *Physical Review Letters* 116.25, p. 253601. ISSN: 0031-9007. DOI: 10.1103/PhysRevLett.116.253601.

Vedovato, Francesco et al. (2017). "Extending Wheeler's delayed-choice experiment to space." In: *Science Advances* 3.10, e1701180. ISSN: 23752548. DOI: 10.1126/sciadv.1701180.

Villar, Aitor, Alexander Lohrmann, and Alexander Ling (2017). "Experimental entangled photon pair generation using crystals with parallel optical

axes." In: *Optics Express* 26.10, p. 12396. ISSN: 1094-4087. DOI: 10.1364/OE.26.012396.

Wang, Xiang Bin (2005). "Beating the photon-number-splitting attack in practical quantum cryptography." In: *Physical Review Letters* 94.23, p. 230503. ISSN: 00319007. DOI: 10.1103/PhysRevLett.94.230503.

Wheeler, John Archibald (1983). *Quantum theory and measurement.* Ed. by John Archibald Wheeler and Wojciech Hubert Zurek. Princeton Univ Press. ISBN: 9780691613161.

Yin, Juan et al. (2017). "Satellite-based entanglement distribution over 1200 kilometers." In: *Science* 356.6343, pp. 1140–1144. ISSN: 10959203. DOI: 10.1126/science.aan3211.

Zhang, Yu-Xiang, Shengjun Wu, and Zeng-Bing Chen (2016). "Coupling-deformed pointer observables and weak values." In: *Physical Review A* 93.3, p. 032128. ISSN: 2469-9926. DOI: 10.1103/PhysRevA.93.032128.

Zhong, Tian et al. (2015). "Photon-efficient quantum key distribution using time–energy entanglement with high-dimensional encoding." In: *New Journal of Physics* 17.2, p. 022002. ISSN: 1367-2630. DOI: 10.1088/1367-2630/17/2/022002.

Zhu, Xuanmin, Yu-Xiang Zhang, and Shengjun Wu (2016). "Direct state reconstruction with coupling-deformed pointer observables." In: *Physical Review A* 93.6, p. 062304. ISSN: 2469-9926. DOI: 10.1103/PhysRevA.93.062304.

Zou, Ping, Zhi-Ming Zhang, and Wei Song (2015). "Direct measurement of general quantum states using strong measurement." In: *Physical Review A* 91.5, p. 052109. ISSN: 1050-2947. DOI: 10.1103/PhysRevA.91.052109.

Żukowski, M., A. Zeilinger, M. A. Horne, and A. K. Ekert (1993). ""Event-ready-detectors" Bell experiment via entanglement swapping." In: *Physical Review Letters* 71.26, pp. 4287–4290. ISSN: 0031-9007. DOI: 10.1103/PhysRevLett.71.4287.

Zych, Magdalena, Fabio Costa, Igor Pikovski, Timothy C. Ralph, and Časlav Brukner (2012). "General relativistic effects in quantum interference of photons." In: *Classical and Quantum Gravity* 29.22, p. 224010. ISSN: 02649381. DOI: 10.1088/0264-9381/29/22/224010.